Tracing the source of oxidizing fluids in subduction zones using iron isotopes in garnet

Author: Anna R. Gerrits

Boston College Electronic Thesis or Dissertation, 2018

Tracing the source of oxidizing fluids in subduction zones using iron isotopes in garnet

Anna R. Gerrits

A thesis

submitted to the Faculty of

the department of Earth and Environmental Sciences

in partial fulfillment

of the requirements for the degree of

Master of Science

Boston College
Morrissey College of Arts and Sciences
Graduate School

September 2018

Tracing the source of oxidizing fluids in subduction zones using iron isotopes in garnet

Anna R. Gerrits

Advisor: Ethan Baxter, Ph.D.

Subduction zones are the primary areas of chemical and mass transfer between the Earth's surface and the mantle. Dehydration during subduction has been linked to subduction seismicity, arc volcanism, and redox (fO_2) changes in the subducting slab and overlying mantle wedge. Despite this, no petrologic record tracing the source of oxidizing fluids from the down going slab has yet been observed. To address this, this study shows a direct record of progressive redox change recorded in zoned garnet crystals from Sifnos and Syros, Greece that grew through the breakdown of the hydrous mineral lawsonite during subduction. Oxygen fugacities (fO_2) calculated using garnet-epidote oxybarometry for multiple growth zones within single garnet grains have been compared with stable iron isotope compositions in the same growth zone. These combined measurements reveal that garnet cores grew under oxidized conditions, recording higher fO_2 and lower δ^{56}Fe values, whereas garnet rims grew under more reduced conditions with lower fO_2 and higher δ^{56}Fe values. This is consistent with the release of oxidizing fluids into the sub-arc mantle accompanying lawsonite breakdown and dehydration, leaving behind a progressively reduced residual slab mineral assemblage. These coupled fO_2 and Fe isotope data show that slab dehydration accompanying lawsonite breakdown plays an important and measureable role in the global redox budget, and provides a mechanism for sub-arc mantle oxidation.

TABLE OF CONTENTS

LIST OF TABLES

LIST OF FIGURES

ACKNOWLEDGEMENTS

I would like to thank my lab group and fellow graduate students at Boston College for their continued support and encouragement throughout my entire degree. Thank you to all the collaborators who worked on this project, Edward Inglis, Besim Dragovic, Kevin Burton, Ethan Baxter, and Paul Starr, who all generously offered their time and knowledge, without which, this project wouldn’t have been possible. Paul Starr, thank you for your constant support and advise. Thank you to Mark Caddick for believing in me and this project. Thanks to Seth Kruckenberg for his comments and edits. And thanks to Zeb Page for starting and supporting my interest in the wonderful world of oxygen fugacity. Ethan Baxter, thank you for everything you have done to support me- this project literally would not have been possible without you. And finally, thanks to my family for supporting me in everything I choose to do.

"There are two types of people in the world: people that don't understand oxygen fugacity and people that have never heard of it."

-Unknown

INTRODUCTION

Subduction zones are the primary areas of chemical and mass transfer between the Earth's surface and the mantle. During subduction, the down-going plate carries oxidized material into the subduction complex and releases large amounts of water and volatiles, such as carbon, through the breakdown of hydrous minerals (Schmidt and Poli, 1998; Magni et al., 2014). This dehydration has been linked to subduction seismicity (Okazaki and Hirth, 2016), arc volcanism (Schmidt and Poli, 1998; Tatsumi, 1986; Marschall and Schumacher, 2012), and possible redox (fO_2) changes in the subducting slab and overlying mantle wedge (Debret and Sverjensky, 2017; Evens et al., 2012; Kelley and Cottrell, 2009; Groppo and Castelli, 2010; Parkinson and Arculus, 1999; Breeding et al., 2004). Oxygen fugacity (fO_2), the chemical potential of oxygen in a system, is an intensive thermodynamic property that controls the speciation of multi-valent elements, such as Fe, S, Ce, and V. This control regulates the ability of these elements to contribute to mineral forming reactions (Frost, 1991). Consequently, oxygen fugacity is an important chemical control in an environment, such as a subduction zone, where the subducting slab experiences multiple changes in mineral assemblages due to changing pressure-temperature (P-T) conditions.

The interaction between material coming off the subducting slab and its possible effects in the sub-arc mantle has been the focus of much previous debate (Debret and

Sverjensky, 2017; Kelley and Cottrell, 2009; Lee et al., 2010; Marschall and Schumacher, 2012; Evens et al., 2012; Breeding et al., 2004; Parkinson and Arculus, 1999). It is widely accepted that there is significant water loss during shallow subduction through the dehydration of subducted sediments but hydrous phases in the down going slab, such as lawsonite, chlorite, phengite, and serpentine retain water to greater depths (Schmidt and Poli, 1998; Poli and Schmidt, 1995). Lawsonite, $CaAl_2Si_2O_7(OH)_2$-H_2O, is an important hydrous mineral within subducting oceanic lithosphere as it contains ~11-12 wt% water (Schmidt and Poli, 1998; Poli and Schmidt, 1995). Lawsonite has been hypothesized as a key phase responsible for the release of oxidizing fluids during subduction, resulting in redox (fO_2) changes upon its breakdown associated with dehydration metamorphic reactions (Debret and Sverjensky, 2017; Groppo and Castelli, 2010).

To identify the source of oxidizing fluids and their possible effects on subduction fO_2, this study uses the exhumed rock record from the Cycladic Islands of Sifnos and Syros, Greece to constrain the fO_2 of the residual slab mineral assemblage that records redox changes resulting from specific dehydration reactions, such as the lawsonite dehydration reaction. Samples from Lago di Cignana, Western Alps, Italy were explored but did not prove adequate for this study. All information concerning the samples from Lago di Cignana, Western Alps, Italy is presented in Appendix A. There exist limited tools with which to measure the oxygen fugacity of the mineral assemblages recording potential redox effects from the breakdown of hydrous minerals within the subducting slab. The mineral garnet commonly grows during subduction and is a robust recorder of changing conditions during its formation, often spanning millions of years (Baxter and Caddick, 2013; Drgovic et al., 2012; Dragovic et al., 2015). This study uses garnet-epidote oxygen barometry (Donohue and Essene, 2000) with epidote inclusions in garnet and the surrounding garnet as oxygen barometer pairs to study the fO_2 conditions of the mineral assemblage in the down going slab (Ague et al., 2001). A record of fO_2 changes during the growth of garnet is revealed through garnet-epidote oxybarometry exploiting the use of multiple epidote inclusions, sampled radially within a single garnet grain. The results of the garnet-epidote oxybarometry therefore give a record of fO_2 change during the duration of garnet growth and provides a means to test hypotheses as to the connections between dehydration and the redox state within the residual subducting slab mineral assemblage. For example, if the garnet grew through a major dehydration reaction, such as the breakdown and dehydration of lawsonite, redox changes caused by this breakdown reaction should be recorded in growth zones of the garnet grain reflected by a systematic change in fO_2 from garnet core to rim.

This study further explores the use of iron isotopes as a tracer of redox changes in a subduction zone setting. Changes in oxidation state may be manifested in the $Fe^{3+}/\Sigma Fe$ ratio of minerals and in fractionation of iron isotopes as heavier Fe isotopes (higher $\delta^{56}Fe$ values) will be preferentially incorporated in bonds involving Fe^{3+} versus Fe^{2+} (Polyakov and Mineev, 2000; Schauble et al., 2001). Previous work has suggested that subducting slab material will lose more isotopically light iron with increased metamorphism as sulfate, hyper-saline, and carbonate fluids, fluids enriched in Fe^{2+}, are released from the slab as lighter iron isotopes are associated with lower $Fe^{3+}/\Sigma Fe$ ratios (Debret and Sverjensky, 2017). Because of this relationship, this study will explore the redox control on iron isotope fractionation using a zoned iron isotope analysis in a single garnet grain for use as an fO_2 tracer.

Chapter 1 of this thesis is the manuscript submitted to Nature Geoscience on September 18, 2018. As such, Chapter 1 is not organized in the traditional format. Chapter 1 begins Section 1.1 with the main body of text, which includes introductory material, results, and conclusions, followed by a discussion of the methods used in the study in Section 1.2. This manuscript is the result of scientific collaborative between by the lead author (Anna R. Gerrits) and coauthors Edward Inglis, Paul G. Starr, Besim Dragovic, Ethan Baxter, and Kevin Burton. The lead author (Anna R. Gerrits) is responsible for all aspects of this thesis including, SEM data, electron microprobe data, oxygen fugacity calculations, iron isotope preparation chemistry and measurements and primary paper writing of all chapters in this thesis, including the paper publication in Chapter 1. Contributions from coauthors included edits during preparation of the manuscript, Chapter 1, and, notably, Besim Dragovic is acknowledged for providing the thermodynamic modeling presented in Chapter 1.

Data presented in Chapter 1 includes oxygen fugacity values, iron isotope compositions, and thermodynamic modeling for Sifnos, Greece samples 09DSF23E, 09DSF-54A, and 06MSF-6C. Chapter 1 provides an example of two samples that are known to have growth through the lawsonite dehydration reaction, 09DSF-23E and 09DSF-54A, and one that has not, 06MSF-6C. Chapter 2 discusses additional samples from Sifnos, 09DSF-37A, and Syros, 14BSY-35C, Greece and two samples from Lago di Cignana, Western Alps, Italy, G17-S825A02 and G17-S825A03. Oxygen fugacity and iron isotope results reported in Chapter 2 provide additional support for the conclusions made in Chapter 1 and further discussion on methods, conclusions, and implications of this study.

GEOLOGIC SETTING

Several of Cycladic Islands (Aegean domain, Greece), including Sifnos and Syros islands, expose well-preserved high-pressure, low-temperature metamorphic rocks belonging to the Cycladic Blueschist Unit (CBU), the lower unit of the Attic-Cycladic crystalline complex (Figure 1 and Figure 2) (Okrusch and Brocker, 1990). The Attic-Cycladic crystalline complex stretches from Turkey to Greece and is composed of two major units separated by low-angle normal faults. The upper unit consists of a sequence of Permian age unmetamorphosed sediments, ophiolite fragments, and high-grade metamorphic rocks (Cheney et al., 2001). The lower unit contains the Cycladic Blueschist Unit (CBU) and consists of a crystalline basement overlain by thrusted sequences of metavolcanics, Mesozoic marbles, and metapelites (Okrusch and Brocker, 1990) (Figure 1 and Figure 2).

The rocks in the Cycladic Blueschist Unit are thought to have undergone two stages of metamorphism. The first metamorphic event (M_1), was a high-pressure, low temperature (HP/LT) blueschist to eclogite facies subduction related metamorphic event with peak metamorphic conditions estimated to be 550-600°C at 2.0 GPa (Schmädicke and Will, 2003, Trotet et al., 2001a) and 525-565°C at >2.1 GPa (Groppo et al., 2009). This HP/LT metamorphic event has been dated on Sifnos to 48-41 Ma using K-Ar and Rb-Sr in white micas (Altherr et al., 1979; Wijbrans et al., 1990) and Sm-Nd in garnet (Dragovic 2013) and on Syros to 53-41 Ma using Ar-Ar geochronology in white micas (Lister and Forster, 2016) and Sm-Nd in garnet (Kendall 2016). This metamorphic event has been attributed to the subduction of the Apulian microplate under the Eurasia driven by the northward movement of the African continent during the closure of the Tethys Sea

(Okrusch and Brocker, 1990; Avigad and Garfunkel, 1991; Avigad, 1993). Subsequent metamorphism (M_2) in the Cycladic Islands is recorded by a medium-pressure greenschist facies event, potentially acquired during Miocene at ca. 24-18 Ma (Altherr et al., 1979; Forster and Lister, 2005), associated with exhumation of the Attic Cycladic massif (Trotet et al., 2001). This metamorphism has overprinted some of the eclogite and blueschist facies metabasalts on Syros and Sifnos.

SAMPLE DESCRIPTIONS

Samples in this study comprise eclogite and blueschist facies metamorphic rocks. Eclogite refers to a rock with a mineral assemblage of omphacite + garnet and +/- accessory minerals including lawsonite, quartz, rutile, amphibole, phengite, paragonite, zoisite, kyanite, and coesite. Blueschist is defined by the presence of glaucophane + lawsonite/epidote +/- jadeite +/- albite +/- garnet +/- chlorite +/- muscovite.

High pressure, low temperature blueschist and eclogite samples were selected for this study because they contain large garnet porphyroblasts with epidote inclusions that may record any redox changes experienced during garnet growth. Because of their pressure-temperature history, blueschist and eclogite blocks experience multiple changes in mineral assemblage before they reach peak metamorphic temperatures, meaning that these rocks have experienced and may preserve fO_2 changes caused by the dehydration of hydrous minerals in the down going slab. While eclogite facies mineral assemblages are preserved in the majority of the samples analyzed in this study, many rocks sampled from both Sifnos and Syros, Greece are overprinted, at least in part, by blueschist and greenschist facies retrogression, accompanied by variable amounts of matrix recrystallization. Samples from Lago di Cignana show retrogressive glaucophane concentrated in compositional domains of omphacite and blueschist rich rock visible at both the outcrop and hand sample scales (Figures 2.9 & 2.10). GPS locations for each sample are presented in Table 2.1 and are discussed in detail below.

Sample 09DSF-23E is a blueschist with large porphyroblasts of garnet and epidote in a glaucophane rich matrix (Figure 2.3) collected from Sifnos, Greece in 2009 (Table 2.1 and Figure 2.1). This sample was first described in details by Dragovic (2013). The mineral assemblage for 09DSF-23E includes large garnet porphyroblasts up to 1.75cm in diameter, epidote porphyroblasts up to 1cm in length, glaucophane, phengite, rutile. Also present, but in lower abundance, are calcite, quartz, and magnetite. Garnet makes up about ~13% of the sample (Dragovic, 2013) and compositions change slightly from garnet cores ($Alm_{68}Grs_{22}Pyp_{7}Sps_{2}And_{1}$) to rims ($Alm_{67}Grs_{21}Pyp_{9}Sps_{2}And_{1}$). Mineral inclusions within garnet porphyroblasts include quartz, omphacite, epidote, albite, rutile, phengite, paragonite, glaucophane, and chloritoid.

Sample 09DSF-54A is a blueschist with large porphyroblasts of garnet and epidote in a glaucophane rich matrix (Figure 2.4) collected from Sifnos, Greece in 2009 (Table 2.1 and Figure 2.1). The mineral assemblage for 09DSF-54A includes large garnet porphyroblasts measuring up to 1.75cm in diameter, epidote porphyroblasts up to 3cm in length, glaucophane, phengite, rutile. Also present, but in lower abundance, are calcite, quartz, and magnetite/hematite. Garnet compositions change slightly from garnet cores ($Alm_{70}Grs_{19}Pyp_{4}Sps_{5}And_{1}$) to rims ($Alm_{69\text{-}74}Grs_{18\text{-}22}Pyp_{6\text{-}8}Sps_{1}And_{1}$). Mineral inclusions in garnet porphyroblasts include quartz, apatite, epidote, albite, rutile, phengite, paragonite, zircon, and glaucophane.

Sample 06MSF-6C is a blueschist with large porphyroblasts of garnet and epidote (Figure 2.5) collected from the Cheronissos area of Sifnos, Greece in 2006 (Table 2.1 and Figure 2.1). This sample was first described and is the focus of Dragovic et al., 2012. The mineral assemblage for 06MSF-6C includes large garnet porphyroblasts measuring up to 1.5cm in diameter, epidote porphyroblasts up to 1cm in diameter, glaucophane, paragonite, rutile. Also present, but in lower abundance, are phengite, quartz, jadeite, and hematite. Garnet compositions change slightly from garnet cores ($Alm_{69-71}Grs_{16-19}Pyp_{8}Sps_{4}And_{0.3-0.5}$) to rims ($Alm_{65-70}Grs_{20-22}Pyp_{8-10}Sps_{1-2}And_{0.5-0.8}$). Mineral inclusions in garnet porphyroblasts include quartz, glaucophane, epidote, rutile, pyroxene, albite, phengite, paragonite, and lower abundance of chloritoid, zircon, and lawsonite.

Sample 14BSY-35C is an eclogite with large porphyroblasts of garnet in an omphacite dominated matrix (Figure 2.6). This sample was collected from Syros, Greece in 2014 (Table 2.1 and Figure 2.2) and was described by Kendall, 2016. The mineral assemblage for 14BSY-35C includes large garnet porphyroblasts measuring up to ~1cm in diameter, acicular glaucophane up to 1cm in length, omphacite, white mica, quartz, sphene, and minor hematite/magnetite. Garnet compositions change slightly from garnet cores ($Alm_{71}Grs_{23}Pyp_{4}Sps_{0.8}And_{0.8}$) to rims ($Alm_{60}Grs_{32}Pyp_{6}Sps_{2}And_{0.2}$). Mineral inclusions in garnet porphyroblasts are visibly concentrated in garnet cores with very few inclusions in garnet rims. The most abundant mineral inclusion is quartz but also includes glaucophane, epidote, rutile, pyroxene, phengite, and paragonite.

Sample 09DSF-37A is a glaucophane schist with porphyroblasts of garnet and epidote in a glaucophane rich matrix (Figure 2.7) collected from Sifnos, Greece in 2009 (Table 2.1 and Figure 2.1). The mineral assemblage for 09DSF-37A includes garnet porphyroblasts measuring up to 3mm in diameter, epidote, glaucophane, phengite, omphacite rutile, sphene. Also present, but in lower abundance, are quartz, and magnetite/hematite. Mineral inclusions in garnet porphyroblasts include quartz, glaucophane, epidote, albite, rutile, pyroxene, phengite, paragonite, and lower abundance of chloritoid, zircon, and lawsonite.

1.0 TRACING THE SOURCE OF OXIDIZING FLUIDS IN SUBDUCTION ZONES USING IRON ISOTOPES IN GARNET

1.1 MANUSCRIPT

Anna R. Gerrits[1], Edward Inglis[2], Besim Dragovic[3,4], Paul G. Starr[1], Ethan F. Baxter[1], Kevin Burton[5]

[1]Department of Earth and Environmental Sciences, Boston College, 140 Commonwealth Avenue, Chestnut Hill, MA 02467, USA
[2]Institut de Physique du Globe de Paris, Sorbonne Paris Cité, CNRS, 1 rue Jussieu, 75238, Paris cedex 05, France
[3]Department of Geosciences, Boise State University, 1910 University Drive, Boise, ID 83725, USA
[4]Department of Geosciences, Virginia Polytechnic Institute and State University, 926 West Campus Drive, Blacksburg, VA 24060, USA
[5]Department of Earth Sciences, Durham University, Science Labs, Durham, DH1 3LE, UK

Subduction zones are the primary areas of chemical and mass transfer between the Earth's surface and the mantle. During subduction, the downgoing plate carries oxidized material into the mantle and releases large amounts of water through the breakdown of hydrous minerals (Schmidt and Poli, 1998; Magni et al., 2014). This dehydration has been linked to subduction seismicity (Olazaki and Hirth, 2016), arc volcanism (Schmidt and Poli, 1998; Tatsumi, 1986; Marschall and Schumacher, 2012), and redox (fO_2) changes in the subducting slab and overlying mantle wedge (Breeding et al., 2004; Kelley and Cottrell, 2009; Groppo and Castelli, 2010; Parkinson and Arculus, 1999; Evans et al., 2012; Debret and Syerjensky, 2017). Despite this, no petrologic record tracing the source of oxidizing fluids from the downgoing slab has yet been observed. Lawsonite, a major hydrous mineral within oceanic lithosphere, has been hypothesized as a key phase responsible for redox changes upon its breakdown and dehydration during subduction (Groppo and Castelli, 2010). Here we show a record of progressive redox change recorded in zoned garnet crystals from Sifnos, Greece that grew through lawsonite breakdown during subduction ca. 45 million years ago. Oxygen fugacities (fO_2), calculated using garnet-epidote oxybarometry for multiple growth zones within single garnet grains, have been coupled with stable Fe isotope compositions in the same growth zone. These combined measurements reveal that garnet cores grew under relatively oxidized conditions, recording higher fO_2 and lower δ^{56}Fe values, whereas garnet rims record more reduced conditions with lower fO_2 and higher δ^{56}Fe values. These data show that the redox state of the mineral assemblages within the slab became more reduced during subduction zone dehydration. This is consistent with the release of oxidizing fluids into the sub-arc mantle accompanying lawsonite breakdown and dehydration, leaving behind a progressively reduced residual slab mineral assemblage. These coupled fO_2 and Fe isotope data support the hypothesis that slab dehydration accompanying lawsonite breakdown plays an important and measureable role in the global redox budget and provides a viable mechanism for sub-arc mantle oxidation.

Oxygen fugacity (fO_2), the chemical potential of oxygen in a system, is an intensive thermodynamic property that controls the speciation of multi-valent elements, such as iron, which regulates the ability of these elements to contribute to mineral forming reactions (Frost, 1991). Because of this, fO_2 is an important chemical control in a given environment, such as a subduction zone, where the subducting slab experiences multiple changes in mineral assemblages as a result of changes in pressure-temperature (*P-T)* conditions. During subduction, components of the downgoing lithosphere, including sediments, altered mafic oceanic crust, and serpentinized mantle, carry water and other volatiles into the subduction zone. It is widely accepted that there is significant fluid loss during shallow subduction but hydrous phases in the downgoing slab, such as lawsonite, chlorite, chloritoid, phengite, and serpentine retain water to greater depths (Schmidt and Poli, 1998; Poli and Schmidt, 1995). Lawsonite, $CaAl_2Si_2O_7(OH)_2$-H_2O, is a common hydrous mineral in mafic oceanic crust and contains ~12 wt% water (Schmidt and Poli, 1998; Mangi et al., 2014; Poli and Schmidt, 1995), making the metamorphic destabilization of lawsonite an important fluid-producing reaction within subduction zones. Much debate exists about the role of slab-derived fluids in oxidizing the overlying sub-arc mantle and how such fluids can be used to explain the oxidized and volatile-rich signatures observed in arc magmas relative to their MORB or OIB counterparts (Schmidt and Poli, 1998; Tatsumi, 1986; Marschall and Schumacher, 2012; Breeding et al., 2004; Kelley and Cottrell, 2009; Groppo and Castelli, 2010; Parkinson and Arculus, 1999; Evans et al., 2012; Debret and Syerjensky, 2017; Lee et al., 2010). It has been hypothesized that dehydration of hydrous minerals, such as lawsonite, could lead to the release of oxidized fluids from the downgoing slab (Groppo and Castelli, 2010; Debret and Syerjensky, 2017). Here we present a novel petrochemical method on the scale of individual mineral growth zones to comment on the redox nature of the fluids released during key subduction dehydration events.

To identify the source of these oxidizing fluids, we use the exhumed rock record to constrain the fO_2 of the residual slab mineral assemblage, which records redox changes resulting from dehydration reactions, such as the breakdown of lawsonite. There exist limited tools with which to measure the fO_2 of the residual slab assemblages. Recent work has demonstrated the utility of garnet as a robust recorder of changing conditions during its formation and growth, often spanning millions of years (Ague et al., 2001; Baxter and Caddick, 2013; Dragovic et al., 2012; Dragovic et al., 2015). Here we present the first high precision stable Fe isotope measurements of individual garnet growth zones to examine the evolving fO_2 of the down-going slab during subduction. Changes in oxidation state are manifested in the $Fe^{3+}/\Sigma Fe$ ratio of minerals and result in a redox driven fractionation of Fe isotopes, as heavier Fe isotopes (higher $\delta^{56}Fe$ values) are preferentially incorporated in bonds involving Fe^{3+} relative to Fe^{2+} when the system is in equilibrium (Polyakoy and Mineev, 2000; Schauble and Rossman; 2001). These iron isotope measurements are coupled with garnet-epidote oxygen barometry calculations (Donohue and Essene, 2000), using multiple epidote inclusions sampled radially within a single garnet grain (Fig. 1.1), to provide a record of fO_2 change during garnet growth. Previous work on slab serpentinites has suggested that subducting slab material will lose isotopically light iron, in the form of aqueous Fe^{2+}-SO_X and Fe^{2+}-CO_X complexes, with increasing metamorphic grade as sulfate, hyper-saline, and carbonate fluids, fluids enriched in Fe^{2+}, are released from the slab (Debret and Syerjensky, 2017). Despite this, no such effect is resolvable on a whole rock scale for meta-mafic lithologies within subduction zones (Inglis et al., 2017). This study proposes the use of the relationship between the oxidation state and the isotopic composition of Fe recorded at the mineral scale, within zoned garnet crystals, as a tracer of fO_2 change during metamorphic devolatilization of subducting oceanic lithosphere.

Applying these methods, we present Fe isotope data and oxygen fugacity calculations (Fig. 1.2) for three zoned garnet crystals hosted within subducted and exhumed crustal metabasalts from Sifnos, Greece. Plotting fO_2 as ΔlogFMQ against δ^{56}Fe for samples 09DSF-23E and 09DSF-54A illustrated in Fig. 1.2, shows a significant change from more oxidized garnet cores (higher ΔlogFMQ) with a lighter Fe isotope signature (lower δ^{56}Fe) isotopes to more reduced garnet rims (lower ΔlogFMQ) with a higher δ^{56}Fe compositions. Sample 06MSF-6C shows no significant change in calculated fO_2 (ΔlogFMQ) values from garnet core to rim and only a minor variation in δ^{56}Fe, with lower δ^{56}Fe values in the garnet core than in the garnet rim (Fig. 1.2). Oxygen fugacity values calculated here are consistent with the typical range of subducted metabasaltic fO_2 values (Donohue and Essene, 2000; Boundy et al., 2002; Cao et al., 2011; Mattinson et al., 2004) in that they show more oxidized conditions, relative to the fayalite-magnetite-quartz (FMQ) buffer, than unaltered mid-ocean ridge basalt (MORB) (Kelley and Cottrell, 2009).

These data show that there is significant redox change recorded in the mafic component of the slab during subduction at the mineral scale. In order to link these redox changes recorded in garnet to key dehydration reactions, thermodynamic modelling constraints on the *P*-*T* evolution of these samples are shown in Fig. 1.3, 1.9, and 1.10. For samples 09DSF-23E (Fig. 1.3) and 09DSF-54A (Fig. 1.9), garnet growth spanned the onset of lawsonite breakdown along a representative subduction zone *P*-*T* path for Sifnos, Greece (Dragovic et al., 2012; Dragovic et al., 2015; Groppo et al., 2009). To the contrary, garnets in sample 06MSF-6C likely ceased growing prior to lawsonite breakdown (Fig. 1.10 and Dragovic et al., 2012). This provides a valid explanation for why the first two samples show significant fO_2 change whereas sample 06MSF-6C does not, and supports the hypothesis that the dehydration of lawsonite plays a key role in altering the redox state of the subducting metamorphic mineral assemblage.

While bulk rock $Fe^{3+}/\Sigma Fe$ ratios can become decoupled from the fO_2, the observed inverse correlation from garnet core to rim between increasing $\delta^{56}Fe$ values and decreasing fO_2 (Fig. 1.1D) confirms that Fe isotope fractionation is linked to changing redox conditions. To account for the observed covariation between higher fO_2 and lower $\delta^{56}Fe$ in garnet cores relative to lower fO_2 and higher $\delta^{56}Fe$ in garnet rims, we propose two possible mechanisms related to the release of oxidizing fluids. First, iron isotope fractionation occurs as an open system process, controlled by the solubility difference between Fe^{2+} and Fe^{3+}. The higher solubility of Fe^{2+} relative to Fe^{3+} (Polyakoy and Mineev, 2000; Schauble and Rossman; 2001) promotes Fe isotope fractionation as lighter Fe isotopes are complexed into oxidizing fluids (Debret et al., 2016), which are subsequently removed from the system. In this scenario the progressive removal of Fe^{2+} bearing, isotopically light fluids is recorded by prograde garnet growth in the residual source rock, and can explain the shift from light to heavy Fe isotope compositions between garnet cores and rims.

A second complementary mechanism is that Fe isotope fractionation is controlled by the bulk rock $Fe^{3+}/\Sigma Fe$ ratio in a closed system with respect to Fe, with changing oxygen fugacity. Lawsonite dehydration releases oxidizing fluids (Groppo and Castelli, 2010), changing the fO_2 of the system, leaving behind a more reduced residual mineral assemblage enriched in Fe^{2+}. This fO_2 change does not alter the whole rock Fe isotope composition, but instead, as garnet more readily incorporates isotopically light Fe^{2+}, causes a shift towards higher δ^{56}Fe values within garnet crystal rims due to simple Rayleigh fractionation. While it is difficult to determine which is the dominant mechanism responsible for the observed Fe isotope fractionation, it is plausible that during garnet growth a combination of these two mechanisms could contribute, as both are driven by the release of oxidizing fluids during progressive dehydration.

The large change in fO_2 (ΔlogFMQ) and Fe isotope compositions observed towards the garnet rim in samples 09DSF-23E (Fig. 1.1 and 1.2) and 09DSF-54A (Fig. 1.2), coincides with the interval of lawsonite breakdown and release of a free fluid phase (Fig. 1.3 and 1.9). The loss of isotopically light Fe^{2+} within fluids and the resulting re-equilibration of Fe-bearing minerals within the more reduced residue provides a mechanism for the observed Fe isotope fractionation and calculated fO_2 change seen from garnet cores to rims. We conclude that this data supports the hypothesis that the breakdown of lawsonite during subduction influences the redox state and iron isotopic signatures of the subducting mafic slab, which plays an important role in the overall global redox budget. In addition, this study provides the first evidence that core to rim Fe isotope variations in garnet are a sensitive recorder of dehydration-driven redox change occurring during metamorphism of subducting oceanic lithosphere.

Much debate exists about the cause of volatile enrichment and oxidized nature of arc magmas (Schmidt and Poli, 1998; Tatsumi, 1986; Marschall and Schumacher, 2012; Breeding et al., 2004; Kelley and Cottrell, 2009; Groppo and Castelli, 2010; Parkinson and Arculus, 1999; Evans et al., 2012; Debret and Syerjensky, 2017; Lee et al., 2010). It is widely accepted that fluids released from the subducting slab are responsible for altering the sub-arc mantle, the source region for arc magmas. A number of studies propose that these fluids, originating from dehydration of oceanic sediments, mafic crust, and serpentinized mantle, are the agents of mantle wedge oxidation (Kelley and Cottrell, 2009; Evans, 2012; Debret and Syerjensky, 2017). Alternatively, it has been suggested that the oxidation of arc magmas may occur during magmatic differentiation or degassing (Lee et al., 2010; Ming et al., 2018). This study provides evidence for redox change in the mafic component of the downgoing slab inferred to be the result of the release of oxidizing fluids during lawsonite breakdown. By fingerprinting the source of oxidizing fluids in the subducting slab, our study provides support for the idea that slab-derived fluids play an important role in the oxidation of the sub-arc mantle and related arc volcanic magmas.

1.2 METHODS

Oxygen fugacity, iron isotope, and thermodynamic modeling methods used in this study are presented before for samples 09DSF-23E, 09DSF-54A, and 06MSF-6C. All three samples are metabasalts collected from Sifnos, Greece. GPS locations for each sample are as follows: 09DSF-23E (N 37.01598°, E 24.39396°), 09DSF-54A (N 37.00930°, E 24.39360°), and 06MSF-6C (N 37.01561°, E 24.39452°).

1.2.1 Oxygen Fugacity Calculations

Oxygen fugacity methods and calculations are based on the oxygen barometer chemistry of Donohue & Essene (2002) utilizing the THERMOCALC program and thermodynamic database of Holland and Powell (1998). To ensure epidote inclusions are suitable for use in garnet-epidote oxygen barometer calculations, care was taken to identify primary epidotes, rather than compositionally patchy epidotes that reflect pseudomorphs after lawsonite. Epidote inclusions used in oxybarometry calculations (Figs 1.5, 1.6, and 1.7) are in equilibrium with the surrounding garnet and show little to no cation zonation in BSE analysis. Epidote inclusions interpreted to be lawsonite pseudomorphs shows cation zonation visible in BSE and are accompanied by either paragonite or albite, representing breakdown products of lawsonite, (Fig. 1.8) and were avoided for this study.

Garnet and epidote endmember activities (Table 1.3) were obtained at the appropriate *P-T'*s for each epidote-garnet pair (Table 1.1 and Supplementary Information) by inputting major element compositions of garnet and epidote minerals into the AX program (Tim Holland, University of Cambridge). Mineral compositions were acquired using wavelength dispersive spectrometry (WDS) on a JEOL-JXA-8200 electron microprobe at the Massachusetts Institute of Technology (Table 1.2). All spot analyses were carried out using an acceleration voltage of 15kv, a current of 20nA, and approximate spot size of 5µm. Oxygen fugacity values (Table 1.4) were calculated by imputing endmember activities of each epidote-garnet pair and the appropriate pressure and temperature into the thermodynamic modeling program, THERMOCALC (Holland and Powell, 1998; Powell and Holland, 1988; Powell and Holland, 1994) using the equation:

$$2\ Ca_2FeAl_2Si_3O_{12}(OH) = 2\ Ca_2FeAl_2Si_3O_{12} + H_2O + 1/2\ O_2 \qquad (1)$$

Epidote ($Ps_{33}Czo_{67}$) Garnet ($Alm_{33}Grs_{67}$) Fluid

Which, can be rewritten to include grossular and almandine garnet end-members:

$$12Ca_2FeAl_2Si_3O_{12}(OH) = 8Ca_3Al_2Si_3O_{12} + 4Fe_3Al_2Si_3O_{12} + 6H_2O + 3O_2 \qquad (2)$$

Epidote ($Ps_{33}Czo_{67}$) Grs garnet Alm garnet Fluid

Oxygen fugacity results are reported as ΔlogFMQ, the difference between the calculated sample fO_2 and the FMQ buffer at a given *P-T*:

$\Delta\log FMQ = (\text{Sample } fO_{2\,P\text{-}T} - FMQ_{P\text{-}T})$

To obtain ΔlogFMQ values for each fO_2 value, the FMQ buffer was recalculated using the *P-T* conditions of each garnet-epidote oxybarometer pair used in fO_2 calculations.

As stoichiometric calculations of garnet compositions based on electron microprobe measurements yield a low andradite component (>1.5% *And* for garnet core and >1% *And* for garnet rim compositions in all three samples), garnet compositions used in oxygen fugacity calculations assume all iron in garnet is Fe^{2+}. All iron in epidote mineral formulas used in oxygen fugacity calculations is assumed to be Fe^{3+}. Calculations assume a unit H_2O activity of 1 based on low salinity measurements of garnet fluid inclusions from Cycladic metabasalts (Barr, 1990). All error for ΔlogFMQ are ±0.2 log units based on the ±1kbar and ±40°C thermodynamic modeling error for *P-T* estimates presented in Palin et al. (2016).

Oxygen fugacity calculations for epidote-garnet pairs in core and rim zones use estimated pressures and temperatures of formation for each sample based on garnet isopleth thermodynamic modeling for samples 09DSF-23E (Fig. 1.10A&B), and 09DSF-54 (Fig. 1.10C&D), and 06MSF-6C (Dragovic et al., 2012). Without accurate *P-T* estimates for epidote inclusions in garnet matrix zones, *P-T*'s were estimated using a *P-T* path from Sifnos, Greece with the prograde slope of Dragovic et al. (2012), Dragovic et al. (2015), and a path curvature based on Groppo et al. (2009). In addition, a second set of fO_2 values was calculated for matrix zone inclusions using *P-T* estimates assuming a straight *P-T* path connecting garnet core and rim *P-T* values (Supplementary Information). The two sets of *P-T*s encompass the range of reasonable *P-T* paths for core to rim growth of each garnet with the resulting range of fO_2 values shown as lines in Fig. 1.4. While there is a range of matrix zone fO_2 for samples 09DSF-23E and 09DSF-54A, core and rim fO_2 values clearly show there is a change from more oxidized garnet cores to more reduced garnet rims in both samples independent of the choice of *P-T* path (Fig. 1.2). The apparent increase in fO_2 from garnet core to intermediate zones in sample 09DSF-23E (Fig 1.2) may have arisen from uncertainties in *P-T* estimates used in oxybarometer calculations for those intermediate zones.

1.2.2 Iron Isotope Analysis

Iron isotope ratios are reported as δ^{56}Fe and δ^{57}Fe using the IRMM-014 external standard with 2-standard deviation reported error (Table 1.2).

$\delta^{56}Fe = ((^{56}Fe/^{54}Fe_{sample})/(^{56}Fe/^{54}Fe_{IRMM\text{-}014})-1)*100$

$\delta^{57}Fe = ((^{57}Fe/^{54}Fe_{sample})/(^{57}Fe/^{54}Fe_{IRMM\text{-}014})-1)*100$

Garnet powders used in iron isotope measurements were cleansed of inclusions and fully dissolved at Boston College (USA) before being passed through an iron exchange chromatographic procedure and analyzed for Fe isotope ratios at Durham University (UK). Growth zones were separated in individual garnet grains using the micro-drilling techniques presented in Pollington and Baxter (2011) to obtain three zones (core, zone 2, and rim) from samples 09DSF-54A and 06MSF-6C and four zones (core, zone 2, zone 3, and rim) from sample 09DSF-23E. Each garnet zone is then crushed to a 75-150μm grain size and any visible inclusions were removed by handpicking and magnetic separation.

Samples were then put through a partial dissolution process, alternating dilute hydrofluoric and nitric acid steps to cleanse the garnet of inclusions. 10-50 mg of the picked garnet separate is heated at 120°C and sonicated in a closed beaker with 1 mL deionized Milli-Q water and 5-90 μL concentrated hydrofluoric acid added to 1 mL of Milli-Q water based on the starting amount of garnet for 120 minutes to dissolve inclusions. This acid mixture is then decanted and the garnet residue washed with 1mL of Milli-Q water four times. The residual garnet is then sonicated and heated at 120°C for 120 minutes in 2 mL 7 M nitric acid to completely dissolve any secondary fluorides. The nitric acid is decanted and the garnet residue is washed in 1mL 2 M nitric acid twice and 1mL Milli-Q water twice. This process is repeated until >50% of the original garnet has been dissolved. The inclusion-cleansed garnet residual is then fully dissolved using hydrofluoric acid, nitric acid, and hydrochloric acid.

Tests were conducted to explore potential Fe isotope fractionation during the partial dissolution process described above. Pure gem quality garnets with no visible inclusions from Mason Mountain Mine, North Carolina were crushed and subjected to various partial dissolution procedures. To test potential fractionation due to the acids used, garnet was partially dissolved separately in 7 M nitric, concentrated HF acid, and was also subjected to the full partial dissolution procedure described above. The resulting δ^{56}Fe compositions are all within error between pure garnet with no partial dissolution (0.015 ± 0.046), garnet after partial dissolution cleansing in nitric acid (0.085 ± 0.028), garnet after partial dissolution cleansing in HF and nitric acid (0.08 ± 0.05), and garnet subjected to the full nitric-HF multi-stage partial dissolution technique (0.06 ± 0.033). While the starting garnet may not have been perfectly pure, the partial dissolution cleansing removed those inclusions (with lower δ^{56}Fe) leaving behind a pure garnet with higher δ^{56}Fe. Importantly, after this initial stage of partial dissolution cleaning, all subsequent steps to further treat the garnets yielded identical δ^{56}Fe. This indicates the success of the method in removing the effects of non-garnet inclusions, but not altering the δ^{56}Fe of the pure garnet itself. Based on these results, the HNO_3-HF multi-step partial dissolution was deemed appropriate to cleanse garnet of inclusions without fractionating iron isotope compositions. All garnet separates used in this study were subject to identical cleansing and preparation procedure. Sample drilling, crushing, and the partial and full dissolution processes were completed in the clean lab at Boston College.

Iron isotope measurements of the minerals were analyzed at Durham University between August and October 2017. The quantitative purification of Fe from the matrix elements was achieved using a protocol adapted from Dauphas et al. (2004). In this method 1.2 ml of BioRad AG1-X8 (200-400 mesh) anion exchange resin was packed onto 11.5 ml total capacity polypropylene columns, which was cleaned with passes of 10 ml MQ H_2O and 10 ml 6 M HCl repeated 4 times each. The resin was preconditioned with 2 ml of 6 M HCl and the sample loaded onto the column in 250 µl of 6 M HCl. The matrix was eluted from the retained Fe species by adding 8 ml of 6 M HCl and discarded. Iron was quantitatively recovered from the column by adding 9 ml 0.4 M HCl, and subsequently collected into clean 15 ml Savillex Teflon beakers. The pure Fe solution was evaporated to dryness and brought back into solution in 2 ml of 0.5 M HNO_3 prior to analysis by mass spectrometry. Prior calibration of this chromatographic ion exchange protocol demonstrated that the recovered Fe fraction was devoid of any isobaric elements (namely Cr and Ni) and totaled >99% of the Fe loaded into the column.

Iron isotope abundances were measured on a Thermo Scientific Neptune Plus MC-ICP-MS at Durham following the procedure of Weyer and Schwieters (2003). The instrument was run in medium-resolution mode which gave a typical mass resolving power of ~6500, adequate to discriminate between the $^{40}Ar^{14}N^+$, $^{40}Ar^{16}O^+$ and $^{40}Ar^{16}OH^+$ polyatomic species that are isobaric on the $^{54}Fe^+$, $^{56}Fe^+$, and $^{57}Fe^+$ masses respectively. Samples were introduced to the plasma interface using an Elemental Scientific SIS quartz spray chamber coupled with a PFA 50 µl/min nebulizer. All of the Fe masses were collected, as were $^{53}Cr^+$ and $^{60}Ni^+$, in the movable faraday collectors, mounted within the back end of the instrument. $^{53}Cr^+$ and $^{60}Ni^+$ were used to correct, using the natural abundances, for any isobaric interference from these elements on the $^{54}Fe^+$ and $^{58}Fe^+$ masses. In all cases this correction had no effect on the calculated ratio as Cr and Ni were quantatively removed from the sample solution prior to analysis by column chemistry. Instrumental mass bias was corrected using standard sample bracketing, where IRMM-014 was used as the bracketing standard. Precision and accuracy was assessed by measuring both an in-house secondary reference solution (Durham FeWire) and an external geo-reference material (USGS BIR 1). A total of 81 Durham FeWire analyses gave a mean of δ^{56}Fe of +0.23 ± 0.04 ‰ and a δ^{57}Fe of +0.37 ± 0.06 ‰ (n=81). Two aliquots of the BIR-1 geo-reference material were processed through two different batches of chemistry and analyzed a total of 4 times each. This gave an average δ^{56}Fe of +0.06 ± 0.028 ‰ and a δ^{57}Fe of +0.09 ± 0.021 ‰, which is in excellent agreement with published values for this standard (Weyer and Schwieters, 2003; Millet et al., 2012; Hibbert et al., 2012). Total procedural blank yielded <6ng Fe, which is negligible when compared to the total amount of Fe processed through the columns. The Fe isotope data for the samples analyzed as part of this study are reported in Table 1.2 with error of two-standard deviation of four isotopic analyses for each sample.

1.2.3 Thermodynamic Modeling

To constrain the *P-T* conditions for garnet growth and the evolution of the metamorphic mineral assemblage during progressive subduction, *P-T* pseudosections and mineral modal plots were constructed using the thermodynamic program Perple_X (version 6.7.5) (Connolly, 2009) and the ‘ds 5.5’ update to the Holland and Powell (1998) internally-consistent dataset. The chemical system MnO-Na_2O-CaO-K_2O-FeO-MgO-Al_2O_3-SiO_2-H_2O-TiO_2-Fe_2O_3 (MnNCKFMASHTO) was used for all modelling. The following activity-composition models were used for phases involving solid solution: pyroxene and amphibole[42], garnet (White et al., 2007), white mica (Auzanneau et al., 2010; Coggan and Holland, 2002), chlorite (Powell and Holland, 1998), feldspar (Fuhrman and Lindsley, 1988), epidote and chloritoid (Holland and Powell, 1998), spinel (White et al., 2002a), ilmenite (White et al., 2002b), and carbonates (Holland and Powell, 2003). In all the calculations, quartz, lawsonite, rutile, kyanite, and sphene were assumed to be pure, with phase equilibria calculations run in fluid-undersaturated conditions (see discussion below). Fe_2O_3 contents for the bulk compositions were evaluated by combining the average composition of phases with their respective volume abundances. Ferric iron contents of mineral phases were estimated from electron microprobe analyses using the AX program (Tim Holland, University of Cambridge).

Bulk compositions used for all phase equilibria calculations are shown in Table 1.3, along with $Fe^{3+}/\Sigma Fe$ (by mole fraction) used for each sample. Whole rock compositions were used in calculation of the *P*-*T* conditions of garnet growth initiation (garnet cores). As garnet is chemically zoned in both samples and the sequestration of components in zoned crystals can have a significant effect on both the effective composition of the rock and the resultant mineralogy (Marmo et al., 2002), independent bulk compositions of rock matrices were obtained by physical separation of garnet crystals from a whole rock volume. All bulk compositions (whole rocks and matrices) were determined by X-ray fluorescence (XRF) spectroscopy using a Phillips 2404 XRF vacuum spectrometer at Franklin and Marshall College.

Path dependent forward models take into account the continuous fractionation of garnet and water, following Baxter and Caddick (2013), with a sequence of regularly spaced *P-T* increments, where at each increment, the composition and modal abundance of all stable phases is predicted. The models were run at 0.5˚C increments, with variable pressure increments. The *P-T* paths used for this modelling (Fig. 1.3A) were chosen based on the individual *P-T* gradients derived from Dragovic et al. (2015), also utilizing additional *P-T* constraints from Dragovic et al. (2012). The whole rock compositions were used as the initial bulk compositions for the phase fractionation calculations. The initial fluid contents for the phase fractionation calculations were determined based on repeat phase fractionation calculations to best model the observed mineralogy (of garnet inclusions and matrix) and volumetric mineral abundances. In order to reproduce the observed mineralogy, including the stable coexistence of lawsonite and epidote during initial garnet growth, fluid undersaturated conditions were required. The initial fluid contents chosen for modelling of samples 09DSF-23E, 09DSF-54A, and 06MSF-6C are 6.0%, 4.0%, and 2.0%, respectively. Fluid in samples 09DSF-23E and 09DSF-54A were considered to be a fixed fluid H_2O–CO_2 compositions of 1 mol.% CO_2 – 99 mol.% H_2O (09DSF-23E) and 10 mol.% CO_2 – 90 mol.% H_2O (09DSF-54A). Fluid in sample 06MSF-6C was considered to be pure H_2O. These fluid compositions were estimated based on petrographic observations.

P-T pseudosections were calculated for the *P-T* range of 1.0-2.5 GPa and 400-650˚C using the same a-x models listed above. The bulk composition used for the pseudosection modelling of each sample represents the effective bulk composition (garnet and water fractionated) calculated at 500˚C along the phase fractionation path. The fluid contents used for the pseudosections that estimate the *P*-*T* of garnet crystal cores are the same as those used as the initial fluid content for the phase fractionation calculations. For the pseudosections that estimate the *P*-*T* conditions of garnet crystal rims, the fluid content was based on predictions from the phase fractionation calculations for the remnant fluid content at the assumed *P*-*T* conditions of garnet rim growth (3.0% for 09DSF-23E and 2.7% for 09DSF-54A). An iterative analysis of fluid content resulted in broadly similar *P*-*T* pseudosections and predicted garnet rim *P*-*T* conditions.

1.3 TABLES

Table 1.1: Reported $f\mathrm{O}_2$, **Δ**logFMQ, and error values for each garnet-epidote inclusion pair for samples 09DSF-23E, 09DSF-54A, and 06MSF-6C with *PT*s used in calculations. The distance of each epidote inclusion from the core of the garnet also reported. This table is Extended Data Table 1 in the manuscript.

	Epidote Inclusion	**Distance from Core (mm)**	**T (°C)**	**P (kbar)**	**$f\mathrm{O}_2$ (log)**	**FMQ (log)**	**ΔlogFMQ**	**$f\mathrm{O}_2$ error**
09DSF-23E	Ep 1	11.48	555	16	-17.6	-19.6	2	0.2
	Ep 2	11.04	555	16	-17.1	-19.6	2.5	0.2
	Ep 4	9.73	560	23	-15.3	-18.7	3.4	0.2
	Ep 6	8.33	520	22.25	-17.2	-20.2	3	0.2
	Ep 7	7.91	520	22.25	-16.7	-20.2	3.5	0.2
	Ep 9	6.87	480	21.5	-19.1	-21.9	2.8	0.2
	Ep 11	5.95	480	21.5	-19.2	-21.9	2.7	0.2
	Ep 14	4.21	480	21.5	-18.9	-21.9	3	0.2
	Ep 16	3.03	520	22.25	-16.6	-20.2	3.6	0.2
	Ep 18	1.60	560	23	-15.4	-18.7	3.3	0.2
	Ep 19	1.11	560	23	-15.1	-18.7	3.6	0.2
	Ep 21	5.32	555	16	-17.4	-19.6	2.2	0.2
09DSF-54A	Ep 7	4.43	584	21.2	-14.4	-18.1	3.7	0.2
	Ep 11	3.01	584	23	-14	-17.9	3.9	0.2
	Ep 12	2.22	535	22.75	-15.5	-19.6	4.1	0.2
	Ep 16	1.81	535	22.75	-15.8	-19.6	3.8	0.2
	Ep 17	1.34	535	22.75	-15.4	-19.6	4.2	0.2
	Ep 20	0.94	487	22.5	-17.4	-21.5	4.1	0.2
	Ep 2	1.01	487	22.5	-17.8	-21.5	3.7	0.2
	Ep 24	0.25	487	22.5	-17.6	-21.5	3.9	0.2
	Ep 29	2.75	584	23	-13.6	-17.9	4.3	0.2
	Ep 31	3.30	584	23	-13.7	-17.9	4.2	0.2
	Ep 36	3.97	584	21.2	-14.7	-18.1	3.4	0.2
	Ep 37	4.31	584	21.2	-14.8	-18.1	3.3	0.2
	Ep 38	4.35	584	21.2	-14.4	-18.1	3.7	0.2
06MSF-6C	Ep 6	2.05	535	21.5	-16.6	-19.7	3.1	0.2
	Ep 11	0.25	470	20.2	-19.1	-22.5	3.4	0.2
	Ep 13	1.16	490	20.6	-18.3	-21.6	3.3	0.2
	Ep 16	2.79	500	20.8	-18.2	-21.1	2.9	0.2
	Ep 20	4.78	520	21.2	-16.8	-20.3	3.5	0.2
	Ep 21	5.23	530	21.4	-16.9	-19.9	3	0.2
	Ep rim	6.62	560	22	-15.1	-18.8	3.7	0.2

Table 1.2: Reported $\delta^{56/54}$Fe and $\delta^{57/54}$Fe values of garnet zones from samples 09DSF-23E, 09DSF-54A, and 06MSF-6C using the IRMM-014 external standard with 2-standard deviation error reported. This table is Extended Data Table 2 in the manuscript.

Sample	**Garnet Zone**	**$\delta^{56/54}$FeIRMM14 (‰)**	**$\delta^{56/54}$ Error (‰)**	**$\delta^{57/54}$FeIRMM14 (‰)**	**$\delta^{57/54}$ Error (‰)**
09DSF-23E	Core	-0.36	±0.02	-0.48	±0.09
	Zone 2	-0.3	±0.04	-0.44	±0.02
	Zone 3	-0.24	±0.04	-0.37	±0.03
	Rim	-0.1	±0.02	-0.24	±0.16
09DSF-54A	Core	-0.48	±0.04	-0.69	±0.04
	Zone 2	-0.48	±0.04	-0.63	±0.11
	Rim	-0.33	±0.05	-0.47	±0.07
06MSF-6C	Core	-0.45	±0.04	-0.65	±0.05
	Zone 2	-0.4	±0.03	-0.58	±0.03
	Rim	-0.34	±0.025	-0.48	±0.04

Table 1.3: Major element whole rock bulk chemistry, matrix bulk chemistry, and fluid content used in thermodynamic modeling of samples 09DSF-23E, 09DSF-54A, and 06MSF-6C reported in Extended Data Figure 1.6 and Extended Data Figure 1.7. Ferric/ferrous iron was estimated based on mineral mode and chemistry. This table is Extended Data Table 3 in the manuscript.

wt%	**09DSF-23E Whole Rock**	**09DSF-23E Matrix**	**09DSF-54A Whole Rock**	**09DSF-54A Matrix**	**06MSF-6C Whole Rock**
SiO_2	49.53	51.55	51.02	51.68	53.15
TiO_2	1.12	1.2	1.43	1.49	1.07
Al_2O_3	17.51	16.69	14.53	14.3	13.77
FeO	8.35	4.42	6.8	10.18	9.19
Fe_2O_3	3.98	5.18	7.55	2.83	4.15
MnO	0.16	0.02	0.11	0.07	0.14
MgO	4.95	0.11	4.43	4.56	5.65
CaO	8.59	8.06	5.89	6.18	2.42
Na_2O	2.78	3.02	5.72	5.96	5.3
K_2O	1.05	0.86	1.25	1.3	0.99
Total	98.02	91.11	98.73	98.55	95.83
$Fe^{3+}/\Sigma Fe$	0.3	0.3	0.5	0.5	0.2
Fluid content (wt% H_20)	6.0	3.0	4.0	2.7	2

Table 1.4: Major element epidote and garnet compositions used in activity and oxybarometry calculations for sample 09DSF-23E analyzed using the electron microprobe at MIT. This table is part of the Supplementary Information Data in the manuscript.

Inclusion	**Composition**										
	Cr_2O_3	**Al_2O_3**	**CaO**	**MnO**	**Na_2O**	**TiO_2**	**SiO_2**	**K_2O**	**FeO**	**MgO**	**Total**
Ep 1	0	27.95	23.9	0.1957	0	0.2066	38.03	0	8.26	0.0142	98.5565
Ep 2	0	26.39	23.78	0.1804	0	0.0318	37.39	0	9.79	0.0227	97.5849
Ep 4	0	26.41	23.26	0.0359	0	0.0619	37.61	0	9.88	0.0297	97.2876
Ep 6	0	26.15	23.44	0.2899	0	0.0522	36.95	0	10.34	0.0097	97.2318
Ep 7	0	25.19	23.57	0.1691	0	0.0036	37.05	0.0006	11.47	0.0059	97.4593
Ep 9	0	26.43	23.6	0.0946	0	0.0503	38	0	10.68	0	98.8549
Ep 11	0	28.11	23.86	0.1579	0	0.0554	37.86	0	7.92	0.0351	97.9985
Ep 14	0	26.63	23.64	0.1605	0.0021	0.0156	37.38	0	9.84	0.0154	97.6837
Ep 16	0	25.36	23.67	0.2081	0	0.03	37.59	0	10.85	0.0014	97.7096
Ep 18	0.0026	27.5	23.6	0.1312	0	0.0872	37.41	0	9.08	0.0331	97.8442
Ep 19	0	25.58	23.32	0.4454	0	0.0593	37.88	0	11.12	0	98.4048
Ep 21	0	26.67	23.14	0.2073	0.0107	0.1867	37.48	0	9.7	0.0174	97.4121
Gt by ep 1	0.0085	22.08	8.05	0.5269	0.0306	0.0461	38.05	0	31.37	2.47	102.632
Gt by ep 2	0.0023	21.87	7.75	0.968	0.1151	0.1033	37.56	0	31.25	2.31	101.9286
Gt by ep 4	0.0321	21.88	7.67	1.0149	0.1026	0.089	37.62	0	31.49	2.03	101.9285
Gt by ep 6	0	21.88	8.28	0.9255	0.0644	0.1389	37.72	0.0015	32.1	1.66	102.7703
Gt by ep 7	0.0169	21.68	7.45	0.9021	0.062	0.0832	37.52	0	32.4	1.69	101.8042
Gt by ep 9	0.0152	21.63	8.38	0.9385	0.08	0.1599	37.39	0.003	32.1	1.6444	102.3409
Gt by ep 11	0	21.74	8.05	0.9992	0.0232	0.1043	37.72	0	31.8	1.73	102.1667
Gt by ep 14	0.0213	21.79	7.28	1.0295	0.0362	0.0781	37.75	0.0098	32.6	1.84	102.4348
Gt by ep 16	0.0371	21.78	7.29	1.0633	0.0569	0.1007	37.62	0.0021	32.55	1.85	102.35
Gt by ep 18	0.023	21.94	7.13	1.0592	0.0723	0.0611	37.38	0	32.34	2.14	102.1455
Gt by ep 19	0.0361	21.82	7.44	1.0196	0.0847	0.1722	37.7	0.0066	31.79	2.25	102.3191
Gt by ep 21	0	21.78	7.82	0.5792	0.0357	0.0596	37.8	0.009	31.07	2.5	101.6535

Table 1.5: Major element epidote and garnet compositions used in activity and oxybarometry calculations for sample 09DSF-54A analyzed using the electron microprobe at MIT. This table is part of the Supplementary Information Data in the manuscript.

Inclusion	**Composition**									
	Cr_2O_3	Al_2O_3	CaO	MnO	Na_2O	TiO_2	SiO_2	K_2O	FeO	MgO	Total
Ep 7	0	23.33	23.19	0	0.0022	0	38.17	0.0141	13.31	0.0255	98.0418
Ep 11	0	23.98	22.97	0	0.0198	0	38.2	0	12.65	0.0393	97.8591
Ep 12	0	21.8	23.3	0	0	0	37.98	0	14.87	0.0103	97.9604
Ep 16	0	25.34	23.14	0	0	0	38.41	0.0027	11.06	0	97.9528
Ep 17	0	23.33	22.73	0	0	0	38.33	0.0436	13.32	0.0044	97.7581
Ep 20	0	22.92	22.89	0	0.0446	0	38.19	0.0177	14.07	0	98.1323
Ep 2	0	25.13	23.53	0	0	0	38.42	0.0257	10.89	0	97.9958
Ep 24	0	24.71	23.13	0	0.0454	0	38.37	0	11.14	0	97.3955
Ep 29	0	23.39	23.03	0	0.0355	0	37.53	0.0012	13.44	0.0614	97.4882
Ep 31	0	23.47	23.31	0	0.044	0	38.42	0.0035	12.72	0.1204	98.088
Ep 36	0	26.78	23.85	0	0	0	37.85	0	9.92	0	98.4
Ep 37	0	27.44	24.09	0	0	0	39.08	0	8.44	0.0927	99.1428
Ep 38	0	25.18	23.66	0	0.0108	0	38.5	0	11.09	0.0151	98.456
Gt by ep 7	0.0123	21.79	7.64	0.526	0.0592	0.0435	37.49	0	32.58	1.96	102.101
Gt by ep 11	0.0116	21.62	7.1	0.5526	0	0.0495	37.21	0.0036	33.72	1.5405	101.8077
Gt by ep 12	0.0417	21.42	7.1	0.6844	0.0131	0.0894	37.39	0	34.12	1.2953	102.1538
Gt by ep 16	0.0438	21.48	6.7	1.0004	0.0367	0.1039	37.3	0.0021	34.26	1.1578	102.0846
Gt by ep 17	0.0255	21.79	6.47	1.49	0.0105	0.0674	37.26	0	34.44	1.0624	102.6157
Gt by ep 20	0.0316	21.42	6.74	1.77	0.0211	0.0935	37.22	0	34.4	0.9958	102.6919
Gt by ep 2	0.015	21.34	7.22	1.67	0.0158	0.0882	37.25	0	34.09	0.9861	102.675
Gt by ep 24	0.05	21.49	6.53	2.18	0.0079	0.0756	37.33	0.0051	33.81	0.9682	102.4467
Gt by ep 29	0.0027	21.37	6.88	1.89	0.0079	0.0802	37.28	0.0018	34.18	0.99	102.6825
Gt by ep 31	0.0166	21.25	7.13	1.43	0.0131	0.1156	37.18	0	34.16	1.0137	102.309
Gt by ep 36	0.0372	21.38	7.07	0.8002	0.0105	0.1179	37.32	0.0036	34.37	1.1517	102.2611
Gt by ep 37	0.0178	21.29	7.28	0.6685	0.0183	0.0838	37.56	0.0071	34.13	1.2375	102.293
Gt by ep 38	0.0178	21.29	7.28	0.6685	0.0183	0.0838	37.56	0.0071	34.13	1.2375	102.293

Table 1.6: Major element epidote and garnet compositions used in activity and oxybarometry calculations for sample 06MSF-6C analyzed using the electron microprobe at MIT. This table is part of the Supplementary Information Data in the manuscript.

Inclusion	Composition										
	Cr_2O_3	Al_2O_3	CaO	MnO	Na_2O	TiO_2	SiO_2	K_2O	FeO	MgO	Total
Ep 6	0	26.3	23.52	0.2452	0.0513	0.359	37.39	0.003	9.55	0.0318	97.4503
Ep 11	0.0307	23.95	22.63	0.3904	0.0397	0.0662	37.1	0.0086	12.12	0	96.3357
Ep 13	0	26.28	23.48	0.3019	0.0172	0.018	37.56	0.0021	9.99	0	97.6492
Ep 16	0	26.67	23.59	0.3491	0.0343	0.0498	36.97	0.0047	9.77	0	97.438
Ep 20	0.03	23.41	23.19	0.197	0.0513	0.1187	37.29	0.0077	13.34	0	97.6348
Ep 21	0	25.19	22.81	0.5854	0	0.0783	37.12	0.005	11.35	0	97.1388
Ep Rim	0.0301	23.36	23.14	0.1777	0.0289	0.0424	37.2	0.0186	12.97	0	96.9677
Gt by ep 6	0.0563	21.81	7.53	1.0537	0.0257	0.0884	37.27	0.0021	31.54	1.96	101.3361
Gt by ep 11	0.0622	21.61	6.86	1.81	0.0104	0.1118	37.16	0.0072	32.26	1.79	101.6815
Gt by ep 13	0.0218	21.74	6.65	1.51	0.07	0.0745	37.53	0.0024	32.3	1.91	101.8086
Gt by ep 16	0.0422	21.58	7.21	1.1663	0	0.1213	37.39	0.0087	31.4	1.91	100.8284
Gt by ep 20	0.0236	21.78	7.63	0.8699	0.0026	0.0721	37.44	0.0033	31.23	2.15	101.2014
Gt by ep 21	0.0413	21.8	8.2	0.8393	0.0511	0.0727	37.46	0	30.78	2.11	101.3543
Gt by rim	0.0229	21.87	7.51	0.6195	0.0563	0.0204	37.44	0.017	31.74	1.83	101.126

Table 1.7: Epidote and garnet endmember activities calculated using the AX program for high PTs (first half of table) and low PTs (second half of table) used in oxybarometry calculations for sample 09DSF-23E. This table is part of the Supplementary Information Data in the manuscript.

Inclusion	**Temperature (°C)**	**Pressure (kbar)**	**Activity**						
			py	**gr**	**alm**	**spss**	**andr**	**cz**	**ep**
Ep 1	555	16						0.58	0.43
Ep 2	555	16						0.48	0.53
Ep 4	560	23						0.47	0.51
Ep 6	520	22.25						0.47	0.54
Ep 7	520	22.25						0.39	0.62
Ep 9	480	21.5						0.44	0.55
Ep 11	480	21.5						0.6	0.42
Ep 14	480	21.5						0.49	0.52
Ep 16	520	22.25						0.39	0.61
Ep 18	560	23						0.56	0.44
Ep 19	560	23						0.38	0.57
Ep 21	555	16						0.49	0.48
Gt by ep 1	555	16	0.0029	0.02	0.27	0.00000			
Gt by ep 2	555	16	0.00251	0.018	0.26	0.00001			
Gt by ep 4	560	23	0.0017	0.017	0.28	0.00001			
Gt by ep 6	520	22.25	0.00105	0.021	0.29	0.00000			
Gt by ep 7	520	22.25	0.00105	0.016	0.32	0.00000			
Gt by ep 9	480	21.5	0.00115	0.022	0.27	0.00000			
Gt by ep 11	480	21.5	0.00123	0.02	0.3	0.00001			
Gt by ep 14	480	21.5	0.00137	0.0155	0.32	0.00001			
Gt by ep 16	520	22.25	0.00132	0.015	0.31	0.00001			
Gt by ep 18	560	23	0.00191	0.014	0.29	0.00001			
Gt by ep 19	560	23	0.0022	0.0159	0.28	0.00001			
Gt by ep 21	555	16	0.00302	0.019	0.27	0.00000			
Ep 1	555	16						0.58	0.43
Ep 2	555	16						0.48	0.53
Ep 4	530	17.8						0.47	0.51
Ep 6	505	19.7						0.47	0.54
Ep 7	505	19.7						0.39	0.62
Ep 9	480	21.5						0.44	0.55
Ep 11	480	21.5						0.6	0.42
Ep 14	480	21.5						0.49	0.52
Ep 16	505	19.7						0.39	0.62
Ep 18	530	17.8						0.56	0.45
Ep 19	530	17.8						0.38	0.58
Ep 21	555	16						0.49	0.48
Gt by ep 1	555	16	0.0029	0.02	0.27	0.00000			
Gt by ep 2	555	16	0.00251	0.018	0.26	0.00001			
Gt by ep 4	530	17.8	0.00179	0.0174	0.28	0.00001			
Gt by ep 6	505	19.7	0.00108	0.021	0.29	0.00000			
Gt by ep 7	505	19.7	0.00107	0.0162	0.32	0.00000			
Gt by ep 9	480	21.5	0.00115	0.022	0.27	0.00000			
Gt by ep 11	480	21.5	0.00123	0.02	0.3	0.00001			
Gt by ep 14	480	21.5	0.00137	0.0155	0.32	0.00001			
Gt by ep 16	505	19.7	0.00136	0.0152	0.31	0.00001			
Gt by ep 18	530	17.8	0.002	0.0143	0.29	0.00001			
Gt by ep 19	530	17.8	0.0023	0.0162	0.28	0.00001			
Gt by ep 21	555	16	0.00302	0.019	0.27	0.00000			

Table 1.8: Epidote and garnet endmember activities calculated using the AX program for high PTs (first half of table) and low PTs (second half of table) used in oxybarometry calculations for sample 09DSF-54A. This table is part of the Supplementary Information Data in the manuscript.

Inclusion	**T (°C)**	**P (kbar)**	**Activity**						
			py	gr	alm	spss	andr	cz	ep
Ep 7	584	21.2						0.28	0.61
Ep 11	584	23						0.22	0.68
Ep 12	535	22.75						0.13	0.76
Ep 16	535	22.75						0.35	0.59
Ep 17	535	22.75						0.21	0.67
Ep 20	487	22.5						0.21	0.69
Ep 2	487	22.5						0.18	0.72
Ep 24	487	22.5						0.31	0.64
Ep 29	584	23						0.24	0.68
Ep 31	584	23						0.23	0.68
Ep 36	584	21.2						0.49	0.51
Ep 37	584	21.2						0.5	0.49
Ep 38	584	21.2						0.35	0.62
Gt by ep 7	584	21.2	0.000231	0.0129	0.34	0.000054			
Gt by ep 11	584	23	0.00147	0.0166	0.3	0.000001			
Gt by ep 12	535	22.75	0.00045	0.0133	0.37	0.000003			
Gt by ep 16	535	22.75	0.000323	0.0113	0.38	0.000001			
Gt by ep 17	535	22.75	0.000246	0.01	0.38	0.00004			
Gt by ep 20	487	22.5	0.00026	0.0102	0.38	0.000041			
Gt by ep 2	487	22.5	0.000227	0.011	0.36	0.000067			
Gt by ep 24	487	22.5	0.000205	0.0105	0.37	0.00013			
Gt by ep 29	584	23	0.000193	0.0109	0.35	0.000079			
Gt by ep 31	584	23	0.00211	0.012	0.35	0.000034			
Gt by ep 36	584	21.2	0.000299	0.0125	0.37	0.000002			
Gt by ep 37	584	21.2	0.00037	0.013	0.37	0.000003			
Gt by ep 38	584	21.2	0.00037	0.013	0.37	0.000003			
Ep 7	584	21.2						0.28	0.61
Ep 11	550	21.6						0.22	0.68
Ep 12	515	22						0.13	0.76
Ep 16	515	22						0.35	0.59
Ep 17	515	22						0.21	0.68
Ep 20	487	22.5						0.21	0.69
Ep 2	487	22.5						0.18	0.72
Ep 24	487	22.5						0.31	0.64
Ep 29	550	21.6						0.24	0.69
Ep 31	550	21.6						0.23	0.69
Ep 36	584	21.2						0.49	0.51
Ep 37	584	21.2						0.5	0.49
Ep 38	584	21.2						0.35	0.62
Gt by ep 7	584	21.2	0.000231	0.0129	0.34	0.000054			
Gt by ep 11	550	21.6	0.00147	0.0166	0.3	0.000001			
Gt by ep 12	515	22	0.00047	0.0135	0.37	0.000003			
Gt by ep 16	515	22	0.000333	0.0115	0.38	0.000001			
Gt by ep 17	515	22	0.000341	0.0116	0.38	0.000012			
Gt by ep 20	487	22.5	0.00026	0.0102	0.38	0.000041			
Gt by ep 2	487	22.5	0.000227	0.011	0.36	0.000067			
Gt by ep 24	487	22.5	0.000205	0.0105	0.37	0.00013			
Gt by ep 29	550	21.6	0.000203	0.011	0.35	0.000079			
Gt by ep 31	550	21.6	0.00223	0.0122	0.35	0.000034			
Gt by ep 36	584	21.2	0.000299	0.0125	0.37	0.000002			
Gt by ep 37	584	21.2	0.00037	0.013	0.37	0.000003			
Gt by ep 38	584	21.2	0.00037	0.013	0.37	0.000003			

Table 1.9: Epidote and garnet endmember activities calculated using the AX program (see methods) used in oxybarometry calculations for sample 06MSF-6C. This table is part of the Supplementary Information Data in the manuscript.

Inclusion	**Activity**						
	py	**gr**	**alm**	**spss**	**andr**	**cz**	**ep**
Ep 6						0.48	0.52
Ep 11						0.29	0.65
Ep 13						0.46	0.54
Ep 16						0.51	0.51
Ep 20						0.25	0.71
Ep 21						0.38	0.56
Ep rim						0.26	0.69
Gt by ep 6	0.00166	0.0171	0.29	0.00014			
Gt by ep 11	0.00133	0.0134	0.3	0.000073			
Gt by ep 13	0.00142	0.012	0.32	0.000042			
Gt by ep 16	0.00147	0.0156	0.32	0.00002			
Gt by ep 20	0.00213	0.0183	0.29	0.0000079			
Gt by ep 21	0.00199	0.021	0.27	0.0000069			
Gt by ep rim	0.00126	0.0164	0.31	0.0000029			

Table 1.10: Reported *f*O_2, **Δ**logFMQ, and error values for each garnet-epidote inclusion pair for samples 09DSF-23E and 09DSF-54A with low *PT*s used in calculations. This table is part of the Supplementary Information Data in the manuscript.

Sample	**Epidote Inclusion**	**T (°C)**	**P (kbar)**	***f*O_2 (log)**	**FMQ**	**ΔlogFMQ**	***f*O_2 error**
09DSF-23E	Ep 1	555	16	-17.6	-19.6	2	0.2
	Ep 2	555	16	-17.1	-19.6	2.5	0.2
	Ep 4	530	17.8	-17.8	-20.3	2.5	0.2
	Ep 6	505	19.7	-18.5	-21.1	2.6	0.2
	Ep 7	505	19.7	-18	-21.1	3.1	0.2
	Ep 9	480	21.5	-19.1	-21.9	2.8	0.2
	Ep 11	480	21.5	-19.2	-21.9	2.7	0.2
	Ep 14	480	21.5	-18.9	-21.9	3	0.2
	Ep 16	505	19.7	-17.9	-21.1	3.2	0.2
	Ep 18	530	17.8	-17.8	-20.3	2.5	0.2
	Ep 19	530	17.8	-17.4	-20.3	2.9	0.2
	Ep 21	555	16	-17.4	-19.6	2.2	0.2
09DSF-54A	Ep 7	584	21.2	-14.4	-18.1	3.7	0.2
	Ep 11	550	21.6	-15.5	-19.2	3.7	0.2
	Ep 12	515	22	-16.5	-20.4	3.9	0.2
	Ep 16	515	22	-16.8	-20.4	3.6	0.2
	Ep 17	515	22	-16.4	-20.4	4	0.2
	Ep 20	487	22.5	-17.4	-21.5	4.1	0.2
	Ep 2	487	22.5	-17.8	-21.5	3.7	0.2
	Ep 24	487	22.5	-17.6	-21.5	3.9	0.2
	Ep 29	550	21.6	-15.2	-19.2	4	0.2
	Ep 31	550	21.6	-15.3	-19.2	3.9	0.2
	Ep 36	584	21.2	-14.7	-18.1	3.4	0.2
	Ep 37	584	21.2	-14.8	-18.1	3.3	0.2
	Ep 38	584	21.2	-14.4	-18.1	3.7	0.2

1.4 FIGURES

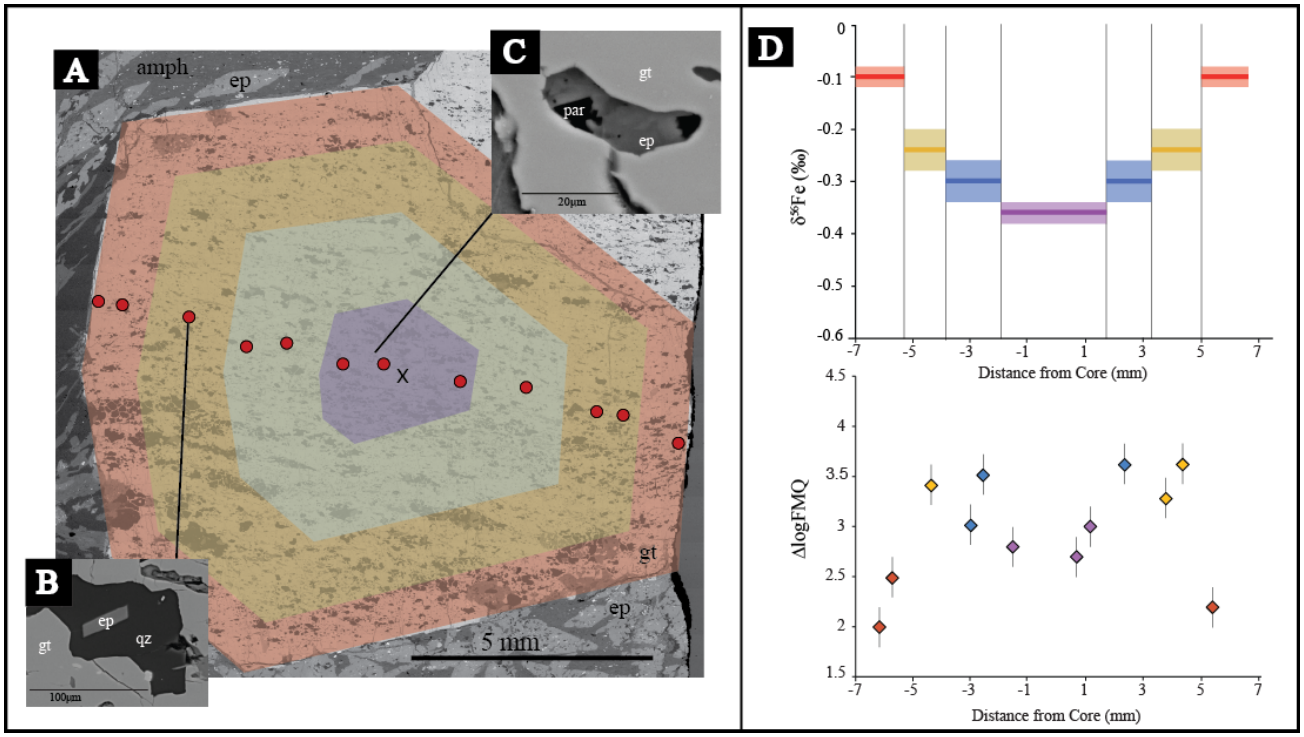

Figure 1.1 – A) BSE image of the garnet grain in sample 09DSF-23E. Epidote inclusions used in oxybarometry calculations are shown as red circles and sampling zones used for iron isotope measurements indicated by colored regions. B) Example of an epidote inclusion used in oxybarometry calculations. C) Example of a lawsonite pseudomorph that was avoided in oxybarometry calculations. D) δ^{56}Fe (top) and ΔlogFMQ (bottom) values for sample 09DSF-23E plotted from garnet rim to rim. δ^{56}Fe values were analyzed once for each garnet zone and have been plotted symmetrically to show trend from garnet rim to rim. Error calculations for the δ^{56}Fe data are the two-standard deviation of four isotopic analysis for each sample. All error for ΔlogFMQ are ±0.2 log units based on ±1kbar and ±40°C error associated with *P*-*T* estimates from thermodynamic modeling (Palin et al., 2016).

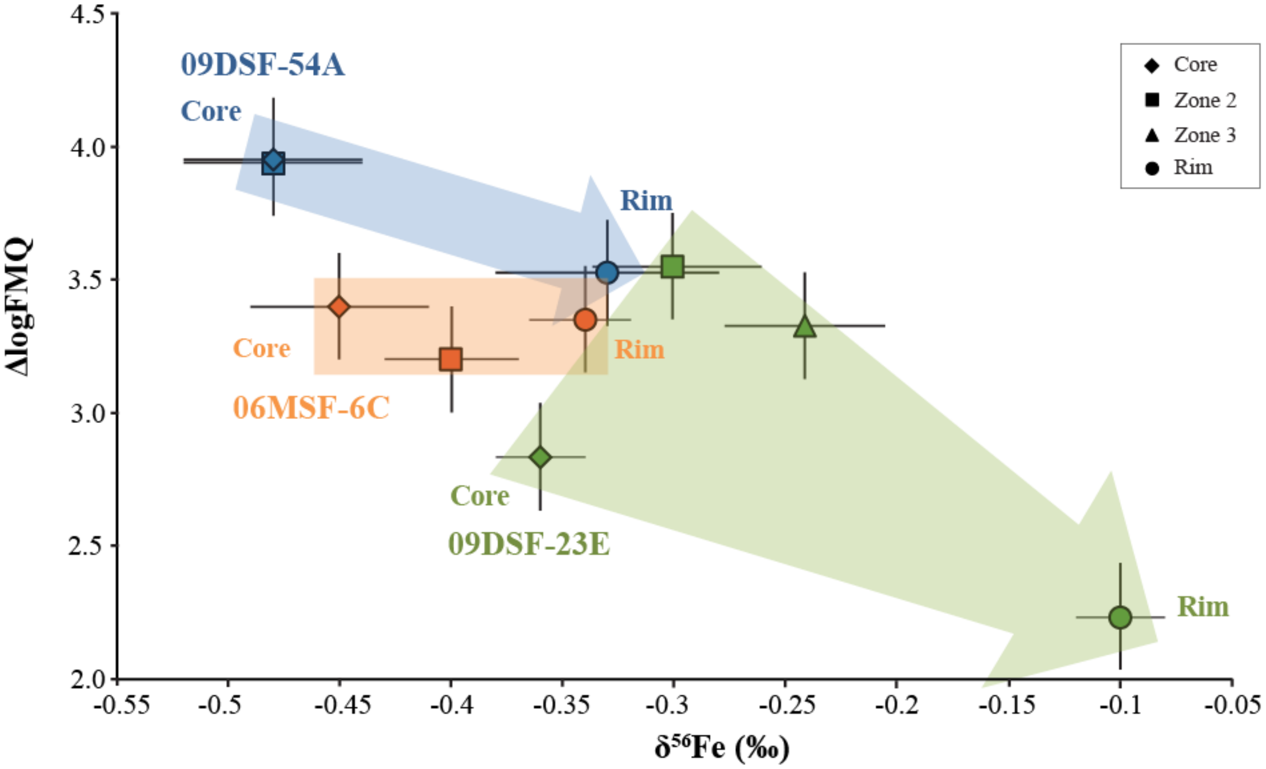

Figure 1.2–Iron isotope data, presented as δ^{56}Fe values, plotted against the ΔlogFMQ values for each zone (average of core points, average of points in each middle zone, average of rim points). 09DSF-54A is plotted in blue, 09DSF-23E in green, and 06MSF-6C in orange. Each fO_2 data point represents a composite of all epidote inclusion-garnet pairs in that zone for the garnet. The arrows show the general trends in the data from the core (diamond markers) to middle zones (square markers) to garnet rims (circle markers). Error calculations for the δ^{56}Fe data are the two-standard deviation of four isotopic analysis for each sample. All error for ΔlogFMQ are ±0.2 log units based on ±1kbar and ±40°C error associated with *P-T* estimates from thermodynamic modeling (Palin et al., 2016).

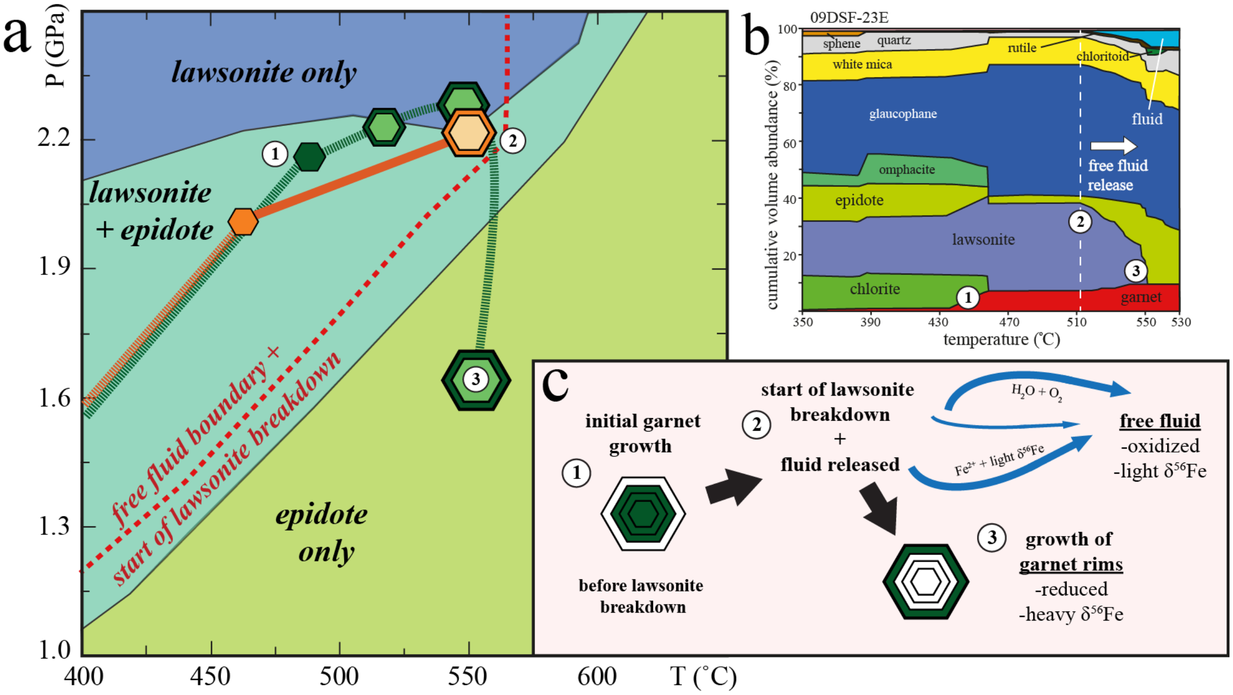

Figure 1.3 – **a)** Pressure-temperature (P-T) diagram showing *PT* path during garnet growth for samples 09DSF-23E (green) and 06MSF-6C (orange). *PT* path between garnet core and rim for sample 09DSF-23E is based on Sifnos *PT* paths by Dragovic et al., (2012), Dragovic et al., (2015) and Groppo et al., (2009). Condition of garnet growth for sample 09DSF-54A (not shown) is very similar to that for 09DSF-23E. Phases are labeled for fields showing PT conditions where epidote, lawsonite, and lawsonite + epidote are stable. **b)** Cumulative modal mineral volume abundance (%) for sample 09DSF-23E along the prograde and retrograde P-T path given in the inset of Figure 3a. The onset of lawsonite breakdown releases a free fluid phase, shown as the light blue field and marked by the white dashed line at ~515C. **c)** Cartoon showing conditions for sample 09DSF-23E at labeled points 1, 2, and 3 on the P-T and cumulative modal abundance diagrams (Fig. 3a and 3b).

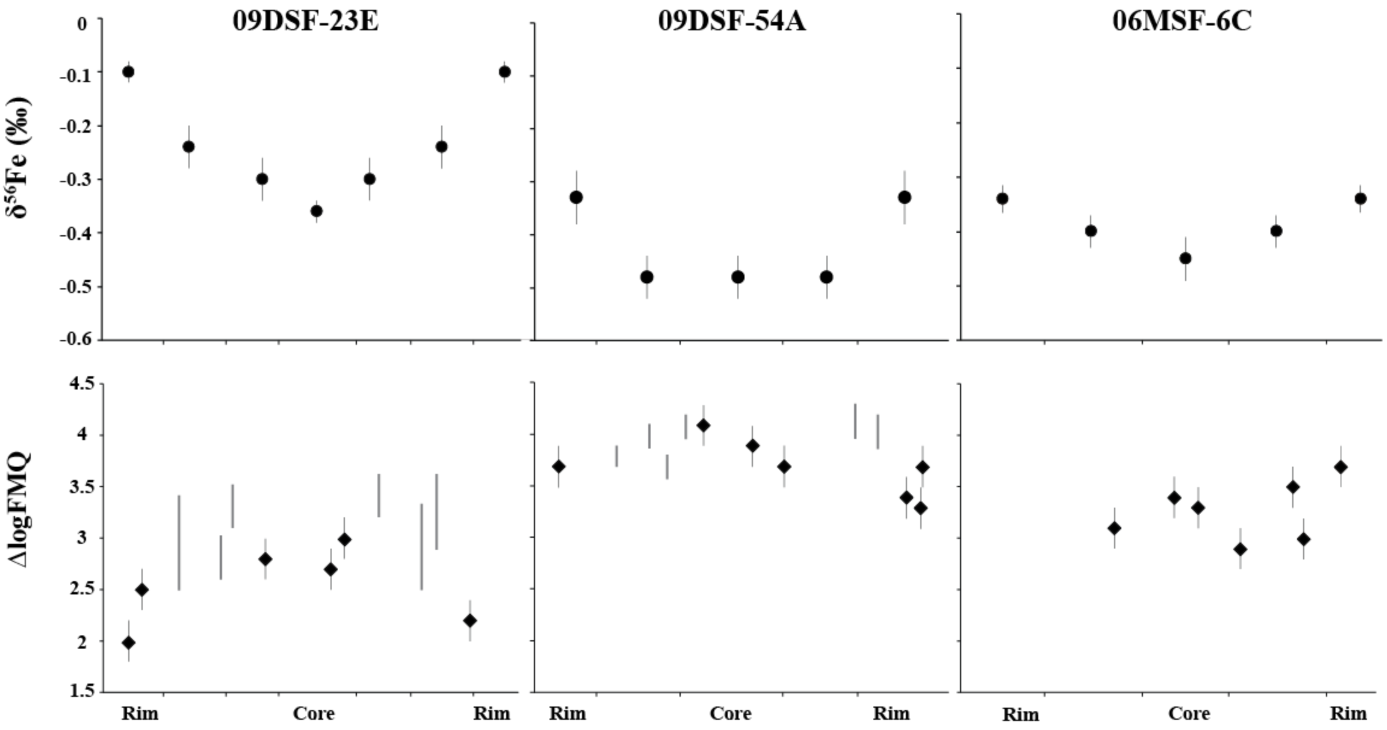

Figure 1.4: ΔlogFMQ and the δ^{56}Fe values plotted from rim to rim in one garnet grain from samples 09DSF-54A, 09DSF-23E, 06MSF-6C. Temperatures and pressures for garnet core and rim calculations are based on thermodynamic modeling (see Methods) and middle zones are plotted as lines to represent the range of fO_2 values possible for realistic *P*-*T* paths between garnet core and rim growth. Error calculations for the δ^{56}Fe data are the two-standard deviation of four isotopic analysis for each sample. All error for ΔlogFMQ are ±0.2 log units based on ±1kbar and ±40°C error associated with *P*-*T* estimates from thermodynamic modeling (Palin et al., 2016). This figure is Extended Data Figure 1 in the manuscript.

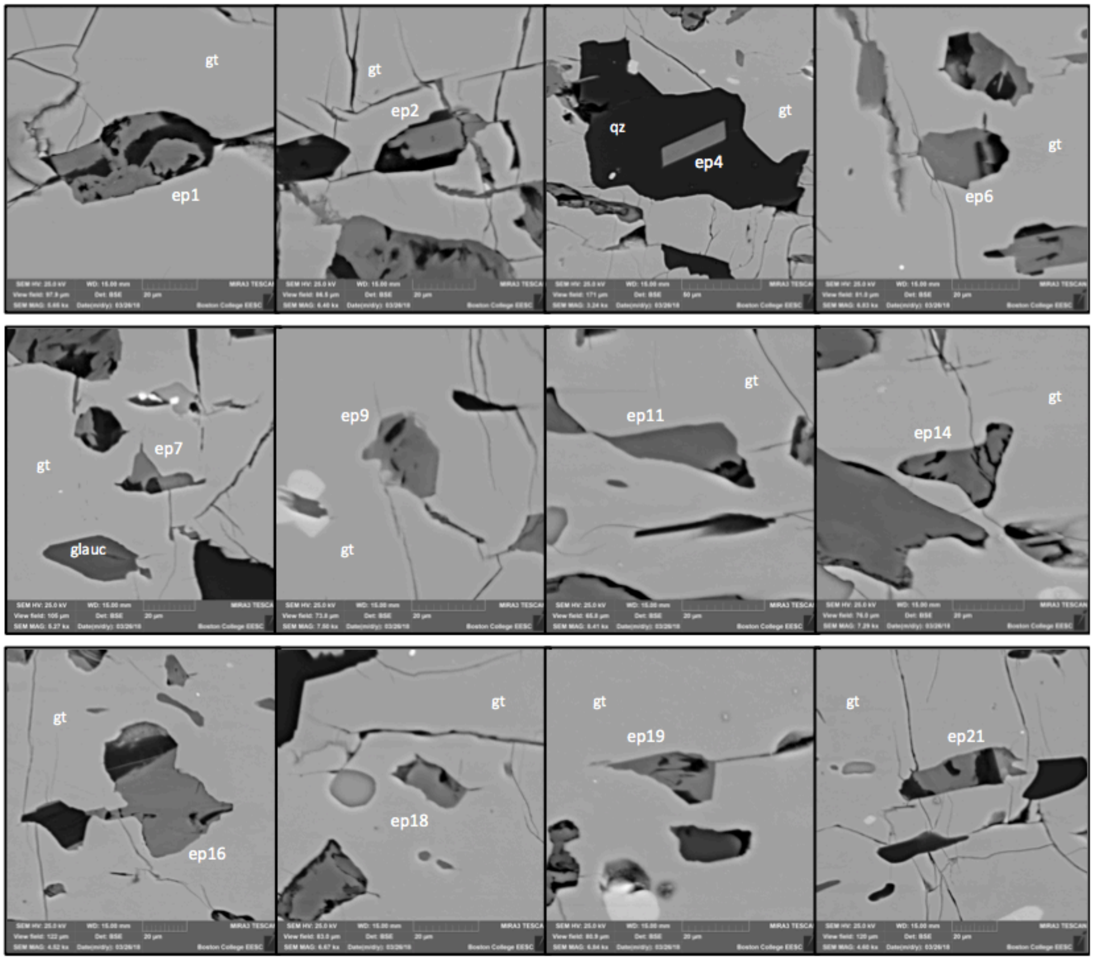

Figure 1.5: BSE images of each epidote inclusion in sample 09DSF-23E used in oxygen barometry calculations. This figure is Extended Data Figure 2 in the manuscript.

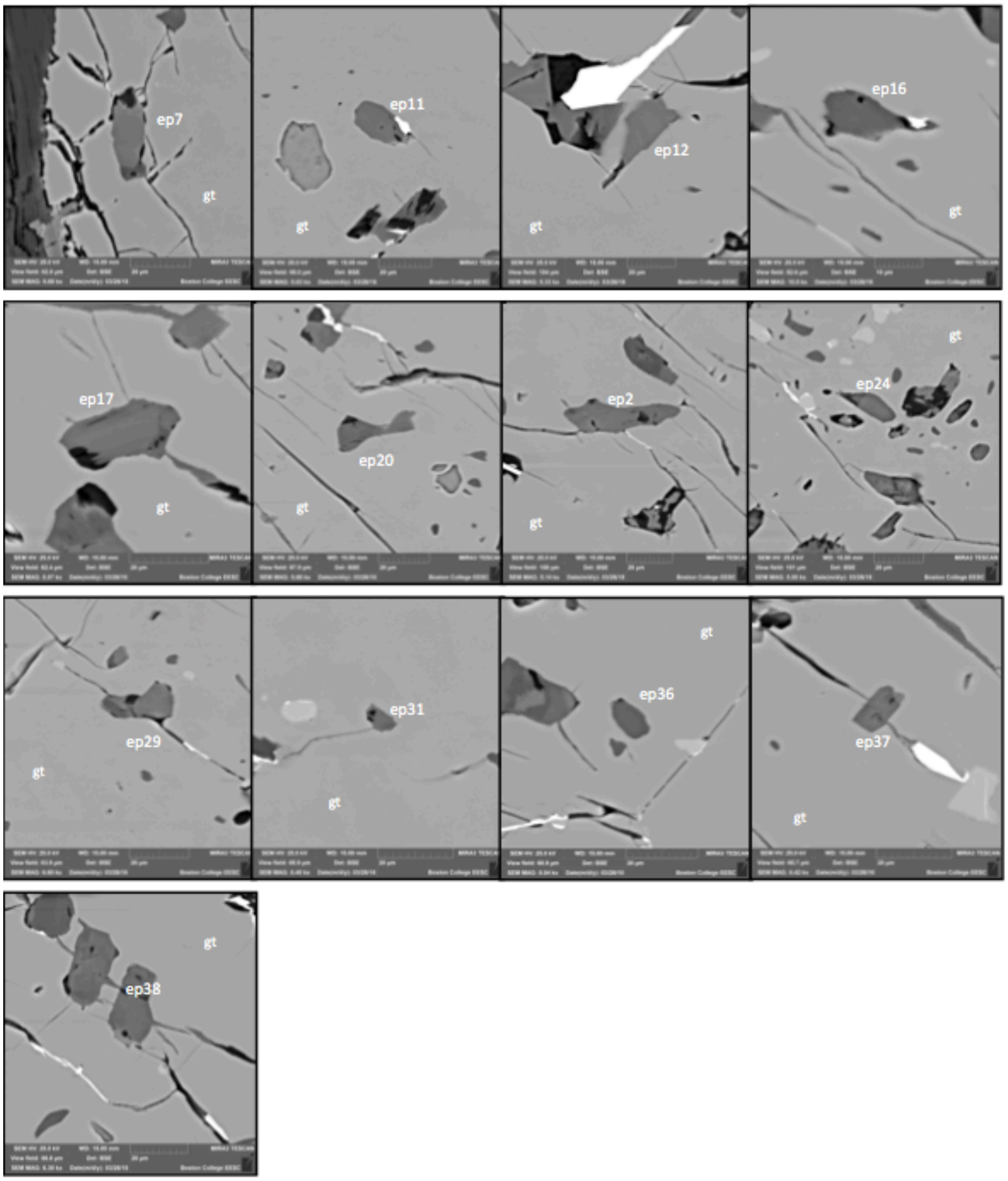

Figure 1.6: BSE images of each epidote inclusion in sample 09DSF-54A used in oxygen barometry calculations. This figure is Extended Data Figure 3 in the manuscript.

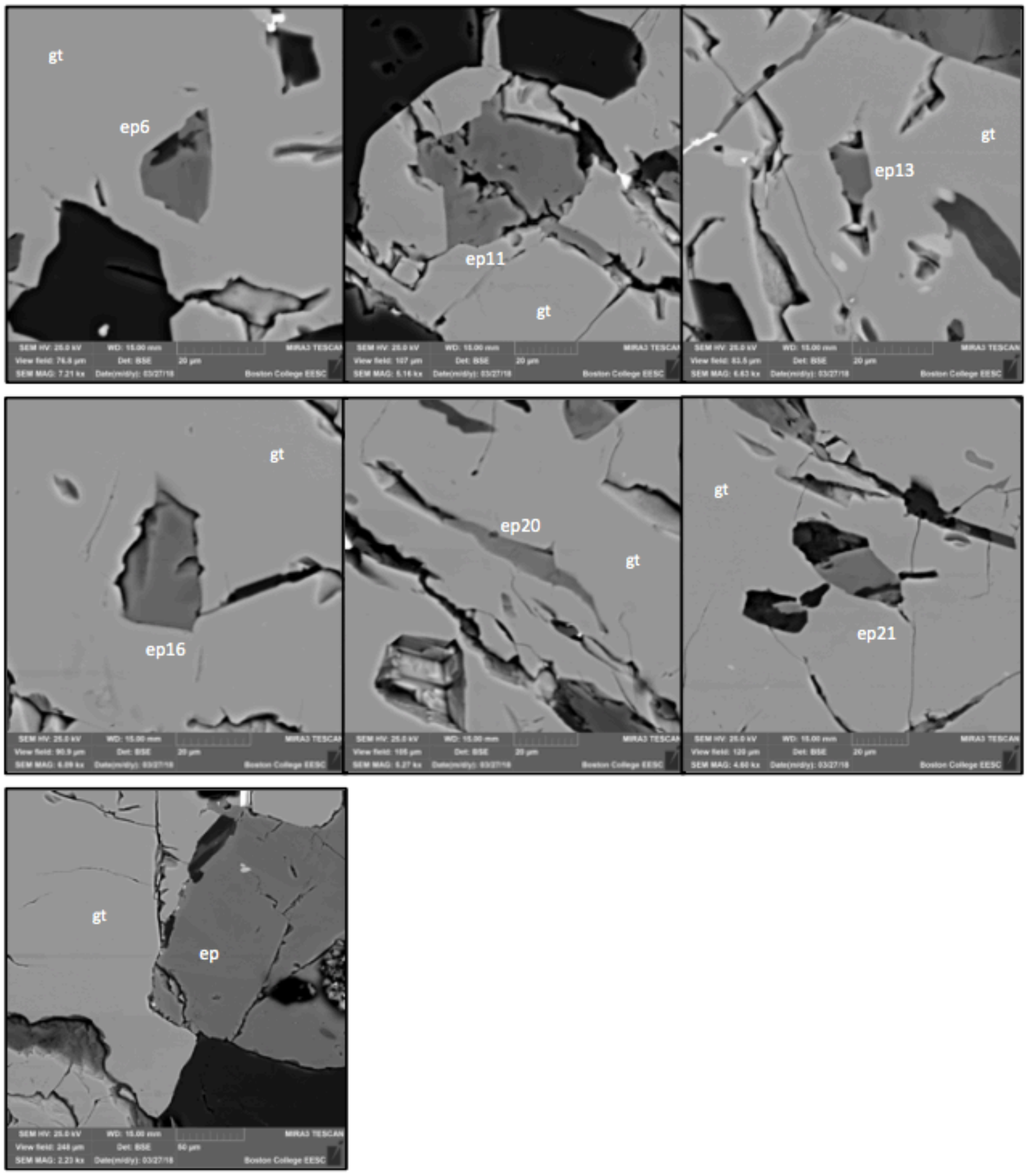

Figure 1.7: BSE images of each epidote inclusion in sample 06MSF-6C used in oxygen barometry calculations. This figure is Extended Data Figure 4 in the manuscript.

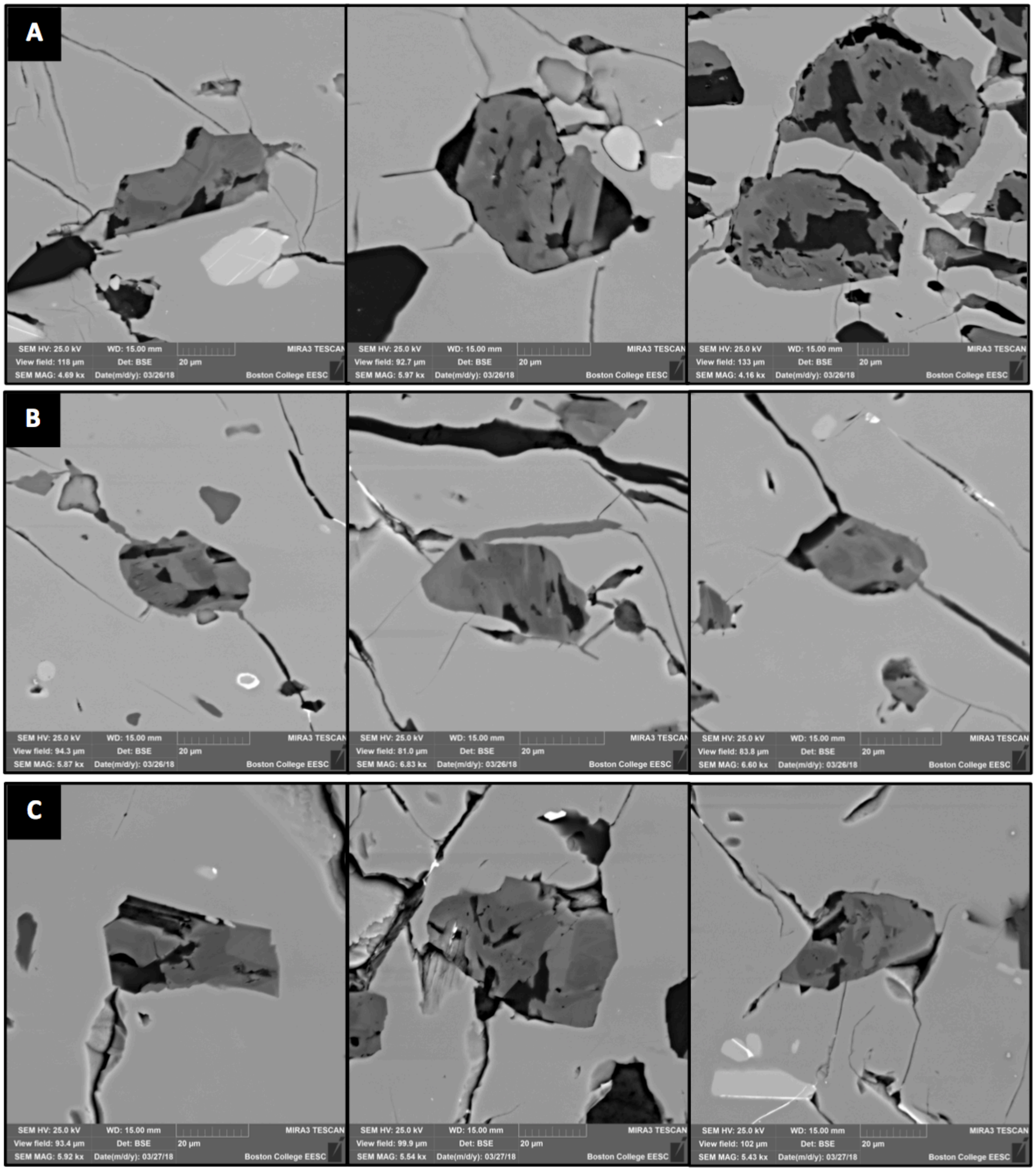

Figure 1.8: BSE images of epidote inclusion in samples A) 09DSF-23E, B) 09DSF-54A, and C) 06MSF-6C so show epidote inclusions thought to be pseudomorphs after lawsonite. Epidote inclusions like these examples show chemical zoning and are associated with albite or paragonite, products of lawsonite breakdown. These and all similar epidote inclusions were not used in oxygen barometry calculations. This figure is Extended Data Figure 5 in the manuscript.

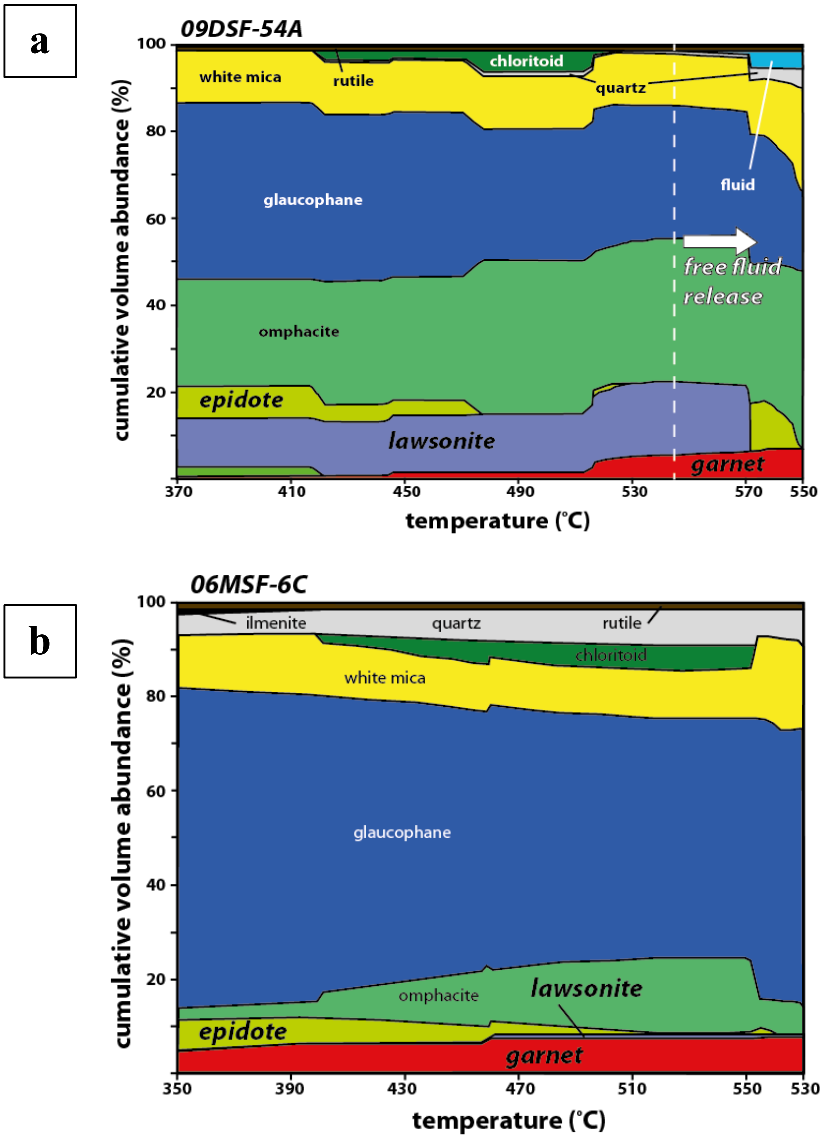

Figure 1.9: Modal mineral volume abundance (in %) for the P-T path given in Figure 3. a) Plot for sample 09DSF-54A shows garnet growth spans lawsonite breakdown. The onset of lawsonite breakdown releases a free fluid phase, shown as the light blue field and marked by the white dashed line at ~540C. b) Sample 06MSF-6C shows that garnet growth does not span the breakdown of any hydrous mineral phases. This figure is Extended Data Figure 6 in the manuscript.

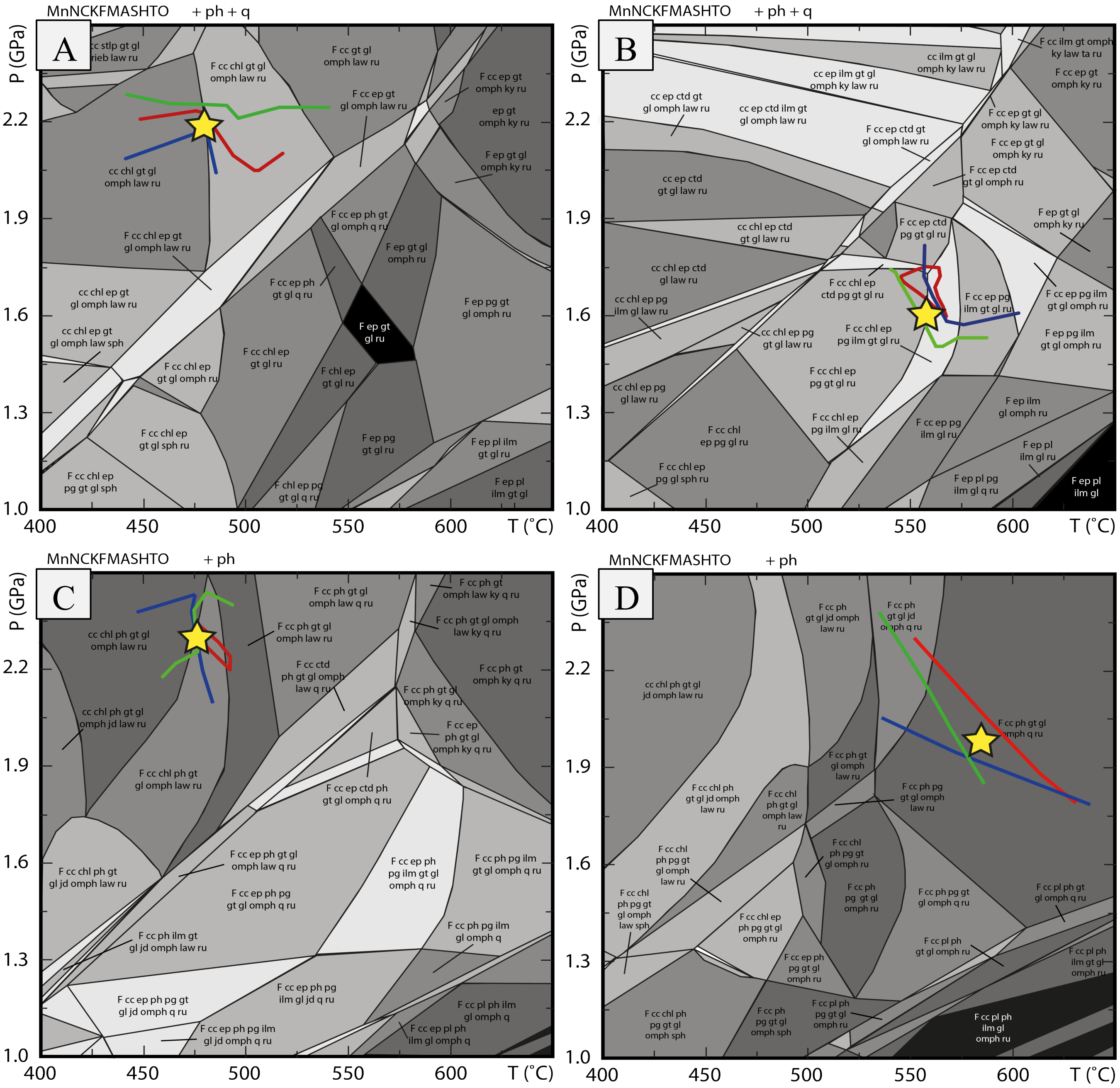

Figure 1.10: Equilibrium phase diagram sections used for calculation of core and rim P-T conditions for samples 09DSF-23E and 09DSF-54A. Phase diagrams (A) and (C) use whole rock bulk compositions for calculation of P-T conditions corresponding to core growth for samples 09DSF-23E and 09DSF-54A respectively. Phase diagrams (B) and (D) were calculated using matrix bulk compositions to estimate the P-T conditions for growth of the garnet rims (Extended Data Table 1.3) for samples 09DSF-23E and 09DSF-54A respectively. Garnet chemical isopleths corresponding to observed garnet core and rim chemistry (Supplementary Data) are plotted (almandine=red, grossular=green, spessartine=blue). Intersection of garnet core isopleths constrains the P–T of garnet nucleation and intersection of garnet rim isopleths constrains the P–T of garnet rim growth. Mineral assemblages are labeled using the following abbreviations: gt = garnet; ep = epidote; law = lawsonite; chl = chlorite; ph = phengite; omph = omphacite; q = quartz; ru = rutile; jd = jadeite; gl = glaucophane; ilm = ilmenite; pl = plagioclase; cc = calcite; F = fluid; sph = sphene; ctd = chloritoid; pg = paragonite; ky = kyanite. This figure is Extended Data Figure 7 in the manuscript.

1.5 REFERENCES

Agard, P., Goffé, B., Touret, J.L. and Vidal, O., 2000. Retrograde mineral and fluid evolution in high-pressure metapelites (Schistes lustrés unit, Western Alps). *Contributions to Mineralogy and Petrology*, *140*(3), pp.296-315.

Ague, J.J., Baxter, E.F. and Eckert Jr, J.O., 2001. High f O2 During Sillimanite Zone Metamorphism of Part of the Barrovian Type Locality, Glen Clova, Scotland. *Journal of Petrology*, *42*(7), pp.1301-1320.

Altherr, R., Schliestedt, M., Okrusch, M., Seidel, E., Kreuzer, H., Harre, W., Lenz, H., Wendt, I. and Wagner, G.A., 1979. Geochronology of high-pressure rocks on Sifnos (Cyclades, Greece). *Contributions to Mineralogy and Petrology*, *70*(3), pp.245-255.

Auzanneau, E., Schmidt, M.W., Vielzeuf, D. and Connolly, J.D., 2010. Titanium in phengite: a geobarometer for high temperature eclogites. *Contributions to Mineralogy and Petrology*, *159*(1), p.1.

Avigad, D., 1993. Tectonic juxtaposition of blueschists and greenschists in Sifnos Island (Aegean Sea)—implications for the structure of the Cycladic blueschist belt. *Journal of Structural Geology*, *15*(12), pp.1459-1469.

Avigad, D. and Garfunkel, Z., 1991. Uplift and exhumation of high-pressure metamorphic terrains: the example of the Cycladic blueschist belt (Aegean Sea). *Tectonophysics*, *188*(3), pp.357-372.

Barr, H., 1990. Preliminary fluid inclusion studies in a high-grade blueschist terrain, Syros, Greece. *Mineralogical Magazine*, *54*(375), pp.159-168.

Baxter, E.F. and Caddick, M.J., 2013. Garnet growth as a proxy for progressive subduction zone dehydration. *Geology*, *41*(6), pp.643-646.

Boundy, T.M., Donohue, C.L., Essene, E.J., Mezger, K. and Austrheim, H., 2002. Discovery of eclogite facies carbonate rocks from the Lindås Nappe, Caledonides, Western Norway. *Journal of Metamorphic Geology*, *20*(7), pp.649-667.

Breeding, C.M., Ague, J.J. and Bröcker, M., 2004. Fluid–metasedimentary rock interactions in subduction-zone mélange: implications for the chemical composition of arc magmas. *Geology*, *32*(12), pp.1041-1044.

Cao, Y., Song, S.G., Niu, Y.L., Jung, H. and Jin, Z.M., 2011. Variation of mineral composition, fabric and oxygen fugacity from massive to foliated eclogites during exhumation of subducted ocean crust in the North Qilian suture zone, NW China. *Journal of Metamorphic Geology*, *29*(7), pp.699-720.

Cheney, J.T., Brady, J.B., Harms, T.A. and Schumacher, J.C., 2001. Evolution of Cycladic Subduction Zone Rocks: Syros Blueschist-Eclogite Terrane III. In *Keck Symposium* (Vol. 14, pp. 107-112).

Christie, D.M., Carmichael, I.S. and Langmuir, C.H., 1986. Oxidation states of mid-ocean ridge basalt glasses. *Earth and Planetary Science Letters*, *79*(3-4), pp.397-411.

Coggon, R. and Holland, T.J.B., 2002. Mixing properties of phengitic micas and revised garnet-phengite thermobarometers. *Journal of Metamorphic Geology*, *20*(7), pp.683-696.

Connolly, J.A.D., 2009. The geodynamic equation of state: what and how. *Geochemistry, Geophysics, Geosystems*, *10*(10).

Dal Piaz, G., Cortiana, G., Del Moro, A., Martin, S., Pennacchioni, G. and Tartarotti, P., 2001. Tertiary age and paleostructural inferences of the eclogitic imprint in the Austroalpine outliers and Zermatt–Saas ophiolite, western Alps. *International Journal of Earth Sciences*, *90*(3), pp.668-684.

Dauphas, N., John, S.G. and Rouxel, O., 2017. Iron isotope systematics. *Reviews in Mineralogy and Geochemistry*, *82*(1), pp.415-510.

Dauphas, N., et al., 2004. Chromatographic separation and multicollection-ICPMS analysis of iron. Investigating mass-dependent and-independent isotope effects. *Analytical Chem.* 76, 5855-5863.

Debret, B., Millet, M.A., Pons, M.L., Bouilhol, P., Inglis, E. and Williams, H., 2016. Isotopic evidence for iron mobility during subduction. *Geology*, *44*(3), pp.215-218.

Debret, B. & Sverjensky, D.A. 2017. Highly oxidizing fluids generated during serpentine breakdown in subduction zones. *Sci. Rep.* 7, 10351.

Diener, J.F.A. and Powell, R., 2012. Revised activity–composition models for clinopyroxene and amphibole. *Journal of Metamorphic Geology*, *30*(2), pp.131-142.

Donohue, C.L. and Essene, E.J., 2000. An oxygen barometer with the assemblage garnet–epidote. *Earth and Planetary Science Letters*, *181*(3), pp.459-472.

Dragovic, B., 2013. *Constraining the rates and timescales of garnet growth and associated dehydration during metamorphism* (Doctoral dissertation, Boston University).

Dragovic, B., Baxter, E.F. and Caddick, M.J., 2015. Pulsed dehydration and garnet growth during subduction revealed by zoned garnet geochronology and thermodynamic modeling, Sifnos, Greece. *Earth and Planetary Science Letters*, *413*, pp.111-122.

Dragovic, B., Samanta, L.M., Baxter, E.F., Selverstone, J., 2012. Using garnet to constrain the duration and rate of water-releasing metamorphic reactions during subduction: an example from Sifnos, Greece. Chem. Geol. 314–317, 9–22.

Evans, K.A., 2012. The redox budget of subduction zones. *Earth-Science Reviews*, *113*(1-2), pp.11-32.

Evans, K.A., Elburg, M.A. and Kamenetsky, V.S., 2012. Oxidation state of subarc mantle. *Geology*, *40*(9), pp.783-786.

Forster, M., Lister, G., Compagnoni, R., Giles, D., Hills, Q., Betts, P., Beltrando, M. and Tamagno, E., 2004. Mapping of oceanic crust with" HP" to" UHP" metamorphism: The Lago di Cignana Unit,(Western Alps). In *Mapping geology in Italy*. Geological Society of London.

Froitzheim, N., Schmid, S.M. and Frey, M., 1996. Mesozoic paleogeography and the timing of eclogite-facies metamorphism in the Alps: a working hypothesis. *Eclogae Geologicae Helvetiae*, *89*(1), p.81.

Frost, B.R., 1991. Introduction to oxygen fugacity and its petrologic importance. *Reviews in Mineralogy and Geochemistry*, *25*(1), pp.1-9.

Furman, M.L., 1988. Ternary-feldspar modeling and thermometry. *Amer. Mineral.*, *73*, pp.201-215.

Groppo, C., & Castelli, D., 2010. Prograde P–T evolution of a lawsonite eclogite from the Monviso meta-ophiolite (Western Alps): dehydration and redox reactions during subduction of oceanic FeTi-oxide gabbro. *Journal of Petrology*, *51*(12), 2489-2514.

Groppo, C., Forster, M., Lister, G. and Compagnoni, R., 2009. Glaucophane schists and associated rocks from Sifnos (Cyclades, Greece): New constraints on the P–T evolution from oxidized systems. *Lithos*, *109*(3-4), pp.254-273.

Hibbert, K.E.J., Williams, H.M., Kerr, A.C. and Puchtel, I.S., 2012. Iron isotopes in ancient and modern komatiites: evidence in support of an oxidised mantle from Archean to present. *Earth Planet. Sci. Lett.* **321**, 198-207.

Holland, T.J.B. and Powell, R., 1998. An internally consistent thermodynamic data set for phases of petrological interest. *Journal of metamorphic Geology*, *16*(3), pp.309-343.

Inglis, E.C., Debret, B., Burton, K.W., Millet, M.A., Pons, M.L., Dale, C.W., Bouilhol, P., Cooper, M., Nowell, G.M., McCoy-West, A.J. and Williams, H.M., 2017. The behavior of iron and zinc stable isotopes accompanying the subduction of mafic oceanic crust: A case study from Western Alpine ophiolites. *Geochemistry, geophysics, geosystems*, *18*(7), pp.2562-2579.

Kelley, K.A. and Cottrell, E., 2009. Water and the oxidation state of subduction zone magmas. *Science*, *325*(5940), pp.605-607.

Keiter, M., Ballhaus, C. and Tomaschek, F., 2011. A new geological map of the Island of Syros (Aegean Sea, Greece): implications for lithostratigraphy and structural history of the Cycladic Blueschist Unit. *Geological Society of America Special Papers*, *481*, pp.1-43.

Lapen, T.J., Johnson, C.M., Baumgartner, L.P., Mahlen, N.J., Beard, B.L. and Amato, J.M., 2003. Burial rates during prograde metamorphism of an ultra-high-pressure terrane: an example from Lago di Cignana, western Alps, Italy. *Earth and Planetary Science Letters*, *215*(1-2), pp.57-72.

Lee, C.T.A., Luffi, P., Le Roux, V., Dasgupta, R., Albaréde, F. and Leeman, W.P., 2010. The redox state of arc mantle using Zn/Fe systematics. *Nature*, *468*(7324), p.681.

Lister, G.S. and Forster, M.A., 2016. White mica 40Ar/39Ar age spectra and the timing of multiple episodes of high-P metamorphic mineral growth in the Cycladic eclogite–blueschist belt, Syros, Aegean Sea, Greece. *Journal of Metamorphic Geology*, *34*(5), pp.401-421.

Magni, V., Bouilhol, P. and van Hunen, J., 2014. Deep water recycling through time. *Geochemistry, Geophysics, Geosystems*, *15*(11), pp.4203-4216.

Marschall, H.R. and Schumacher, J.C., 2012. Arc magmas sourced from mélange diapirs in subduction zones. *Nature Geoscience*, *5*(12), pp.862-867.

Mattinson, C.G., Zhang, R.Y., Tsujimori, T. and Liou, J.G., 2004. Epidote-rich talc-kyanite-phengite eclogites, Sulu terrane, eastern China: P-T-fO_2estimates and the significance of the epidote-talc assemblage in eclogite. *American Mineralogist*, *89*(11-12), pp.1772-1783.

Matthews, A. and Schliestedt, M., 1984. Evolution of the blueschist and greenschist facies rocks of Sifnos, Cyclades, Greece. *Contributions to Mineralogy and Petrology*, *88*(1), pp.150-163.

Millet, M.A., Baker, J.A. and Payne, C.E., 2012. Ultra-precise stable Fe isotope measurements by high resolution multiple-collector inductively coupled plasma mass spectrometry with a 57Fe–58Fe double spike. *Chem. Geol.* **304**, 18-25.

Ming, T., Erdman, M., Eldridge, G., Lee, C.T.A., 2018. The redox "filter" beneath magmatic orogens and the formation of continental crust. *Science Advances, 4*, 5.

Marmo, B.A., Clarke, G.L. and Powell, R., 2002. Fractionation of bulk rock composition due to porphyroblast growth: effects on eclogite facies mineral equilibria, Pam Peninsula, New Caledonia. *Journal of metamorphic Geology*, *20*(1), pp.151-165.

Okazaki, K. and Hirth, G., 2016. Dehydration of lawsonite could directly trigger earthquakes in subducting oceanic crust. *Nature*, *530*(7588), p.81.

Okrusch, M. and Bröcker, M., 1990. Eclogites associated with high-grade blueschists in the Cyclades archipelago, Greece: a review. *European Journal of Mineralogy*, pp.451-478.

Palin, R.M., Weller, O.M., Waters, D.J. and Dyck, B., 2016. Quantifying geological uncertainty in metamorphic phase equilibria modelling; a Monte Carlo assessment and implications for tectonic interpretations. *Geoscience Frontiers*, *7*(4), pp.591-607.

Parkinson, I.J. and Arculus, R.J., 1999. The redox state of subduction zones: insights from arc-peridotites. *Chemical Geology*, *160*(4), pp.409-423.

Poli, S. and Schmidt, M.W., 1995. H2O transport and release in subduction zones: experimental constraints on basaltic and andesitic systems. *Journal of Geophysical Research: Solid Earth*, *100*(B11), pp.22299-22314.

Pollington, A.D., Baxter, E.F., 2011. High precision microsampling and preparation of zoned garnet porphyroblasts for Sm–Nd geochronology. Chem. Geol. 281, 270–282.

Polyakov, V.B. and Mineev, S.D., 2000. The use of Mössbauer spectroscopy in stable isotope geochemistry. *Geochimica et Cosmochimica Acta*, *64*(5), pp.849-865.

Powell, R. and Holland, T.J.B., 1988. An internally consistent dataset with uncertainties and correlations: 3. Applications to geobarometry, worked examples and a computer program. *Journal of metamorphic Geology*, *6*(2), pp.173-204.

Powell, R. and Holland, T., 1994. Optimal geothermometry and geobarometry. *American Mineralogist*, *79*(1-2), pp.120-133.

Powell, R., Holland, T.J.B.H. and Worley, B., 1998. Calculating phase diagrams involving solid solutions via non-linear equations, with examples using THERMOCALC. *Journal of metamorphic Geology*, *16*(4), pp.577-588.

Reinecke, T., 1998. Prograde high-to ultrahigh-pressure metamorphism and exhumation of oceanic sediments at Lago di Cignana, Zermatt-Saas Zone, western Alps. *Lithos*, *42*(3-4), pp.147-189.

Reinecke, T., 1991. Very-high-pressure metamorphism and uplift of coesite-bearing metasediments from the Zermatt-Saas zone, Western Alps. *European Journal of Mineralogy*, pp.7-18.

Schmidt, M.W. and Poli, S., 1998. Experimentally based water budgets for dehydrating slabs and consequences for arc magma generation. *Earth and Planetary Science Letters*, *163*(1), pp.361-379.

Schauble, E.A., Rossman, G.R. and Taylor, H.P., 2001. Theoretical estimates of equilibrium Fe-isotope fractionations from vibrational spectroscopy. *Geochimica et Cosmochimica Acta*, *65*(15), pp.2487-2497.

Schmädicke, E. and Will, T.M., 2003. Pressure–temperature evolution of blueschist facies rocks from Sifnos, Greece, and implications for the exhumation of high-pressure rocks in the Central Aegean. *Journal of Metamorphic Geology*, *21*(8), pp.799-811.

Skora, S., Lapen, T.J., Baumgartner, L.P., Johnson, C.M., Hellebrand, E. and Mahlen, N.J., 2009. The duration of prograde garnet crystallization in the UHP eclogites at Lago di Cignana, Italy. *Earth and Planetary Science Letters*, *287*(3), pp.402-411.

Sossi, P.A., Halverson, G.P., Nebel, O. and Eggins, S.M., 2015. Combined separation of Cu, Fe and Zn from rock matrices and improved analytical protocols for stable isotope determination. *Geostandards and Geoanalytical Research*, **39**, 129-149.

Tatsumi, Y., 1986. Formation of the volcanic front in subduction zones. *Geophysical Research Letters*, *13*(8), pp.717-720.

Trotet, F., Jolivet, L. and Vidal, O., 2001. Tectono-metamorphic evolution of Syros and Sifnos islands (Cyclades, Greece). *Tectonophysics*, *338*(2), pp.179-206.

Van der Klauw, S.N.G.C., Reinecke, T. and Stöckhert, B., 1997. Exhumation of ultrahigh-pressure metamorphic oceanic crust from Lago di Cignana, Piemontese zone, western Alps: the structural record in metabasites. *Lithos*, *41*(1-3), pp.79-102.

Weyer, S. and Schwieters, J.B., 2003. High precision Fe isotope measurements with high mass resolution MC-ICPMS. *International Journal of Mass Spectrometry*, **226**, 355-368.

White, R.W., Powell, R. and Holland, T.J.B., 2007. Progress relating to calculation of partial melting equilibria for metapelites. *Journal of metamorphic Geology*, *25*(5), pp.511-527.

White, R.W., Powell, R. and Clarke, G.L., 2002. The interpretation of reaction textures in Fe-rich metapelitic granulites of the Musgrave Block, central Australia: constraints from mineral equilibria calculations in the system K2O–FeO–MgO–Al2O3–SiO2–H2O–TiO2–Fe2O3. *Journal of metamorphic Geology*, *20*(1), pp.41-55.

White, R.W., Powell, R., Holland, T.J.B. and Worley, B.A., 2000. The effect of TiO~ 2 and Fe~ 2O~ 3 on metapelitic assemblages at greenschist and amphibolite facies conditions: mineral equilibria calculations in the system K~ 2O-FeO-MgO-Al~ 2O~ 3-SiO~ 2-H~ 2O-TiO~ 2-Fe~ 2O~ 3. *Journal of Metamorphic Geology*, *18*(5), pp.497-512.

Wijbrans, J.R., Schliestedt, M. and York, D., 1990. Single grain argon laser probe dating of phengites from the blueschist to greenschist transition on Sifnos (Cyclades, Greece). *Contributions to Mineralogy and Petrology*, *104*(5), pp.582-593.

2.0 CHAPTER 2

2.1 METHODS

All samples described above were characterized by means of electron microscopy analytical methods using a Mira scanning electron microscope at Boston College. Backscattered electron (BSE) images of full thin sections, or sub regions thereof, were produced to characterize phase relationships. Semi-quantitative characterization of materials was conducted by means of energy dispersive spectrometry (EDS) analyzed at Boston College using an Oxford Instruments X-Max 50 Silicon Drift Detector, from which maps of chemical zonation could be produced to guide subsequent quantitate electron microprobe analysis.

Quantitative compositional analysis was performed for samples 09DSF-23E, 09DSF-54A, 06MSF-6C, 14BSY-35C, 09DSF-37A using wavelength dispersive spectrometry (WDS) on a JEOL JXA-8200 electron microprobe at the Massachusetts Institute of Technology. All spot analyses were carried out using an acceleration voltage of 15kv, a current of 20nA, and approximate spot size of 5µm. In addition to samples 09DSF-23E, 09DSF-54A, and 06MSF-6C presented in Chapter 1, oxygen fugacity calculations were carried out on samples 14BSY-35C and 09DSF-37A. Compositional data obtained from the electron microprobe for sample 14BSY-35C (Table 2.2) and sample 09DSF-37A (Table 2.3 and 2.4) were used to calculate garnet and epidote activities for each epidote inclusion and surrounding garnet pair (14BSY-35C: Table 2.5 & 09DSF-37A: Table 2.6 and 2.7) for use in fO_2 calculations. Oxygen fugacity calculations for samples 09DSF-37A and 14BSY-35C and iron isotope preparation and analysis for sample 14BSY-35C follow the procedure presented in Chapter 1.

2.1.1 Partial Dissolution Fractionation Tests

Tests were conducted to explore potential iron isotope fractionation during the partial dissolution process. Pure gem quality garnets with no visible inclusions from Mason Mountain Mine, North Carolina were crushed together and portioned into seven portions of equal mass. The seven portions were then subjected to the various partial dissolution procedures described below.

- **Procedure K:** Garnet sample experienced no partial dissolution to compare with test samples for potential iron isotope fractionation. Partial dissolution test yields garnet reside (Gt K) for analysis.

- **Procedure G:** Garnet sample partially dissolved in nitric acid only to test if nitric acid alone will fractionate iron isotope compositions. Partial dissolution test yields garnet reside (Gt G) and nitric acid leachate (Gt G HNO_3) for analysis.

  Procedure:
  1. 3hrs in 7N nitric acid
  2. Collect leach and rinses

- **Procedure H:** Garnet sample partially dissolved in HF acid only to test if HF acid alone will fractionate iron isotope compositions. Partial dissolution test yields garnet reside (Gt H) and HF acid leachate (Gt H HF) for analysis.

  Procedure:
  1. 30 mins in HF acid (1mL concentrated HF; 1mL H_2O)
  2. Collect leach and rinses

- **Procedure F:** Garnet sample partially dissolved using the normal Baxter Group partial dissolution routine described below. Partial dissolution test yields garnet reside (Gt F) for analysis.

  Procedure:
  1. 30 mins in HF acid (1mL concentrated HF; 1mL 1.5N HCl)
  2. Overnight in perchloric acid
  3. 3 hours in 7N nitric acid
  4. 50 mins in aqua reqia
  5. Rinses between steps in 1.5N HCl and H_2O

- **Procedure J:** Garnet sample partially dissolved using the 2 stage Nitric-HF dissolution procedure described below. The first three steps of this test should remove any inclusions. Any difference between the garnet residue and leachate in step 4 would represent Fe leaching and fractionation purely from garnet. Partial dissolution test yields garnet reside (Gt J) and nitric acid leachate (Gt J HNO_3) collected from the forth step for analysis.

  Procedure:
  1. 2hrs in 7N nitric
  2. 2hrs in weak HF (80µL HF + 1mL of H_2O)
  3. 2hrs in 7N nitric to remove fluorides
  4. 2hrs in 7N nitric – collect leach and rinses
  5. Rinses between steps in H_2O only

- **Procedure I:** Garnet sample partially dissolved using the 2 stage Nitric-HF dissolution procedure described below. The first three steps of this test should remove any inclusions. Any difference between the garnet residue and leachate in step 4 would represent Fe leaching and fractionation purely from garnet. Partial dissolution test yields garnet reside (Gt I) and HF acid leachate (Gt I HF) collected from the forth step for analysis.

  Procedure:
  1. 2hrs in 7N nitric
  2. 2hrs in weak HF (80µL HF + 1mL of H_2O)
  3. 2hrs in 7N nitric to remove fluorides
  4. 2hrs in weak HF (80µL HF + 1mL of H_2O)-collect leach + rinses from this step only
  5. Rinses between steps in H_2O only

- **Procedure D:** Garnet sample partially dissolved using the 2 stage Nitric-HF dissolution procedure described below. Partial dissolution test yields garnet reside (Gt D) and nitric + HF acid leachate (Gt D HF+ HNO_3) collected from the forth and fifth steps for analysis.

  Procedure:
  1. 2hrs in 7N nitric
  2. 2hrs in weak HF (80µL HF + 1mL of H_2O)
  3. 2hrs in 7N nitric to remove fluorides
  4. 30 mins in weak HF (80µL HF + 1mL of H_2O)
  5. 2hrs in 7N nitric
  6. Collect combined HF + nitric leach (steps 4 and 5 only)
  7. Rinses between steps in H_2O only

Sample crushing and the partial and full dissolution processes described above were completed in the clean lab at Boston College. Iron was chemically separated using anionic exchange resin, following the method of Williams et al. (2004) and Williams et al. (2009), in preparation for MC-ICPMS analysis. Column chemistry was completed in the

Durham University clean lab and iron isotope compositions were analyzed using the Thermo Scientific Neptune Plus MC-ICPMS at Durham University.

2.2 RESULTS

SEM BSE imaging analysis and petrographic observations of epidote inclusions in garnet porphyroblasts in samples, 09DSF-23E, 09DSF-54A, 06MSF-6C, 14BSY-35C, and 09DSF-37A reveal two distinct populations of epidote inclusions. In samples 09DSF-23E, 09DSF-54A, 06MSF-6C, and 09DSF-37A epidote inclusions either show little to no compositional zoning and are not associated with products of the breakdown of lawsonite, such as albite or paragonite, or show vast compositional zoning and are present with products of the breakdown of lawsonite, such as albite or paragonite. The presence of these two populations of epidote inclusions suggests that some epidote inclusions in garnet are primary epidote and some epidote inclusions are pseudomorphs after lawsonite. Because of this and support from thermodynamic modeling claiming epidote and lawsonite are co-stable phases during garnet growth for samples 09DSF-23E, 09DSF-54A, 06MSF-6C (Chapter 1), these epidote inclusions are hypothesized to be primary epidote in equilibrium with the surrounding garnet and so were used for fO_2 calculations. BSE images of each epidote inclusions used in fO_2 calculations for samples 09DSF-23E, 09DSF-54A, 06MSF-6C are presented in Figures in Chapter 1.

Petrologic observations of sample 14BSY-35C show that all epidote inclusions in garnet cores are present as inclusions in quartz inclusions, show no compositional zoning, and have euhedral crystal shapes. Epidote inclusions in garnet rims are not associated with other mineral inclusions, show no compositional zoning, and exhibit an anhedral crystal shape. Additionally, sample 14BSY-35C lacks any obvious pseudomorphs after lawsonite either as inclusions in garnet or in the matrix. BSE images of each epidote inclusions used in fO_2 calculations for sample 14BSY-35C are presented in Figure 2.8. Samples G17-S825A02 and G17-S825A03 from Lago di Cignana show only zoned epidote inclusions in garnet porphyroblasts so fO_2 calculations with these samples using garnet-epidote oxybarometry was not attempted.

Oxygen fugacity and iron isotope results for sample 14BSY-35C are presented in Figure 2.10 as plots of fO_2 (ΔlogFMQ) and iron isotope compositions (δ^{56}Fe) plotted rim to rim in one garnet grain. Data contained in the iron isotope composition plot is reported in Table 2.9 and data contained in the fO_2 plot is reported in Table 2.11. A complete record of each iron isotope compositional measurement is reported in Table 2.8. Calculated oxygen fugacities for sample 14BSY-35C range from 3.1 to 3.4 ΔlogFMQ for garnet cores and 2.5 to 2.7 ΔlogFMQ for garnet rims. Iron isotope compositions (δ^{56}Fe) change from -0.12‰ to -0.047‰ from garnet cores to rims.

Calculated fO_2 data for sample 09DSF-37A contained in the Figure 2.11 is reported in Table 2.10. Oxygen fugacity results for sample 09DSF-37A are presented in Figure 2.11 from garnet rim to rim and core to rim at a constant fO_2 of -18 logfO_2 and show no systematic change from garnet rim to rims. Because of the lack of systematic redox change from garnet rim to rim and lack of large garnet porphyroblasts for zoned work (garnets measure <3mm), iron isotope compositional analysis was not attempted for sample 09DSF-37A. Results for samples 09DSF-23E, 09DSF-54A, and 06MSF-6C including electron microprobe compositional data, BSE pictures of each epidote inclusion, oxygen fugacity calculations, and iron isotope compositions are reported in Chapter 1.

Partial dissolution fractionation test results conduced to ensure no iron isotope fractionation would result from the partial dissolution procedure are reported in Table 2.9. Results yield δ^{56}Fe compositions that are all within error between garnet with no partial dissolution, 0.015 ± 0.046, garnet partially dissolved in nitric acid, 0.085 ± 0.028, garnet dissolved in HF acid, 0.08 ± 0.05, and garnet subjected to the full nitric-HF multi-stage partial dissolution technique, 0.06 ± 0.033. HF leachates and garnet residue analyzed for samples Gt H and Gt I yield different δ^{56}Fe compositions and show there may be fractionation between the garnet residue and the HF leachate; this is because the residue likely includes secondary fluoride salts with fractionated δ^{56}Fe values from the dissolved Fe remaining in the HF leach solution. This underscores the well-known importance of following any HF-leach with a second strong acid treatment (i.e. perchloric or nitric acid) to break down and re-dissolve any secondary fluorides As no HF treated garnet is used for analysis without subsequent treatment with nitric or perchloric acid in the partial dissolution methods utilized in this study, these tests show that garnet samples put through the normal 2 stage partial dissolution processes show no iron isotope fractionation caused by the partial dissolution, allowing this study to use the HNO_3-HF multi-step partial dissolution to cleanse garnet of inclusions without fractionating iron isotope compositions.

2.3 DISCUSSION

2.3.1 fO_2 and Garnet-Epidote Oxybarometry

Garnet-epidote oxybarometry calculations yield more reduced garnet rims than cores for Sifnos samples 09DSF-23E and 09DSF-54A and Syros sample, 14BSY-35C. Sifnos samples 06MSF-6C and 09DSF-37A show no consistent change in fO_2 change from garnet core to rim. These data show that fO_2 is changing during garnet growth in samples 09DSF-23E, 09DSF-54A, and 14BSY-35C and is not for samples 06MSF-6C and 09DSF-37A.

Petrologic observations of sample 14BSY-35C reveals epidote inclusions are not compositional zoned and are never associated with products of the breakdown of lawsonite. Additionally, sample 14BSY-35C lacks any obvious pseudomorphs after lawsonite either as inclusions in garnet or in the matrix. These observations suggest that lawsonite was not a stable phase during garnet growth and thus, garnets in sample 14BSY-35C likely did not experience the dehydration and redox change associated with lawsonite breakdown like samples 09DSF-23E and 09DSF-54A. However, the large change in fO_2 values between garnet cores and rims implies that some process or reaction drove redox change during garnet growth in sample 14BSY-35C.

A number of possible explanations can be employed explain the variation in fO_2 from garnet core to rim in sample 14BSY-35C. It is possible that garnets in sample 14BSY-35C grew through the breakdown of a hydrous mineral, not lawsonite, that caused the release of water and oxygen to facilitate the change from more oxidized garnet cores to more reduced garnet rims. It is also possible that lawsonite was a stable phase and began to breakdown during garnet growth to cause a change in fO_2, like samples 09DSF-23E and 09DSF-54A, but no petrologic record of lawsonite stability was recorded in sample 14BSY-35C. Additionally, it is possible, although unlikely (Groppo and Castelli, 2010), that the breakdown and subsequent dehydration of hydrous mineral during subduction does not cause a change in redox state and the garnet core to rim fO_2 variations and caused by an unknown subduction process.

Pseudosection modeling of sample 14BSY-35C was attempted by Kendall (2016) but was unsuccessful in reproducing the observed mineral assemblage and prograde mineral assemblage evolution. Due to the mismatch between the observed mineral assemblage and model equilibria, information from thermodynamic modeling about dehydration reactions that occurred during garnet growth is limited. However, if garnet growth in sample 14BSY-35C occurred during a major dehydration reaction, as it did for samples 09DSF-23E and 09DSF-54A (Chapter 1), then the fO_2 results provide additional support for the hypothesis that the breakdown of hydrous minerals has a measurable effect on subduction fO_2.

Like sample 06MSF-6C, garnet-epidote oxybarometer calculations in sample 09DSF-37A, yield no symmetric pattern of redox change from garnet rim to rim (Figure 2.11). Because there is no symmetric pattern of redox change from garnet rim to rim, it is likely that garnets in sample 09DSF-37A did not grow through a major dehydration reaction, such as lawsonite breakdown. Petrologic observations of epidote inclusions in garnet porphyroblasts in Sifnos sample 09DSF-37A yields similar results to Sifnos samples 09DSF-23E, 09DSF-54A and 06MSF-6C and show two distinct populations of epidote inclusions. The presence of these two types of epidote inclusions suggests that some epidote inclusions in garnet are primary epidote and some epidote inclusions are pseudomorphs after lawsonite. These observations suggest that lawsonite and epidote were co-stable phases during garnet growth but give no evidence that lawsonite breakdown occurred during garnet growth. Alternatively, it is possible that garnets in sample 09DSF-37A grew through lawsonite breakdown but redox changes caused by the breakdown and dehydration were not recorded by the garnet-epidote inclusion equilibria.

Unlike samples 09DSF-23E, 09DSF-54A, 06MSF-6C and 14BSY-35C, extensive BSE imaging analysis was not conducted on every epidote inclusion used in fO_2 calculations to ensure no zoned epidotes were used for sample 09DSF-37A because it was decided early in the process that this sample was not an ideal candidate for study. Sample 09DSF-37A contains small garnet porphyroblasts (<3mm) and so is not ideal for iron isotope compositional analysis. Epidote inclusions were inspected at the time of compositional analysis at MIT but were not reexamined, like samples 09DSF-23E, 09DSF-54A, 06MSF-6C and 14BSY-35C, on the SEM at Boston College to ensure no compositional zoned inclusions were used. Because of this, it is also possible that epidote inclusions used in oxygen barometer calculations in sample 09DSF-37A are either not primary epidote but instead pseudomorphs after lawsonite or that either garnet or epidote compositions were altered after prograde growth and do not reflect the equilibrium conditions between garnet and epidote necessary for oxybarometer calculations. To full understand oxygen fugacity changes in sample 09DSF-37A, additional work would be necessary to ensure epidote inclusions used in calculations are not pseudomorphs after lawsonite and to discern if garnet growth spans a major dehydration reaction that may cause a change in redox conditions.

2.3.2 Challenges and Sources of Error in fO_2 Calculations

The largest source of error in the garnet-epidote oxybarometry calculations in this study arise from the difficulty in establishing whether epidote inclusions in garnet represent primary phases that are in chemical equilibrium with their host garnet during prograde metamorphism. Oxybarometry calculations require garnet and epidote to be in equilibrium for accurate fO_2 values to be calculated (Donohue and Essene, 2000). Both garnet and epidote often show chemical zonation and so, garnet-epidote barometer pairs must be studied using BSE imaging to ensure that pairs used in oxybarometer calculations are in equilibrium. Additionally, epidote is a common retrogressive phase in metabasalts and a number of samples from this study contain large retrogressive matrix epidote porphyroblasts. These retrogressive matrix epidotes are not in equilibrium with the entire garnet porphyroblasts so matrix epidote should not be used with garnet cores as oxybarometer pairs. In addition to primary epidote inclusions in garnet porphyroblasts, numerous epidote inclusions in garnet porphyroblasts in samples from this study are compositionally patchy and occur with paragonite or albite and likely reflect pseudomorphs after lawsonite. Compositionally patchy epidote inclusions were avoided in garnet-epidote oxybarometry calculations to prevent fO_2 miscalculations.

Additional error in garnet-epidote oxybarometry calculations include inaccurate pressure and temperature estimates. In oxybarometer calculations, the garnet-epidote reaction curve can shift ~0.05 log fO_2/kbar (Donohue and Essene, 2000) so accurate pressures for garnet growth are required for oxybarometer calculations. Using the small

2σ uncertainty of Palin et al. (2016) for thermodynamic pseudosection *PT* estimates of ±1 kbar and ±40°C, calculated oxygen fugacities encompassing this error show there is a ±0.2 ΔlogFMQ shift in the fO_2 results. Table 2.13 shows these values for three garnet-epidote inclusion pairs in sample 06MSF-6C. Based on the results of these sensitivity tests, an error of ±0.2 ΔlogFMQ is expected based on the *P-T* estimates used in the fO_2 calculations.

Additionally, Fe^{3+} substitution for Al in garnet can cause error in garnet-epidote oxybarometry calculations. Garnet-epidote oxybarometry calculations assume all iron in garnet is Fe^{2+} so these methods are only applicable to garnets with low Fe^{3+} content. However, the dependence of Fe^{3+} substitution in garnet of fO_2 calculations is minor: a 15 mol% Fe^{3+} substitution for Al in garnet results in a ~0.1 log fO_2 shift (Donohue and Essene, 2000). Fortunately, stoichiometry using compositions from electron microprobe analysis in garnets reveal low andradite component, >1.5% *And* for garnet core and >1% *And* for garnet rim compositions, for all garnets from this study so little to no error is expected from Fe^{3+} substitution in garnet.

2.3.3 Iron Isotope Analysis

The iron isotopic analyses reported and discussed in this study for samples 09DSF-23E, 09DSF-54A, 14BSY-35C, and 06MSF-6C, represent the first zoned analysis of iron isotope compositions in a single mineral grain. Iron isotope compositions analyzed in this study yield a change in composition between garnet cores and rim with heavier rims (higher $\delta^{56}Fe$ values) and lighter core and middle zones (lower $\delta^{56}Fe$ values) for samples 09DSF-23E, 09DSF-54A, and 14BSY-35C. Iron isotope analysis for sample 06MSF-6C shows no significant change from garnet core to rim.

Discussion of iron isotopic results from sample 14BSY-35C follows the discussion of results from samples 09DSF-23E and 09DSF-54A in Chapter 1. While bulk rock $Fe^{3+}/\Sigma Fe$ ratios can become decoupled from the fO_2, the inverse correlation we see spatially from garnet core to rim between decreasing fO_2 and increasing $\delta^{56}Fe$ values shown in Figure 1.2 for samples 09DSF-23E, 09DSF-54A, and 06MSF-6C and Figure 2.10 for sample 14BSY-35C, support the hypothesis that iron isotope fractionation is reflecting changes in redox during subduction. To account for the observed covariation between higher fO_2 and lighter $\delta^{56}Fe$ in garnet cores relative to lower fO_2 and heavier $\delta^{56}Fe$ in garnet rims, we propose three possible mechanisms. First, iron isotope fractionation occurs as an open system process, controlled by the solubility difference between Fe^{2+} and Fe^{3+} within a fluid. The release of oxidizing fluid during lawsonite dehydration leaves behind a more reduced residual mineral assemblage enriched in Fe^{2+}. With the presence and increase of reduced iron (Fe^{2+}) in the system, the solubility of Fe^{2+} and relatively insolubility of Fe^{3+} (Polyakoy and Mineev, 2000; Schauble et al., 2001) facilitates iron isotope fractionation as lighter iron isotopes are preferentially complexed and incorporated into oxidizing sulfate, hyper-saline, and carbonate-bearing fluids (Debret et al., 2016), which are removed from the system. In this scenario the progressive removal of Fe^{2+} bearing isotopically light fluids is recorded by prograde garnet growth, and can explain the shift from light to heavy Fe isotopes between garnet cores and rims.

Second, iron isotope fractionation is controlled by the bulk rock $Fe^{3+}/\Sigma Fe$ ratio in a closed system (with respect to Fe) with changing oxygen fugacity. Lawsonite dehydration releases oxidizing fluids (Groppo and Castelli, 2010), changing the fO_2 of the system, leaving behind a more reduced residual mineral assemblage enriched in Fe^{2+}. This fO_2 change does not change the whole rock Fe isotope composition, but instead, as garnet more readily incorporates isotopically light Fe^{2+}, causes a shift towards heavier $\delta^{56}Fe$ values within garnet crystal rims due to Rayleigh fractionation and matrix re-equilibrium. Third, lighter iron isotopes are continuously removed from the system as garnet takes in mainly Fe^{+2} during growth. As lighter iron isotopes are preferentially incorporated in bonds with Fe^{2+}, the removal and isolation of Fe^{2+} within the garnet would result in light iron isotope enrichment in the mineral garnet and depletion in the surrounding system with a shift towards higher $\delta^{56}Fe$ values in garnet crystal rims.

While it's difficult to determine which is the dominant mechanism responsible for the observed iron isotope fractionation, it is plausible that during garnet growth in sample 14BSY-35C a combination of these mechanisms contributed. As discussed in Chapter 1, thermodynamic modeling and petrologic observations suggest that garnet in samples 09DSF-23E and 09DSF-54A grew through the lawsonite breakdown reaction and the subsequent release of a free fluid phase (Chapter 1). Because of this, iron isotope fractionation in samples 09DSF-23E and 09DSF-54A is likely caused by the enrichment light iron isotope compositions within the free fluid phase and subsequent removal of the fluid from the system.

As thermodynamic modeling of sample 14BSY-35C was unsuccessful (Kendall 2016) and petrologic observations do not suggest that garnets in this sample grew through lawsonite breakdown and dehydration, understanding the dominant mechanism responsible for the iron isotope fractionation between garnet core and rim is more challenging. It is possible that iron isotope compositional differences in sample 14BSY-35C were caused by the continuous removal and isolation of lighter iron isotopes from the system as garnet grows and takes in mainly Fe^{+2} during growth, the process described in mechanism three above. This mechanism is not driven by a change in redox but by Rayleigh fractionation. While it is possible that Rayleigh fractionation during garnet growth does contribute to the garnet core to rim change in iron isotope compositions in sample 14BSY-35C, the large fO_2 change from garnet core to rim suggests that a redox controlled mechanism may be responsible for the iron isotope compositional differences.

If garnets in sample 14BSY-35C did grow during the breakdown of a hydrous mineral, like samples 09DSF-23E and 09DSF-54A, the fractionation of iron isotopes could be controlled by the loss of isotopically light iron within oxidizing fluids and the resulting re-equilibration of iron barring minerals within the more reduced system. Due to the correlation in redox and iron isotope composition changes from garnet core to rim, sample 14BSY-35C provides additional support for the conclusions presented in Chapter 1 that core to rim iron isotope variations in garnet are a sensitive recorder of redox process occurring during prograde metamorphism of subducting oceanic lithosphere.

2.3.4 Implications of fO_2 and Iron Isotope Analysis

Coupled fO_2 and iron isotope analysis presented in this study represent the first zoned fO_2 and $\delta^{56}Fe$ analysis in a single mineral grain. Samples 09DSF-23E, 09DSF-54A, and 14BSY-35C show a significant change from more oxidized garnet cores (higher *f*O2) with a lighter iron isotope signature (lower δ^{56}Fe) isotopes to more reduced garnet rims (lower *f*O2) with a heavier iron isotope signature (higher δ^{56}Fe). Sample 06MSF-6C shows no significant change in calculated fO_2 values from garnet core to rim and only minor variation in δ^{56}Fe, with only slightly lighter δ^{56}Fe in the garnet core than in the garnet rim. The relationship between fO_2 and δ^{56}Fe in this study implies there is a direct correlation between redox change and iron isotope fractionation during prograde subduction.

These data give insight into the effects that processes, like the breakdown and subsequent dehydration of lawsonite, have in the subducting slab during prograde subduction. This study reveals that the breakdown and dehydration of lawsonite releases an oxidized fluid, enriched in lighter δ^{56}Fe, leaving a more reduced slab mineral assemblage. The release of this oxidizing fluid from the subducting oceanic crust not only effects the mineral assemblage in subducting slab but also has implications in the sub arc mantle region. This study provides the first direct record of the source of oxidized fluid coming from the oceanic crust during subduction and with this direct evidence, provides a mechanism to explain sub arc mantle and arc volcanic oxidation.

Arc magmas are oxidized, enriched in volatiles, and show unusual trace element chemistry compared to their mantle source region (Kelley and Cottrell, 2009). Much debate exists about the role of slab derived fluids in oxidizing the sub arc mantle and explaining the oxidized signatures and volatile enrichment observed in arc magmas (Debret and Sverjensky, 2017; Kelley and Cottrell, 2009; Lee et al., 2010; Evens et al., 2012; Breeding et al., 2004; Marschall and Schumacher, 2012; Groppo and Castelli, 2010;

Parkinson and Arculus, 1999; Schmidt and Poli, 1998; Wood et al., 1990; Tatsumi, 1986). It is generally accepted that fluids coming off the subducting slab are responsible for altering the sub arc mantle region (Debret and Sverjensky, 2017; Kelley and Cottrell, 2009; Evens et al., 2012; Breeding et al., 2004), the source region for arc magmas.

It has been alternatively suggested that oxidation of arc magmas may not be linked to slab derived fluids but rather oxidize through crustal assimilation (Lee et al., 2005), magma differentiation (Ming et al., 2018; Lee et al., 2010; Lee et al., 2005), or degassing (Christie et al., 1986; Sato and Wright, 1966). While these mechanisms provide a plausible hypothesis for oxidation, it is unlikely that oxidation of the sub arc mantle is uninfluenced by oxidized material coming off the subducting slab, as it has been shown that continental lithosphere near subduction zones incorporates both asthenospheric and subduction derived signatures (Wood et al., 1990) and arc volcanics are oxidized and enriched in volatiles relative to the mantle (Kelley and Cottrell, 2009; Evens et al., 2012; Breeding et al., 2004; Schmidt and Poli, 1998; Wood et al., 1990; Tatsumi, 1986). Explanation of these observations is difficult without the migration and alteration of the sub arc mantle region by oxidized slab-derived fluids. Any successful alternatives would have to show either that slab-derived fluids do not have the oxidizing potential to overcome the redox-buffering capacity of the mantle or that the fluids did not leave the subducting slab or slab-mantle interface; the latter then requires an alternative mechanism responsible for the oxidation and volatile enrichment seen in the sub arc mantle and arc magmas.

This study provides the first direct record of the source of oxidized fluids coming off the subducting slab due to lawsonite breakdown during prograde subduction. With the likely migration of these fluids into the mantle wedge, these data support the idea that slab-derived fluids impart an oxidize and volatile rich signature to the sub arc mantle, the source region for primary arc magmas.

2.4 CONCLUSION

The data presented in this study represent the first zoned *f*O_2 and iron isotope analysis in a single mineral grain, confirms the use of iron isotopes as a redox tracer during prograde subduction, and reveals the first record of the source of oxidizing fluids released from the oceanic crust during subduction. Additionally, these data show that there is significant redox change recorded in the slab during prograde subduction. The breakdown of lawsonite is the key fluid-producing and redox-driving process during subduction that releases oxidizing fluids carrying dissolved Fe^{2+} and light iron isotopic signatures into the sub-arc mantle, leaving behind a progressively reduced residual slab mineral assemblage with higher δ^{56}Fe. Much debate exists about the role of slab derived fluids in oxidizing the sub arc mantle and arc magmas. However, the results of this study support the hypothesis that dehydration accompanying lawsonite breakdown during prograde subduction plays an important and measureable role in the global redox budget and provides a mechanism for sub arc mantle oxidation, the source region for primary arc magmas.

2.5 TABLES

Table 2.1 – GPS coordinates for all samples.

Sample	**Location**	**Country**	**GPS Coordinates**
09DSF-23E	Sifnos	Greece	N 37° 01.598′, E 24° 39.396′
09DSF-54A	Sifnos	Greece	N 37° 00.930′, E 24° 39.360′
06MSF-6C	Sifnos	Greece	N 37° 01.561′, E 24° 39.452′
14BSY-35C	Syros	Greece	N 37° 23.134′, E 24° 56.894′
09DSF-37A	Sifnos	Greece	N 37° 01.948′, E 24° 39.745′
G17-S825A02	Lago di Cignana	Italy	N 45° 52.705', E 07° 35.549'
G17-S825A03	Lago di Cignana	Italy	N 45° 52.704', E 07° 35.578'

Table 2.2 – Compositional data from the MIT electron microprobe of epidote inclusions and adjacent garnet points from sample 14BSY-35C.

	Cr2O3	Al2O3	CaO	MnO	Na2O	TiO2	SiO2	K2O	FeO	MgO	Total
Ep in 1	0.054	23.050	22.570	0.107	0.000	0.140	36.890	0.000	13.600	0.007	96.418
Ep in 2	0.010	23.850	23.150	0.030	0.000	0.316	37.450	0.000	12.970	0.000	97.776
Ep in 3	0.012	23.530	22.920	0.092	0.000	0.042	37.450	0.000	13.100	0.003	97.149
Ep in 4	0.000	23.540	22.750	0.173	0.000	0.116	37.160	0.000	13.420	0.000	97.160
Ep in 5	0.066	28.070	23.020	0.033	0.000	0.075	37.180	0.000	7.330	0.060	95.834
Ep in 6	0.035	23.660	23.170	0.086	0.000	0.197	37.160	0.000	13.450	0.000	97.758
Ep in 7	0.014	23.990	23.210	0.064	0.000	0.050	37.480	0.000	13.240	0.001	98.047
Ep in 8	0.026	23.060	23.070	0.074	0.000	0.134	37.440	0.015	13.600	0.002	97.421
Ep in 9	0.027	28.850	23.350	0.036	0.000	0.136	37.820	0.000	6.430	0.077	96.725
Ep in 10	0.087	27.870	22.740	0.027	0.000	0.083	37.540	0.000	7.440	0.074	95.861
Ep in 11	0.001	23.500	23.050	0.112	0.002	0.123	37.210	0.000	13.200	0.009	97.207
Ep in 12	0.004	22.950	20.900	0.059	0.998	0.067	38.910	0.000	12.920	0.013	96.821
Ep in 13	0.000	24.580	23.260	0.046	0.022	0.103	37.590	0.000	12.110	0.003	97.715
Gt by ep 1	0.031	21.770	8.170	0.451	0.073	0.103	36.900	0.000	33.000	0.904	101.401
Gt by ep 2	0.059	21.870	8.090	0.427	0.039	0.099	36.910	0.003	33.240	0.804	101.542
Gt by ep 3	0.023	21.770	8.710	0.566	0.109	0.210	37.460	0.000	32.520	0.746	102.113
Gt by ep 4	0.059	21.770	9.830	0.418	0.049	0.163	37.370	0.003	31.620	0.708	101.991
Gt by ep 5	0.000	22.040	11.850	0.791	0.028	0.046	37.860	0.000	27.800	1.363	101.777
Gt by ep 6	0.007	22.120	8.240	0.361	0.047	0.047	37.530	0.000	32.840	1.031	102.222
Gt by ep 7	0.034	21.850	9.060	0.403	0.075	0.173	37.120	0.000	32.210	0.835	101.760
Gt by ep 8	0.034	21.850	9.060	0.403	0.075	0.173	37.120	0.000	32.210	0.835	101.760
Gt by ep 9	0.000	22.140	11.340	0.795	0.077	0.034	38.070	0.001	27.800	1.471	101.728
Gt by ep 10	0.023	22.220	11.600	0.798	0.040	0.011	37.870	0.002	27.660	1.366	101.591
Gt by ep 11	0.028	21.960	9.060	0.331	0.088	0.097	37.350	0.000	32.070	0.999	101.981
Gt by ep 12	0.041	22.000	7.990	0.335	0.073	0.084	36.840	0.002	33.140	1.056	101.561
Gt by ep 13	0.031	22.080	8.310	0.344	0.005	0.072	37.480	0.000	33.000	1.097	102.418

Table 2.3 – Compositional data from the MIT electron microprobe of epidote inclusions from sample 09DSF-37A.

	Cr2O3	Al2O3	CaO	MnO	Na2O	TiO2	SiO2	K2O	FeO	MgO	Total
Ep 1	0.025	30.230	23.680	0.506	0.016	0.111	38.150	0.000	5.100	0.012	97.830
Ep 2	0.019	32.740	24.330	0.188	0.030	0.358	38.450	0.000	2.470	0.003	98.588
Ep 3	0.046	29.200	23.260	0.296	0.037	0.068	37.780	0.001	7.080	0.018	97.786
Ep 4	0.087	26.810	23.510	0.286	0.049	0.115	37.580	0.004	9.720	0.007	98.168
Ep 5	0.044	26.710	23.140	0.439	0.015	0.128	37.630	0.009	10.120	0.008	98.244
Ep 6	0.000	31.730	23.910	0.300	0.002	0.062	37.940	0.000	4.500	0.000	98.444
Ep 7	0.000	30.650	24.210	0.308	0.000	0.111	38.140	0.000	4.820	0.011	98.249
Ep 8	0.077	31.600	23.630	0.286	0.000	0.036	37.840	0.000	4.550	0.007	98.026
Ep 9	0.043	26.880	23.570	0.376	0.002	0.119	37.880	0.007	9.720	0.003	98.599
Ep 10	0.140	28.970	23.230	0.910	0.000	0.182	37.900	0.002	6.590	0.005	97.930
Ep 11 core	0.026	28.630	23.410	0.132	0.019	0.116	38.130	0.004	7.350	0.050	97.867
Ep 11 rim	0.094	23.300	22.340	0.304	0.054	0.037	36.490	0.005	13.310	0.126	96.060
Ep 12	0.036	24.940	23.400	0.216	0.018	0.098	37.680	0.006	11.530	0.001	97.924
Ep 13 rim	0.023	25.910	23.520	0.100	0.004	0.074	37.590	0.003	10.530	0.012	97.767
Ep 13 core	0.017	28.750	23.480	0.082	0.000	0.110	38.310	0.003	6.930	0.051	97.732
Ep 14	0.025	25.290	23.290	0.172	0.026	0.235	37.740	0.006	11.520	0.000	98.304
Ep 15	0.051	25.930	23.530	0.144	0.000	0.086	37.750	0.000	10.510	0.004	98.006
Ep 16	0.043	25.310	23.660	0.162	0.000	0.060	37.550	0.006	11.310	0.000	98.101
Ep 17	0.080	28.520	23.630	0.228	0.000	0.064	37.880	0.000	7.910	0.000	98.312
Ep 18	0.000	29.110	24.110	0.225	0.000	0.111	38.190	0.000	6.600	0.002	98.348
Matrix ep	0.041	30.470	23.920	0.151	0.092	0.114	39.470	0.008	5.720	0.047	100.033
Ep 19	0.028	30.540	23.090	0.641	0.059	0.074	38.090	0.000	5.600	0.142	98.264
Ep 20	0.078	26.010	23.440	0.268	0.024	0.083	37.820	0.000	10.460	0.014	98.197
Ep 21	0.096	30.510	24.140	0.141	0.004	0.048	38.200	0.000	4.990	0.043	98.173
Ep 22	0.059	29.530	23.220	0.904	0.002	0.225	38.100	0.003	6.410	0.025	98.477
Ep 23	0.042	29.100	23.180	0.477	0.025	0.094	37.730	0.000	6.970	0.024	97.641
Ep 24	0.075	30.500	24.050	0.470	0.000	0.130	38.580	0.000	5.390	0.042	99.237
Ep 25	0.115	26.710	22.640	0.357	0.000	0.082	36.760	0.000	8.850	0.134	95.648

Table 2.4 – Compositional data from the MIT electron microprobe of garnet points near labeled epidote inclusions from sample 09DSF-37A.

	Cr2O3	Al2O3	CaO	MnO	Na2O	TiO2	SiO2	K2O	FeO	MgO	Total
Gt by ep 1	0.097	22.160	8.090	1.257	0.000	0.116	37.850	0.000	29.890	2.820	102.280
Gt by ep 2	0.097	22.160	8.090	1.257	0.000	0.116	37.850	0.000	29.890	2.820	102.280
Gt by ep 3	0.079	22.060	8.320	0.940	0.074	0.151	37.650	0.000	31.000	2.190	102.465
Gt by ep 4	0.079	22.060	8.320	0.940	0.074	0.151	37.650	0.000	31.000	2.190	102.465
Gt by ep 5	0.079	22.060	8.320	0.940	0.074	0.151	37.650	0.000	31.000	2.190	102.465
Gt by ep 6	0.096	22.070	8.120	1.970	0.084	0.185	37.530	0.000	30.290	1.830	102.175
Gt by ep 7	0.096	22.070	8.120	1.970	0.084	0.185	37.530	0.000	30.290	1.830	102.175
Gt by ep 8	0.039	21.850	7.550	3.410	0.021	0.162	37.270	0.000	30.160	1.651	102.112
Gt by ep 9	0.073	21.910	7.500	3.390	0.033	0.182	37.320	0.000	29.270	1.760	101.438
Gt by ep 10	0.047	21.910	7.710	3.340	0.064	0.191	37.460	0.000	29.770	1.720	102.212
Gt by ep 11	0.107	22.040	7.750	2.820	0.028	0.153	37.420	0.000	30.020	1.830	102.168
Gt by ep 12	0.107	22.040	7.750	2.820	0.028	0.153	37.420	0.000	30.020	1.830	102.168
Gt by ep 13	0.100	21.950	8.630	1.233	0.058	0.151	37.700	0.001	29.840	2.030	101.693
Gt by ep 14	0.100	21.950	8.630	1.233	0.058	0.151	37.700	0.001	29.840	2.030	101.693
Gt by ep 15	0.075	22.130	7.970	0.900	0.008	0.126	37.670	0.000	30.710	2.230	101.819
Gt by ep 16	0.075	22.130	7.970	0.900	0.008	0.126	37.670	0.000	30.710	2.230	101.819
Gt by ep 17	0.104	23.090	8.470	0.715	0.000	0.120	37.670	0.003	29.640	2.610	102.421
Gt by ep 18	0.104	23.090	8.470	0.715	0.000	0.120	37.670	0.003	29.640	2.610	102.421
Gtrim by mx	0.070	21.820	8.460	1.264	0.013	0.100	37.580	0.000	28.580	3.120	101.006
Gt by ep 19	0.088	21.990	8.170	1.410	0.000	0.068	37.980	0.000	28.800	2.950	101.456
Gt by ep 20	0.025	22.100	8.030	0.842	0.036	0.091	37.540	0.000	30.370	2.350	101.383
Gt by ep 21	0.025	22.100	8.030	0.842	0.036	0.091	37.540	0.000	30.370	2.350	101.383
Gt by ep 22	0.040	22.080	8.030	2.020	0.008	0.125	37.370	0.000	30.730	1.840	102.243
Gt by ep 23	0.040	22.080	8.030	2.020	0.008	0.125	37.370	0.000	30.730	1.840	102.243
Gt by ep 24	0.002	21.960	7.400	3.980	0.000	0.143	37.540	0.000	28.790	1.820	101.635
Gt by ep 25	0.025	21.490	7.540	4.020	0.033	0.152	36.550	0.000	27.940	1.700	99.450

Table 2.5 – Garnet and epidote activities for sample 14BSY-35C.

	py	gr	alm	spss	andr	cz	ep
Ep in 1						0.24	0.69
Ep in 2						0.28	0.67
Ep in 3						0.25	0.69
Ep in 4						0.26	0.67
Ep in 5						0.63	0.36
Ep in 6						0.27	0.69
Ep in 7						0.28	0.68
Ep in 8						0.22	0.72
Ep in 9						0.66	0.32
Ep in 10						0.59	0.37
Ep in 11						0.26	0.69
Ep in 12						0.17	0.59
Ep in 13						0.33	0.64
Gt by ep 1	0.000199	0.02	0.34	0.0000011			
Gt by ep 2	0.000139	0.019	0.36				
Gt by ep 3	0.000114	0.023	0.34	0.0000021			
Gt by ep 4	0.000109	0.031	0.31				
Gt by ep 5	0.00081	0.053	0.2	0.000053			
Gt by ep 6	0.000275	0.02	0.35				
Gt by ep 7	0.000168	0.026	0.32				
Gt by ep 8	0.000168	0.026	0.32				
Gt by ep 9	0.00096	0.048	0.21	0.0000055			
Gt by ep 10	0.0008	0.05	0.21	0.0000055			
Gt by ep 11	0.00028	0.026	0.31				
Gt by ep 12	0.00031	0.019	0.33				
Gt by ep 13	0.000328	0.021	0.34				

Table 2.6 – Epidote activities for sample 09DSF-37A.

	cz	ep
Ep 1	0.74	0.24
Ep 2	0.95	0.038
Ep 3	0.66	0.3
Ep 4	0.5	0.49
Ep 5	0.47	0.49
Ep 6	0.86	0.13
Ep 7	0.79	0.23
Ep 8	0.85	0.12
Ep 9	0.49	0.51
Ep 10	0.64	0.32
Ep 11 core	0.61	0.37
Ep 11 rim	0.26	0.67
Ep 12	0.35	0.62
Ep 13 rim	0.43	0.56
Ep 13 core	0.62	0.36
Ep 14	0.37	0.59
Ep 15	0.43	0.55
Ep 16	0.39	0.6
Ep 17	0.61	0.37
Ep 18	0.67	0.35
Matrix ep	0.68	0.27
Ep 19	0.72	0.21
Ep 20	0.43	0.55
Ep 21	0.78	0.23
Ep 22	0.66	0.28
Ep 23	0.65	0.31
Ep 24	0.74	0.25
Ep 25	0.53	0.45

Table 2.7 – Garnet activities for sample 09DSF-37A.

	py	gr	alm	spss	andr
Gt by ep 1	0.0043	0.021	0.23	0.000022	
Gt by ep 2	0.0043	0.021	0.23	0.000022	
Gt by ep 3	0.0022	0.021	0.25	0.0000094	
Gt by ep 4	0.0022	0.021	0.25	0.0000094	
Gt by ep 5	0.00239	0.022	0.25	0.000094	
Gt by ep 6	0.00145	0.02	0.25	0.000088	
Gt by ep 7	0.00145	0.02	0.25	0.000088	
Gt by ep 8	0.00115	0.0164	0.25	0.00047	
Gt by ep 9	0.00137	0.0166	0.25	0.00047	
Gt by ep 10	0.00131	0.017	0.24	0.00043	
Gt by ep 11	0.00154	0.018	0.25	0.00026	
Gt by ep 12	0.00141	0.017	0.25	0.00026	
Gt by ep 13	0.00198	0.024	0.25	0.000022	
Gt by ep 14	0.00198	0.024	0.25	0.000022	
Gt by ep 15	0.0022	0.019	0.28	0.0000085	
Gt by ep 16	0.0022	0.019	0.28	0.0000085	
Gt by ep 17	0.0036	0.023	0.24	0.000004	
Gt by ep 18	0.0036	0.023	0.24	0.000004	
Gtrim by mx	0.006	0.025	0.2	0.000023	
Gt by ep 19	0.0048	0.022	0.23	0.000032	
Gt by ep 20	0.00262	0.02	0.26	0.000007	
Gt by ep 21	0.00284	0.021	0.26	0.000007	
Gt by ep 22	0.00145	0.019	0.26	0.000095	
Gt by ep 23	0.00145	0.019	0.26	0.000095	
Gt by ep 24	0.00146	0.016	0.24	0.00075	
Gt by ep 25	0.00136	0.017	0.22	0.00081	

Table 2.8 –14BSY-35C iron isotope composition data including IRMM points for calculation.

	Raw Intensities (V)							Raw Ratios			IEC Ratios				
Name	**53Cr**	**54Fe**	**56Fe**	**56.907Fe**	**58Fe**	**60Ni**	**61Ni**	**56/54Fe**	**56.902/54Fe**	**58/54Fe**	**56/54Fe**	**56.902/54Fe**	**58/54Fe**	**$\delta^{56/54}Fe_{IRMM14}$**	**$\delta^{57/54}Fe_{IRMM14}$**
IRMM	0.0003061	1.2952884	21.7634700	0.5195035	0.0715045	0.0001514	0.0001424	16.8020880	0.4010720	0.0552025	16.8030750	0.4010935	0.0523238		
333.7	0.0002962	1.2459731	20.9330410	0.4996632	0.0687687	0.0001503	0.0001369	16.8006500	0.4010243	0.0551952	16.8016450	0.4010480	0.0522677	**-0.1424**	**-0.1930**
IRMM	0.0002917	1.2609418	21.1889420	0.5058106	0.0696056	0.0001504	0.0001378	16.8040340	0.4011342	0.0552012	16.8050020	0.4011574	0.0522878		
IRMM	0.0002857	1.3203177	22.2253460	0.5286097	0.0719165	0.0001501	0.0001399	16.8334510	0.4003623	0.0544652	16.8343600	0.4003838	0.0517055		
333.7	0.0002824	1.2996323	21.8698200	0.5202257	0.0708532	0.0001461	0.0001403	16.8280510	0.4002899	0.0545128	16.8289620	0.4003116	0.0517877	**-0.1031**	**-0.2533**
IRMM	0.0002805	1.3223760	22.2501700	0.5295075	0.0721329	0.0001457	0.0001380	16.8262420	0.4004210	0.0545478	16.8270340	0.4004421	0.0518737		
IRMM	0.000293	1.626040	27.267504	0.650162	0.089415	0.000154	0.000142	16.769217	0.399842	0.054989	16.769971	0.399858	0.052699		
333.7	0.000293	1.609155	26.979304	0.643280	0.088418	0.000146	0.000140	16.766811	0.399763	0.054947	16.767569	0.399781	0.052712	**-0.1115**	**-0.1477**
IRMM	0.000302	1.645940	27.599352	0.658053	0.090483	0.000154	0.000142	16.768140	0.399804	0.054973	16.768905	0.399822	0.052683		
333.7	0.000297	1.612004	27.027258	0.644372	0.088566	0.000153	0.000141	16.766280	0.399737	0.054943	16.767089	0.399755	0.052637	**-0.1084**	**-0.1582**
IRMM	0.000293	1.632031	27.366064	0.652474	0.089725	0.000153	0.000143	16.768160	0.399797	0.054976	16.768909	0.399815	0.052677		
333.8	0.000293	1.603613	26.889549	0.641136	0.088076	0.000156	0.000141	16.768087	0.399805	0.054924	16.768852	0.399823	0.052566	**-0.0148**	**-0.0057**
IRMM	0.000295	1.644856	27.581700	0.657631	0.090423	0.000152	0.000145	16.768498	0.399818	0.054973	16.769292	0.399836	0.052705		
IRMM	2.93E-04	1.73E+00	2.90E+01	6.90E-01	9.46E-02	1.51E-04	1.42E-04	1.68E+01	3.99E-01	5.48E-02	1.68E+01	3.99E-01	5.26E-02		
333.8	2.94E-04	1.68E+00	2.82E+01	6.72E-01	9.20E-02	1.51E-04	1.41E-04	1.68E+01	3.99E-01	5.47E-02	1.68E+01	3.99E-01	5.26E-02	**-0.0402**	**-0.0386**
IRMM	2.99E-04	1.73E+00	2.89E+01	6.90E-01	9.46E-02	1.53E-04	1.44E-04	1.68E+01	3.99E-01	5.48E-02	1.68E+01	3.99E-01	5.26E-02		
IRMM	0.000296	1.651373	27.671257	0.659595	0.090620	0.000152	0.000148	16.756546	0.399422	0.054875	16.757293	0.399440	0.052655		
333.8	0.000302	1.624272	27.214446	0.648658	0.089543	0.000151	0.000148	16.754894	0.399356	0.055127	16.755668	0.399374	0.052835	**-0.0633**	**-0.1020**
IRMM	0.000299	1.663193	27.867341	0.664236	0.091234	0.000154	0.000150	16.755415	0.399372	0.054855	16.756164	0.399390	0.052582		
333.8	0.000302	1.632222	27.346177	0.651780	0.089970	0.000157	0.000150	16.753909	0.399321	0.055120	16.754681	0.399339	0.052765	**-0.0699**	**-0.1140**
IRMM	0.000303	1.668932	27.962585	0.666497	0.091570	0.000157	0.000156	16.754781	0.399362	0.054867	16.755540	0.399380	0.052536		

Table 2.9 –Four runs for garnet cores and rims for sample 14BSY-35C. Table includes iron isotope averages of garnet core and rim with error.

$\delta^{56/54}Fe_{IRMM14}$	**Run 1**	**Run 2**	**Run 3**	**Run 4**	**Average**	**2sd**
Core	-0.111	-0.108	-0.142	-0.103	-0.116	0.035
Rim	-0.015	-0.040	-0.063	-0.070	-0.047	0.050
$\delta^{57/54}Fe_{IRMM14}$	**Run 1**	**Run 2**	**Run 3**	**Run 4**	**Average**	**2sd**
Core	-0.148	-0.158	-0.193	-0.253	-0.188	0.095
Rim	-0.006	-0.039	-0.102	-0.114	-0.065	0.103

Table 2.10 – 09DSF-37A fO_2 results given as temperatures for logfO_2 values. These results are plotted in Figure 2.11.

fO2	-34	-32	-30	-28	-26	-24	-22	-20	-18	-16	-14
ep1	258	282	308	337	404	443	486	534	589	651	
ep2	298	325	356	389	427	468	514	566	625	692	
ep3	255	278	304	332	363	398	436	478	525	579	639
ep4	245	268	293	320	349	382	419	460	505	555	613
ep5	250	273	298	325	355	389	426	466	512	563	621
ep6	275	300	328	358	392	429	471	517	568	627	694
ep7	263	288	314	343	375	411	450	493	542	597	660
ep8	278	304	331	362	396	433	474	520	572	631	698
ep9	250	272	297	324	354	387	424	464	508	559	616
ep10	259	282	308	336	367	402	439	481	528	581	641
ep11	257	280	306	334	364	399	436	478	524	576	636
ep11two	246	268	292	319	348	380	416	456	499	549	604
ep12	242	265	289	315	344	376	412	451	495	544	600
ep13	249	271	296	323	353	386	423	464	509	560	617
ep13two	257	281	306	334	365	400	438	480	528	581	641
ep14	248	270	295	322	352	385	421	462	507	557	614
ep15	242	265	289	316	346	378	414	454	499	549	605
ep16	241	263	287	314	343	376	412	451	495	545	601
ep17	251	275	300	328	358	393	430	472	518	571	630
ep18	253	276	301	329	360	394	432	474	521	574	633
epMATRIX	258	281	307	336	367	403	441	484	532	586	648
ep19	262	286	312	341	373	409	449	492	541	597	660
ep20	243	265	290	316	346	378	415	455	499	549	606
ep21	264	289	315	344	376	412	451	495	544	599	662
ep22	259	283	309	337	369	404	442	485	532	586	647
ep23	257	281	306	335	366	400	438	481	528	581	641
ep24	263	287	313	341	373	408	446	489	537	591	652
ep25	252	274	299	327	347	390	427	467	512	563	621

Table 2.11 – Pressures and temperatures used in oxybarometry calculations for sample 14BSY-35C and oxygen fugacity and iron isotope results.

	T (°C)	P (kbar)	log$f$O$_2$ (bar)	ΔlogFMQ (bar)	fO$_2$ error (bar)	$\delta^{56/54}$Fe (‰)	2std (‰)
ep5	528	24.2	-18	2.7	0.2	-0.047	0.05
ep1	502	23.2	-17.3	3.4	0.2	-0.12	0.04
ep2	502	23.2	-17.3	3.4	0.2	-0.12	0.04
ep3	502	23.2	-17.5	3.2	0.2	-0.12	0.04
ep4	502	23.2	-17.6	3.1	0.2	-0.12	0.04
ep6	502	23.2	-17.4	3.3	0.2	-0.12	0.04
ep7	502	23.2	-17.6	3.1	0.2	-0.12	0.04
ep8	502	23.2	-17.5	3.2	0.2	-0.12	0.04
ep11	502	23.2	-17.6	3.1	0.2	-0.12	0.04
ep12	502	23.2	-17.5	3.2	0.2	-0.12	0.04
ep13	502	23.2	-17.5	3.2	0.2	-0.12	0.04
ep9	528	24.2	-18.2	2.5	0.2	-0.047	0.05
ep10	528	24.2	-18	2.7	0.2	-0.047	0.05

Table 2.12 – Procedure of each partial dissolution test, described in greater detail in the methods section, the analyte, either garnet residue or leachate, and the $\delta^{56/54}$Fe and $\delta^{57/54}$Fe compositions with reported error for all tests. This data is presented in Figure 2.12.

Sample	**Procedure**	**Analyte**	**δ^{56}Fe (‰)**	**δ^{56}Fe Error (‰)**	**δ^{57}Fe (‰)**	**δ^{57}Fe Error (‰)**
Gt K	No partial	Garnet residue	0.015	0.046	0.038	0.023
Gt G	Nitric only	Garnet residue	0.085	0.028	0.094	0.130
Gt G HNO_3	Nitric only	Nitric leachate	0.049	0.044	0.101	0.074
Gt H	HF only	Garnet residue	0.080	0.050	0.139	0.070
Gt H HF	HF only leach	HF leachate	0.004	0.016	0.054	0.035
Gt F	Baxter partial	Garnet residue	0.053	0.015	0.098	0.034
Gt J	2 stage (nitric leach)	Garnet residue	0.092	0.046	0.180	0.141
Gt J HNO_3	2 stage (nitric leach)	Nitric leachate	0.055	0.032	0.096	0.077
Gt I	2 stage (HF leach)	Garnet residue	0.127	0.016	0.207	0.101
Gt I HF	2 stage (HF leach)	HF leachate	0.034	0.033	0.094	0.065
Gt D	2 stage combined	Garnet residue	0.060	0.033	0.109	0.050
Gt D HF+HNO_3	2 stage combined	Nitric and HF leachate	0.061	0.034	0.111	0.070

Table 2.13 – Oxygen fugacity calculated using 2σ uncertainty of Palin et al. (2016) for thermodynamic pseudosection *PT* estimates of ±1 kbar and ±40°C for epidote inclusions 6, 11, and 21 from sample 06MSF-6C.

	Condition	Temperature (°C)	Pressure (kbar)	fO2 (log)	FMQ	ΔlogFMQ
Ep6	Original	535	21.5	-16.6	-19.7	3.1
	Up P	535	22.5	-16.4	-19.6	3.2
	Down P	535	20.5	-16.8	-19.8	3
	Up T	575	21.5	-15.25	-18.35	3.1
	Down T	495	21.5	-18.3	-21.25	2.95
	Down P, Up T	575	20.5	-15.4	-18.4	3
	Up P, Down T	495	22.5	-18	-21.15	3.15
	Up P, Up T	575	22.5	-14.9	-18.2	3.3
	Down P, Down T	495	20.5	-18.5	-21.4	2.9
Ep 11	Original	470	20.2	-19.1	-22.5	3.4
	Up P	470	21.2	-18.8	-22.4	3.6
	Down P	470	19.2	-19.35	-22.65	3.3
	Up T	520	20.2	-16.9	-20.4	3.5
	Down T	430	20.2	-21.05	-24.4	3.35
	Down P, Up T	520	19.2	-17.15	-20.6	3.45
	Up P, Down T	430	21.2	-20.75	-24.25	3.5
	Up P, Up T	520	21.2	-16.6	-20.1	3.5
	Down P, Down T	430	19.2	-21.3	-24.5	3.2
Ep 21	Original	530	21.4	-16.9	-19.9	3
	Up P	530	22.4	-16.6	-19.8	3.2
	Down P	530	20.4	-17.1	-20	2.9
	Up T	570	21.4	-15.4	-18.5	3.1
	Down T	490	21.4	-18.6	-21.5	2.9
	Down P, Up T	570	20.4	-15.6	-18.6	3
	Up P, Down T	490	22.4	-18.3	-21.4	3.1
	Up P, Up T	570	22.4	-15.2	-18.4	3.2
	Down P, Down T	490	20.4	-18.8	-21.6	2.8

2.6 FIGURES

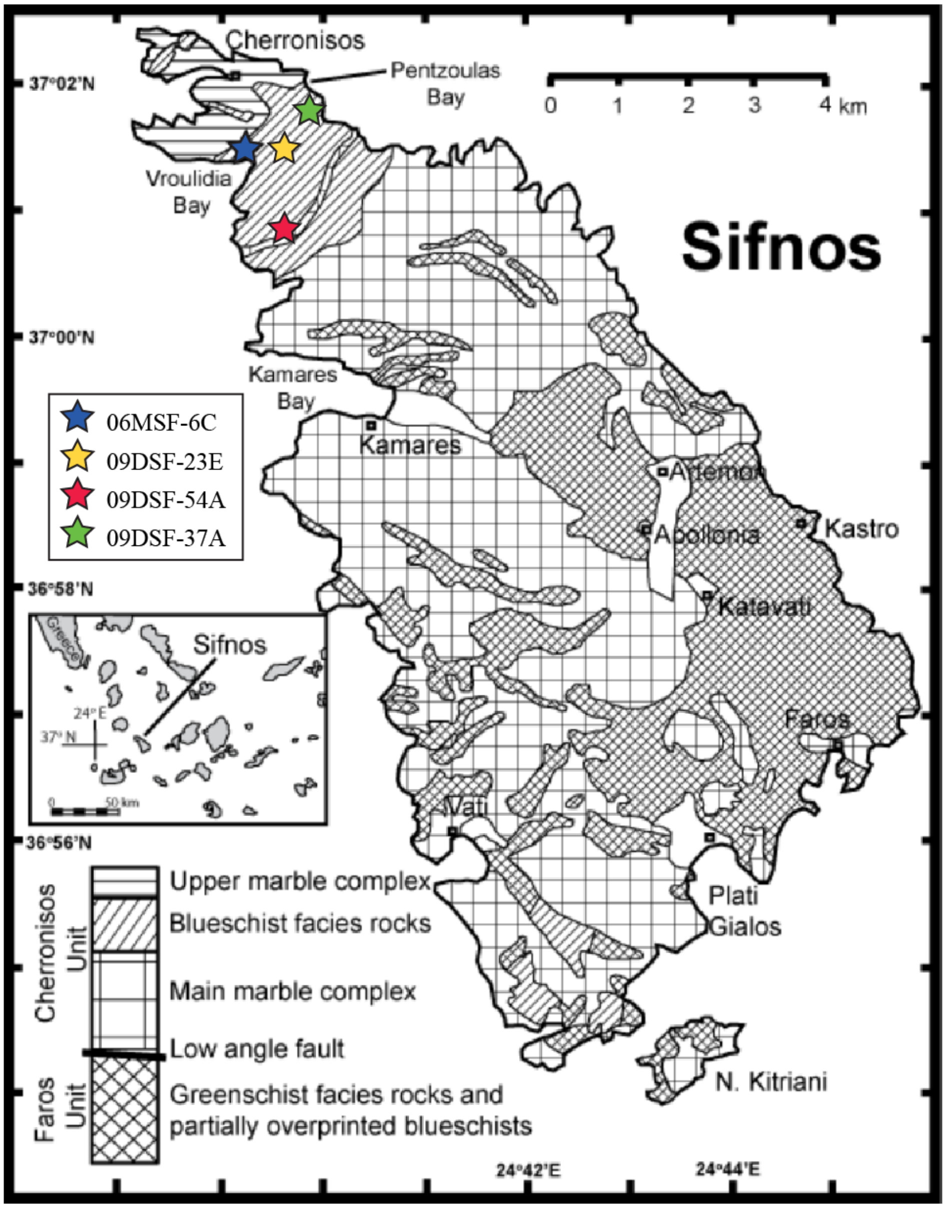

Figure 2.1 – Map of Sifnos, Greece showing sample locations as colored stars. Samples mapped here are all metabasites from the Cycladic Blueschist Unit, mapped in the Cherronisos Unit as blueschist facies rocks (diagonal lines). Samples were originally described and GPS locations are provided in Dragovic (2013). Map is modified after Dragovic (2013), Matthews and Schliestedt (1984) and Trotet et al., (2001).

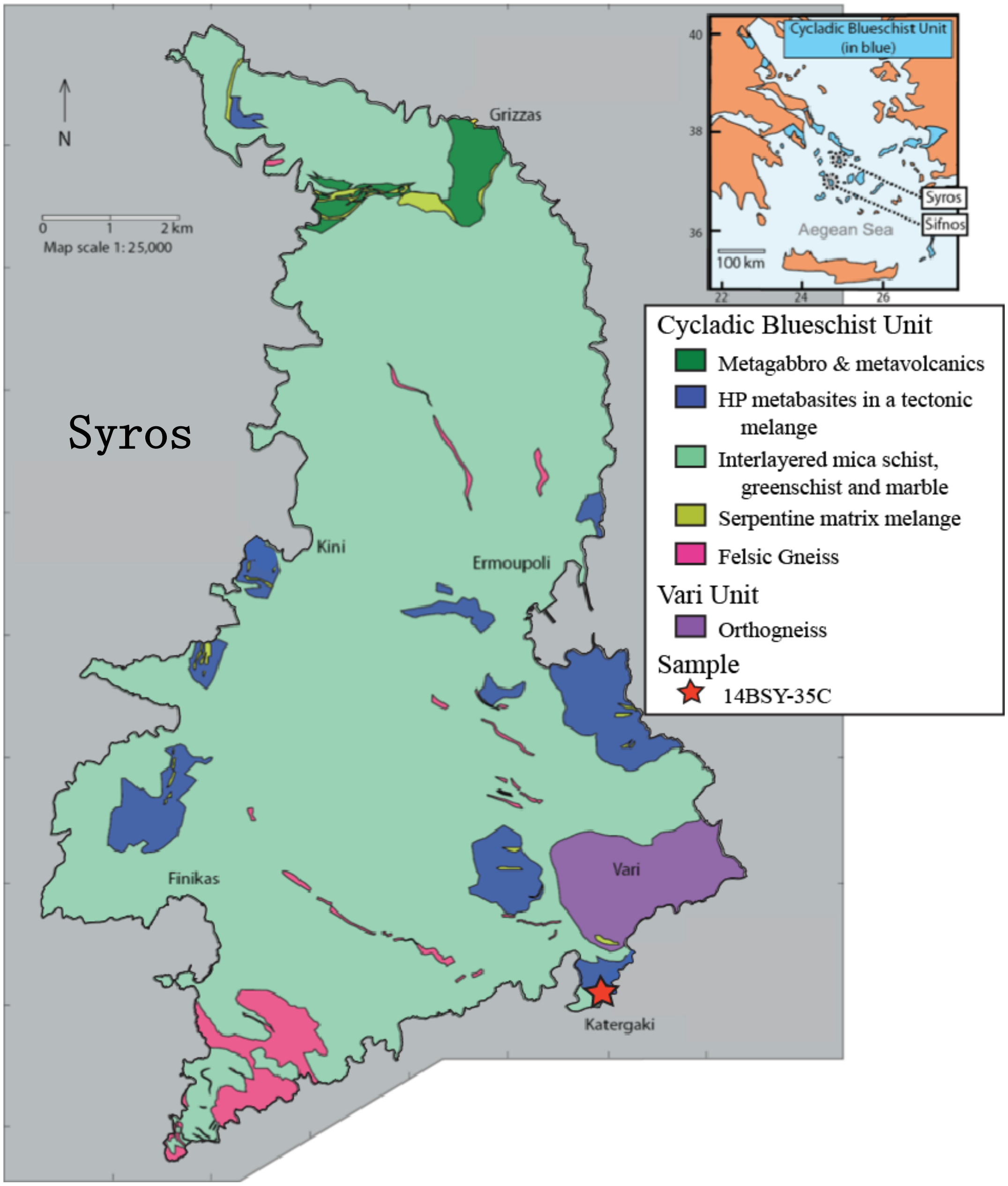

Figure 2.2 – Map of Syros, Greece showing sample 14BSY-35C as a red star. Sample 14BSY-35C is a metabasite from the Cycladic Blueschist Unit (mapped in blue). This sample was originally described by Kendall (2016). Map is modified after Kendall (2016) and Keiter et al. (2011).

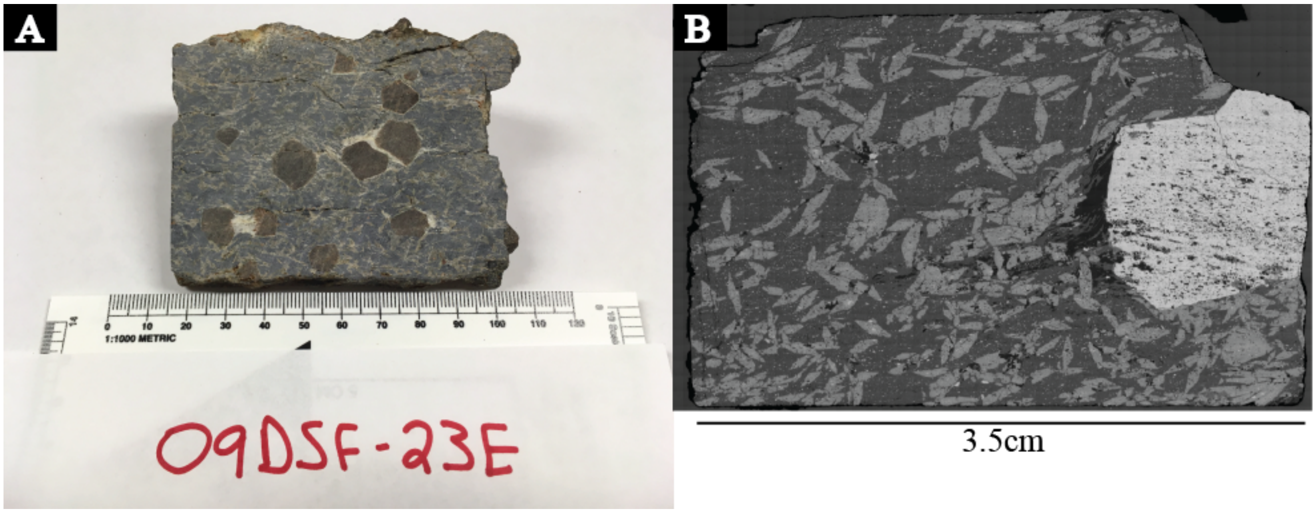

Figure 2.3 – Sample 09DSF-23E in A) hand sample and B) backscatter electron image of the thin section from this sample. Large garnet porphyroblasts measuring up to 1.75cm in diameter and epidote porphyroblasts up to 1cm in length are easily visible in both hand sample and thin section for 09DSF-23E.

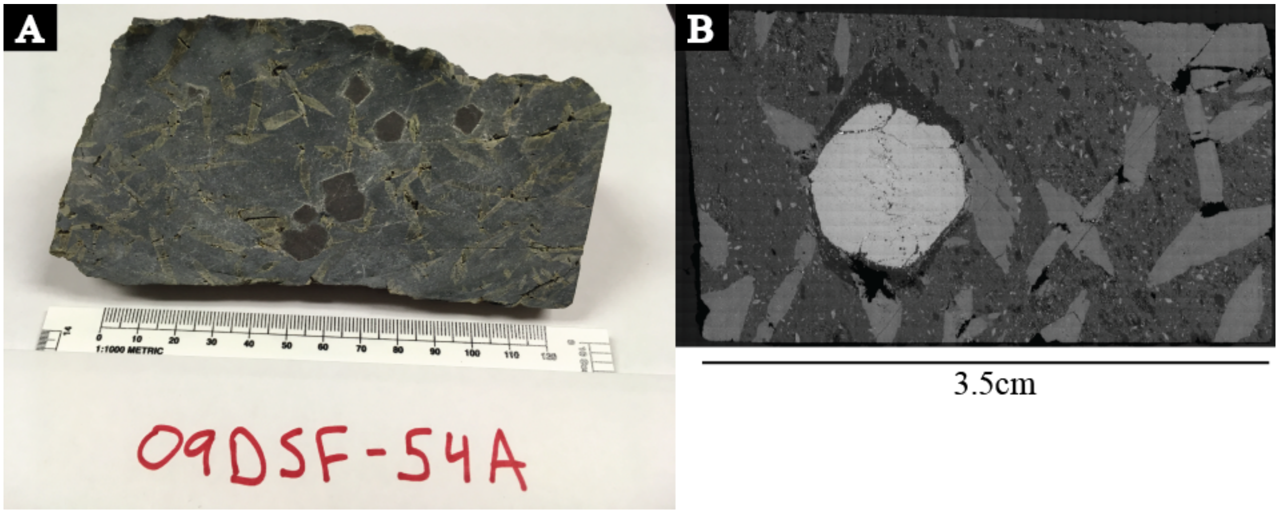

Figure 2.4 – Sample 09DSF-54A in A) hand sample and B) backscatter electron image of the thin section from this sample. Large garnet porphyroblasts measuring up to 1.75cm in diameter and epidote porphyroblasts up to 3cm in length are easily visible in both hand sample and thin section for 09DSF-54A.

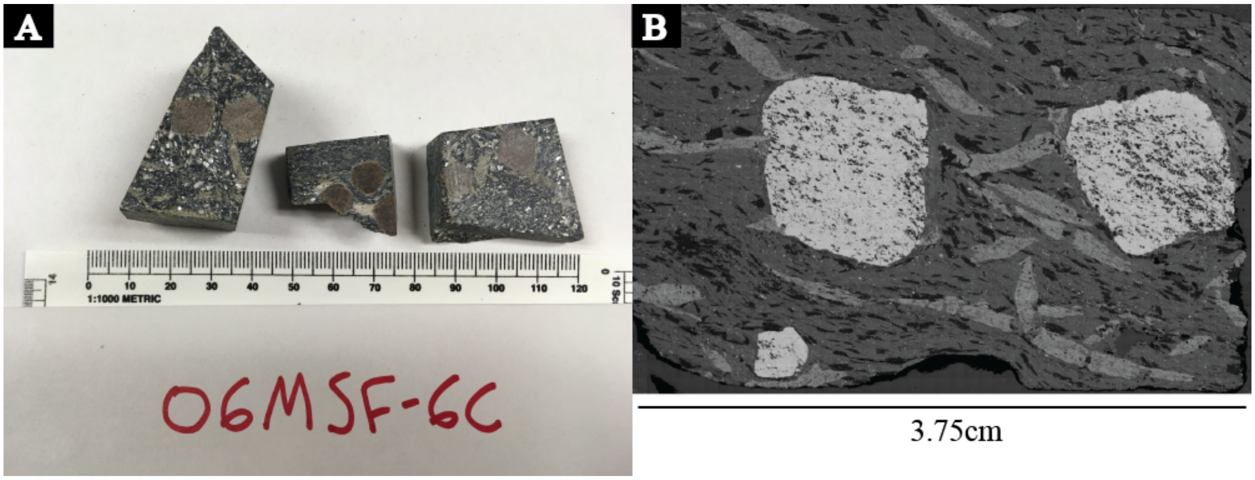

Figure 2.5 – Sample 06MSF-6C in A) hand sample and B) backscatter electron image of the thin section from this sample. Large garnet porphyroblasts measuring up to 1.5cm in diameter and epidote porphyroblasts up to 1cm in length are easily visible in both hand sample and thin section for 06MSF-6C.

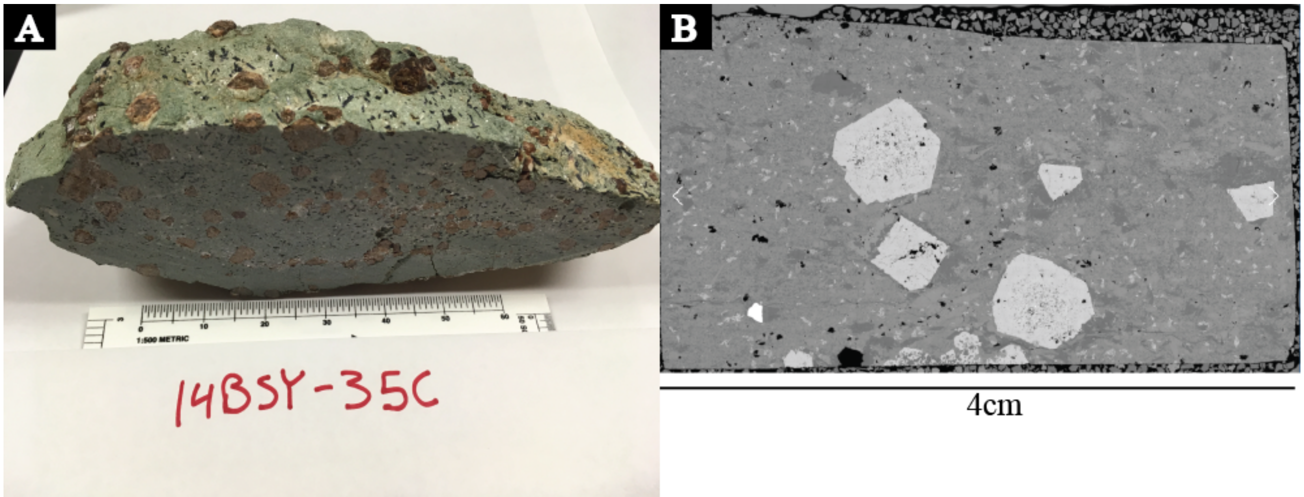

Figure 2.6– Sample 14BSY-35C in A) hand sample and B) backscatter electron image of the thin section from this sample. Large garnet porphyroblasts measuring up to ~1cm in diameter and acicular glaucophane up to 1cm in length in an omphacite dominated matrix are easily visible in both hand sample and thin section for 14BSY-35C.

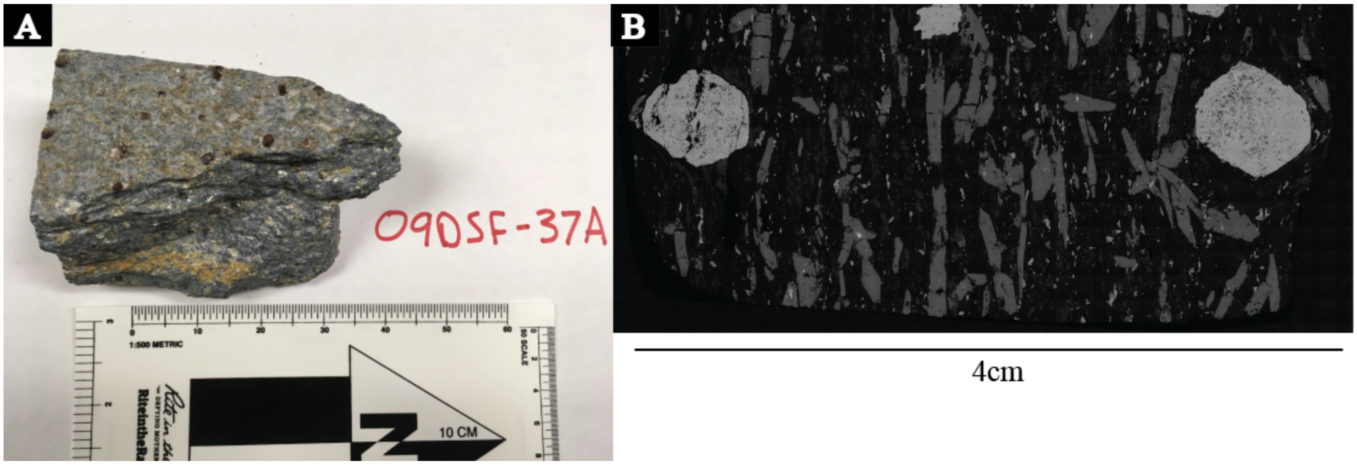

Figure 2.7 – Sample 09DSF-37A in A) hand sample and B) backscatter electron image of the thin section from this sample. Large garnet porphyroblasts measuring up to 3mm in diameter and epidote porphyroblasts are easily visible in both hand sample and thin section for 09DSF-37A.

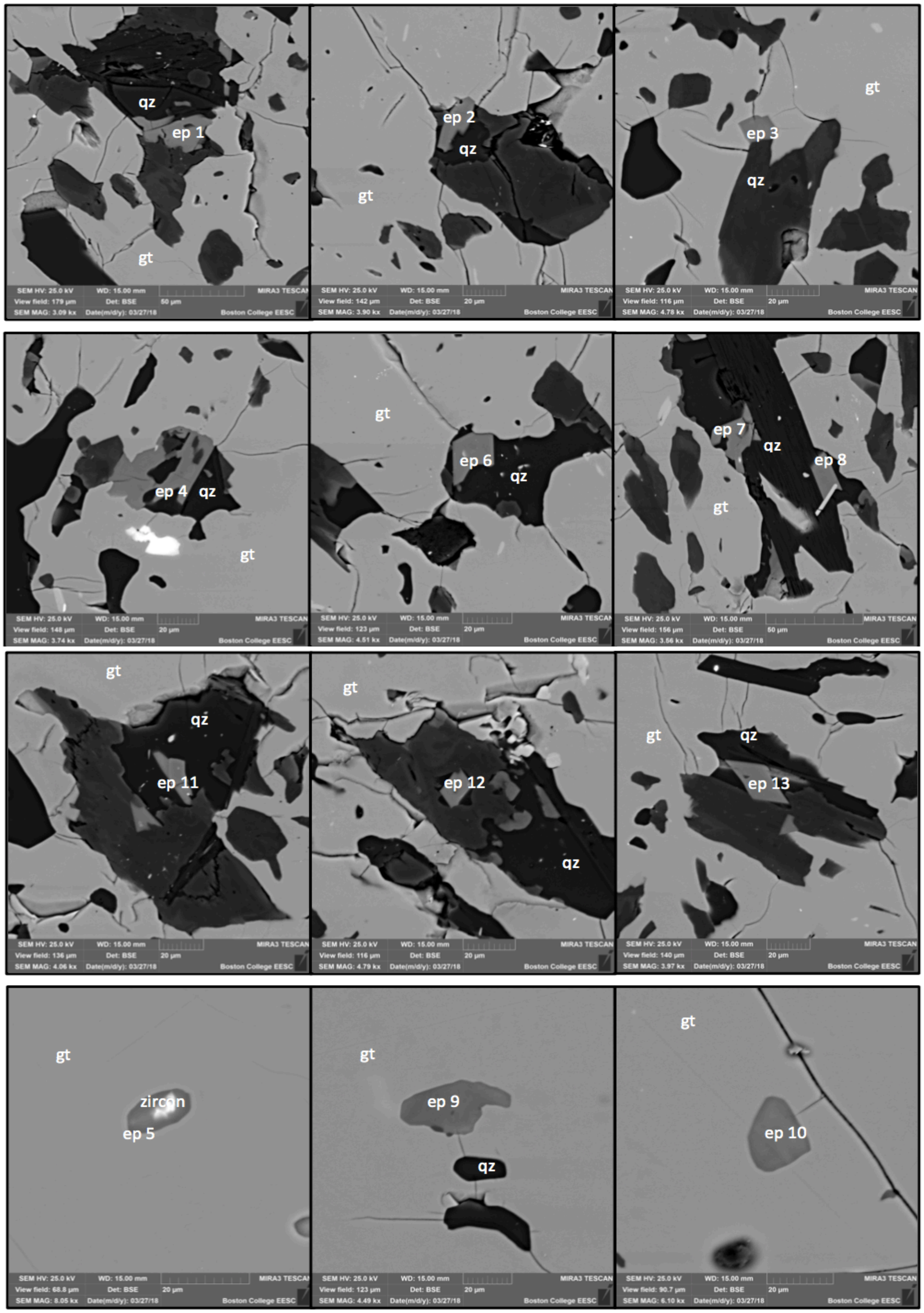

Figure 2.8 – BSE images of epidote inclusions in sample 14BSY-35C used in oxybarometer calculations. Epidote inclusions 1, 2, 3, 4, 6, 7, 8, 11, 12, and 13 are in garnet cores and inclusions 5, 9, and 10 (bottom row) are in garnet rims. BSE images include epidote (ep) and quartz (qz) inclusions in garnet (gt).

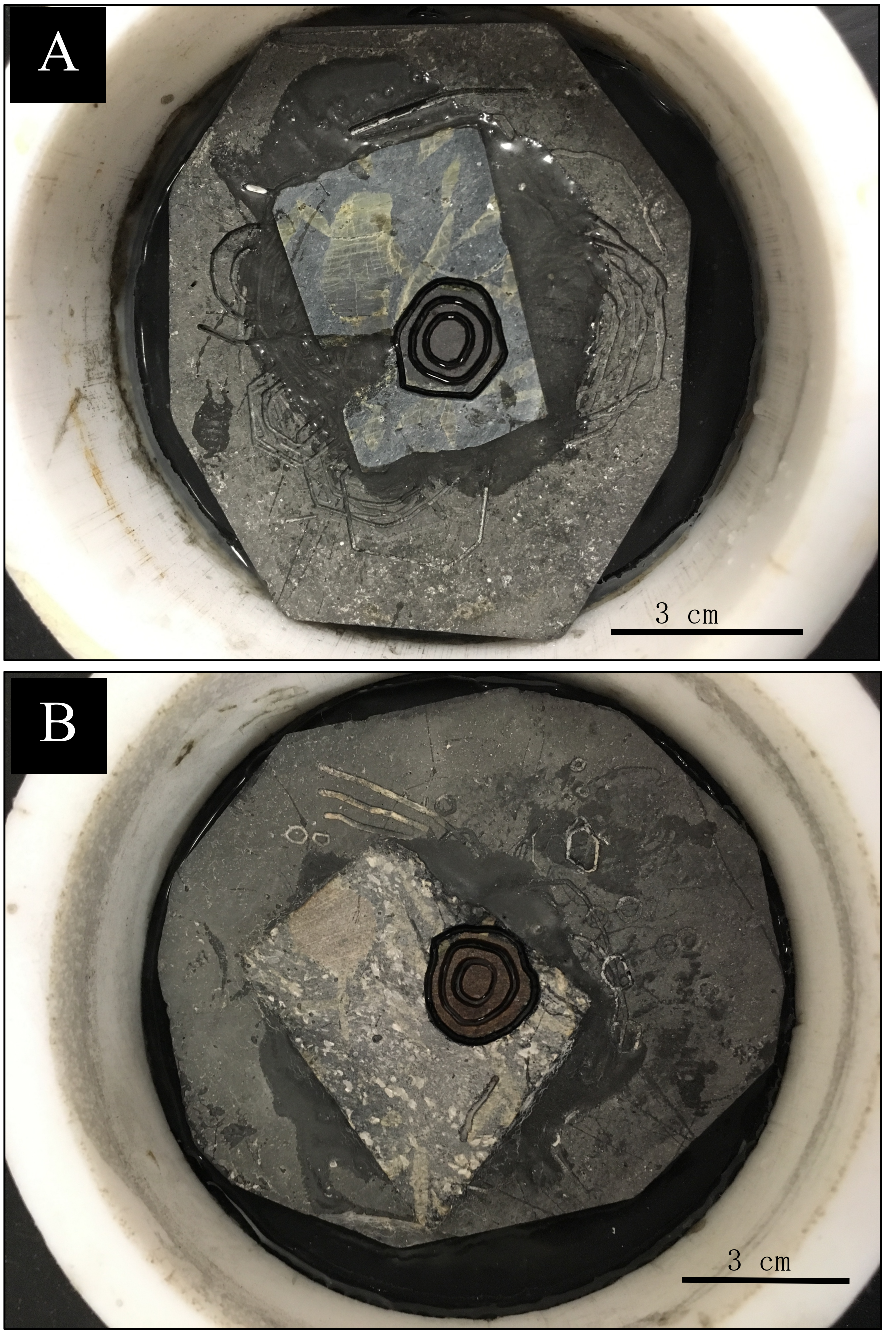

Figure 2.9 – Micro-drilling of garnet growth zones from samples A) 09DSF-54A B) 06MFS-6C. Garnets were drilled using the NewWave MicroMill drill at Boston College with the micro-drilling techniques presented in Pollington and Baxter (2011) to obtain three zones (core, zone 2, and rim) from samples 09DSF-54A and 06MSF-6C.

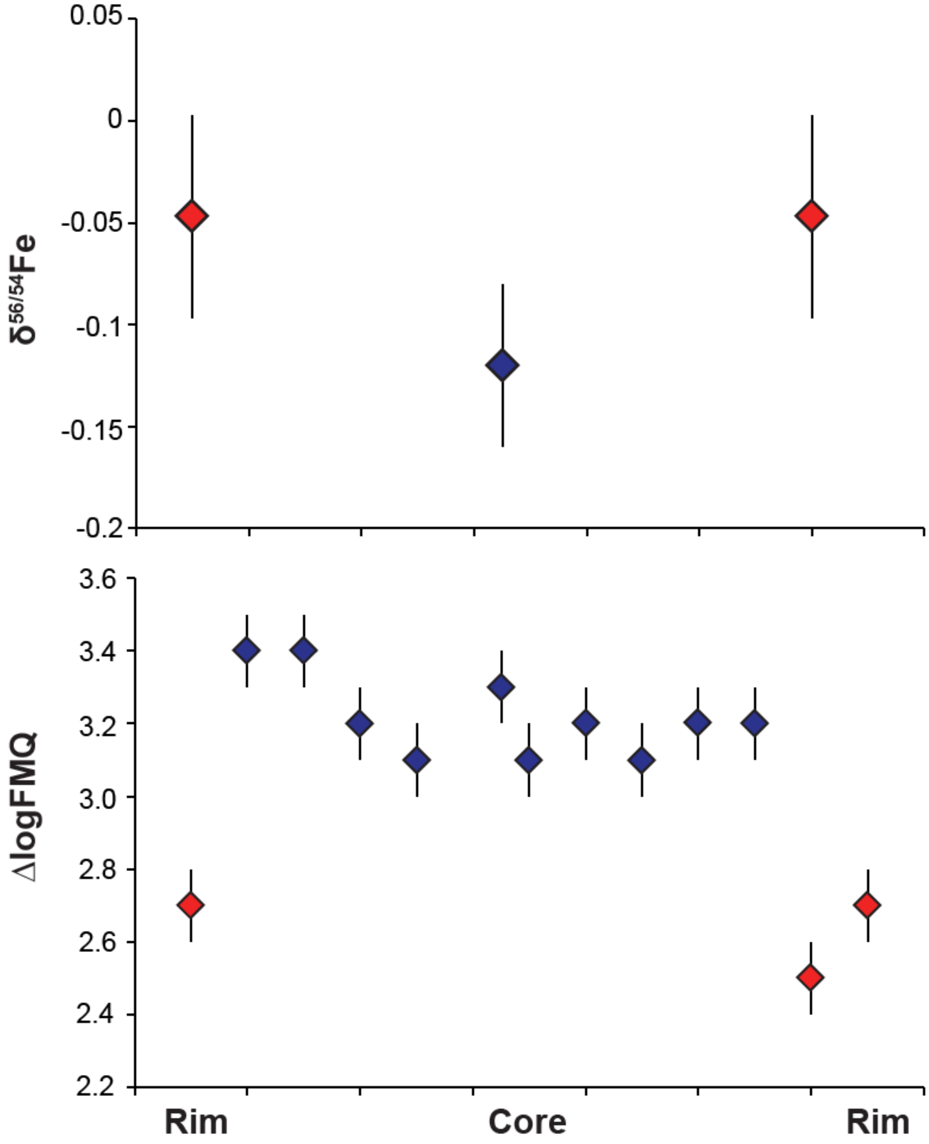

Figure 2.10 –ΔlogFMQ and δ$^{56/54}$Fe plotted rim to rim in one garnet grain for sample 14BSY-35C. Garnet cores are plotted in blue and rims are plotted in red. Error calculations for the δ$^{56/54}$Fe data are the two-standard deviation of four isotopic analysis for each sample. All error for ΔlogFMQ are ±0.1 log units based on oxygen barometer error.

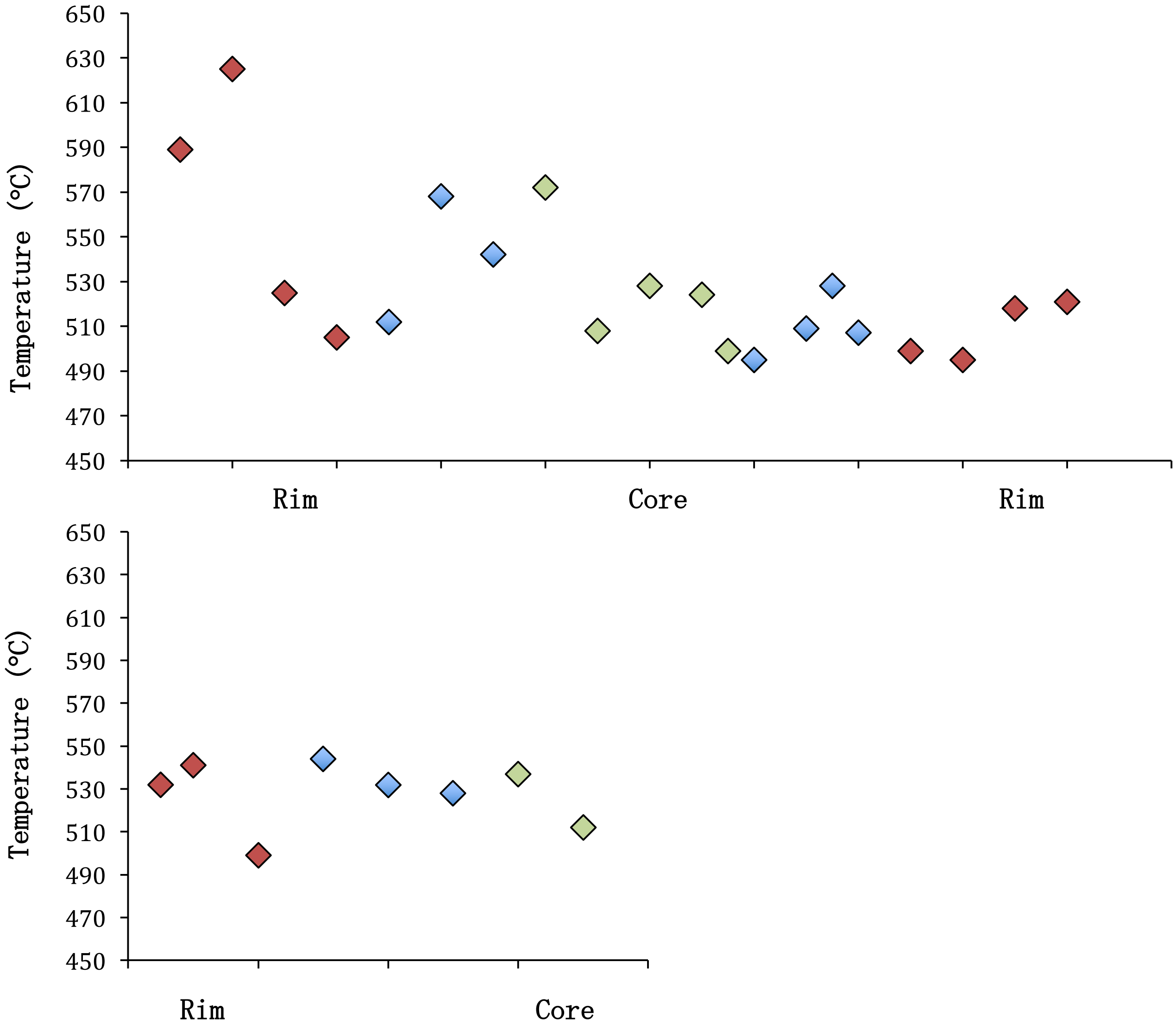

Figure 2.11 –Oxygen fugacity data for sample 09DSF-37A garnet 1(top) and garnet 2 (bottom) from core to rim at a constant fO_2 of -18 $\log fO_2$. Each diamond represents an fO_2 calculation with an epidote inclusion and the surrounding garnet. Orange diamonds represent epidote inclusions in garnet rims, blue diamonds are epidote inclusions in garnet middle zones, and green diamonds are epidote in garnet cores.

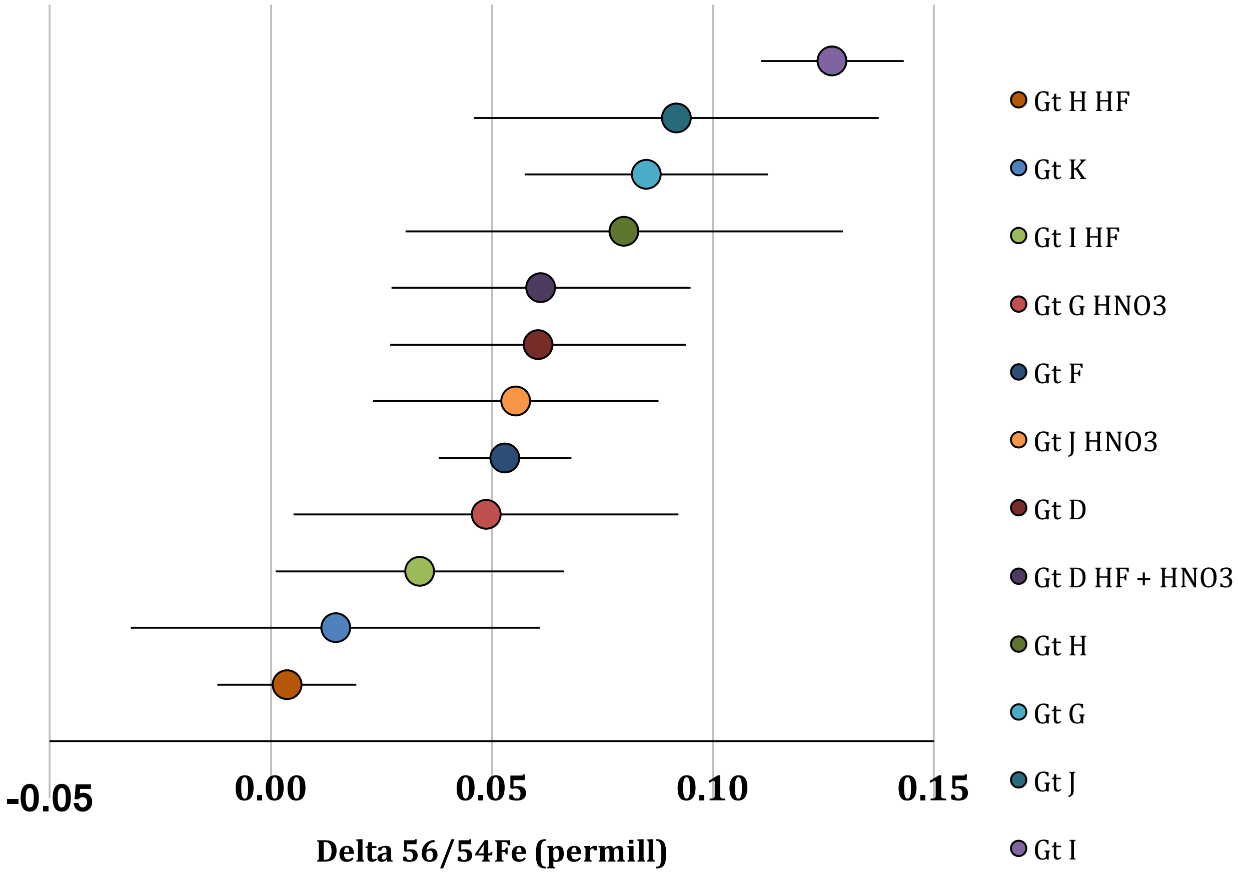

Figure 2.12 –The $\delta^{56/54}$Fe compositions with reported error for all partial dissolution test described in the Methods section. This data is presented in Table 2.12.

2.7 APPENDIX A: LAGO DI CIGNANA, WESTERN ALPS, ITALY

2.7.1 Geologic Setting

Lago di Cignana ultra high-pressure Unit (LCU) (Western Alps, Italy) exposes ultrahigh-pressure, low-temperature (UHP/LT) metamorphic rocks, including eclogite facies metabasalts. The LCU is part of the Zermatt-Saas ophiolite which is composed of metabasite and metasediments and forms the northern part of the Piemonte zone (Reinecke, 1998). The LCU is an ~200m thick lithologic unit that outcrops as three thin lenses approximately 1400m, 350m, and 300m in length (Forster et al., 2004) situated between units of calcschists and metaophiolites (Figure 3). The LCU has been widely interpreted to be remnants of the former Jurassic aged Piedmont oceanic lithosphere and formed during the subduction of the Piedmontese oceanic basin associated with the collision of Eurasia and the Apulian Plate in the Apline Orogeny (Van der Klauw et al., 1997). The discovery of coesite inclusions in garnet rims (Reinecke, 1991) within eclogite samples of the LCU suggests equilibration under peak metamorphic conditions of 590-605°C at >3.2GPa (Groppo et al., 2009) during prograde metamorphism at ca. 50-38 Ma (Lapen et al., 2003 and references therein).

Fieldwork was conducted in August 2017 to collect eclogite samples from Lago di Cignana for this study. Two eclogite samples, G17-S825A02 (Figure 2.14) and G17-S825A03 (Figure 2.15), were collected from an outcrop of the LCU on the edge of Lago di Cignana (Table 2.1 and Figure 2.13). The outcrop consists of eclogitized oceanic basalt, quartzite, and Mn-rich chert. Sampling focused on the oceanic basalts, which outcropped as a thin lens that appeared to be partially retrogressed to blueschist and greenschist facies resulting in a 'banded' outcrop appearance. Several metamorphosed oceanic basalt samples were collected which contained garnet porphyroblasts up to 5mm included within bands of relatively fresh eclogite, lawsonite rich eclogite, blueschist, and greenschist (Figure 2.14 and Figure 2.15). Each collected sample will be described in greater detail in the next section.

2.7.2 Sample Descriptions

Sample G17-S825A02 is an eclogite with large porphyroblasts of garnet in a omphacite and glaucophane rich matrix (Figure 2.14) collected for this study from Lago di Cignana, Italy in August 2017 (Table 2.1 and Figure 2.3). The mineral assemblage in sample G17-S825A02 includes large garnet porphyroblasts measuring up to 4mm in diameter, glaucophane, omphacite, white mica, albite, apatite, quartz, sphene, and calcite. Mineral inclusions in garnet porphyroblasts include quartz, glaucophane, epidote, albite, pyroxene, phengite, paragonite. While Lago di Cignana, Italy is a famous ultrahigh-pressure locality and known for the presence of coesite inclusions in garnet rims (Reinecke, 1991), no coesite or evidence of former coesite has been observed in sample G17-S825A02.

Sample G17-S825A03 is very similar to sample G17-S825A02 as it is an eclogite with large porphyroblasts of garnet in a omphacite and glaucophane rich matrix (Figure

2.15) collected for this study from Lago di Cignana, Italy in August 2017 (Table 2.1 and Figure 2.3). The mineral assemblage for sample G17-S825A03 includes garnet porphyroblasts measuring up to 5mm in diameter, glaucophane, omphacite, white mica, albite, apatite, quartz, sphene, and calcite. Mineral inclusions in garnet porphyroblasts include quartz, glaucophane, epidote, albite, pyroxene, phengite, paragonite. Like G17-S825A02, no coesite has been observed in G17-S825A03.

2.7.3 Figures

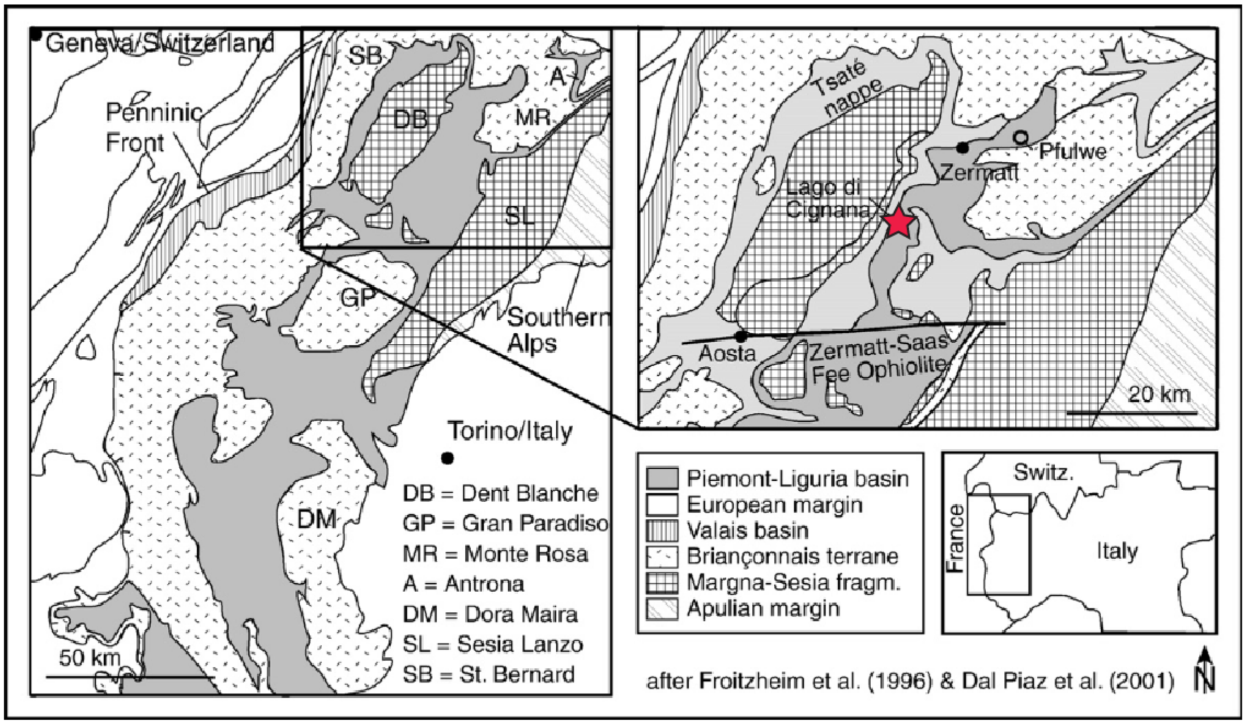

Figure 2.13 – Geologic map of Lago di Cignana, Western Alps, Italy with both samples collected in August 2017 from Lago di Cignana as the red star. GPS coordinates for sample G17-S825A02 at the site of collection is N45° 52’ 70.5”, E07° 35’ 54.9” and N45° 52’ 70.4”, E07° 35’ 57.8” for sample G17-S825A03. Map was modified after Skora et al., (2009), Froitzheim et al (1996), and Dal Piaz et al. (2001).

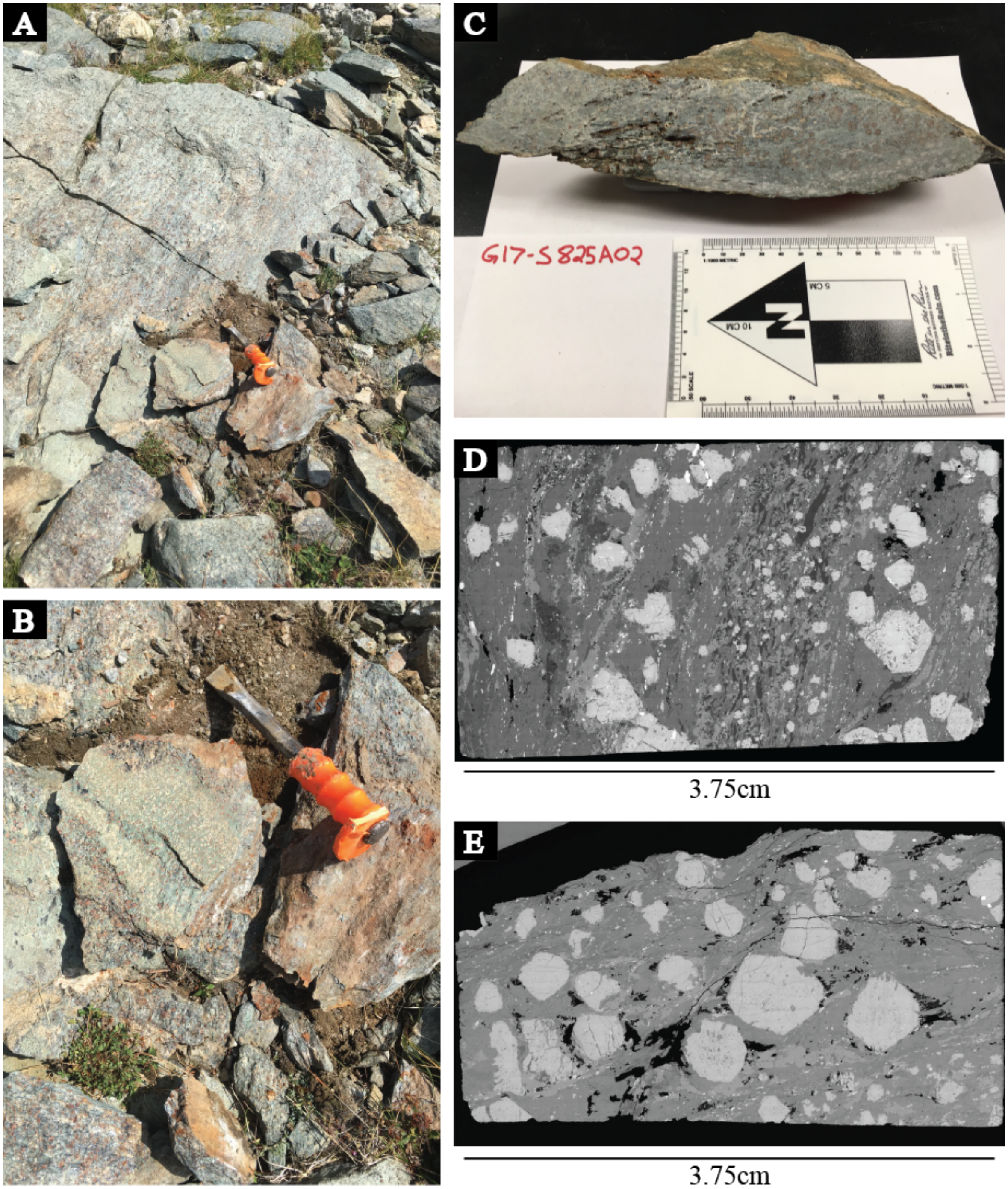

Figure 2.14 – Sample G17-S825A02 in A) field photo B) field photo C) hand sample D) backscatter electron image of thin section G17-S825A02a from this sample and E) backscatter electron image of thin section G17-S825A02b. A) and B) show sample G17-S825A02 at the site of collection (N45° 52’ 70.5”, E07° 35’ 54.9”) Lago di Cignana, Western Alps, Italy in August 2017. G17-S825A02 is characterized by a typical HP/LT assemblage including large garnet porphyroblasts measuring up to 4mm in diameter in a glaucophane and omphacite rich matrix.

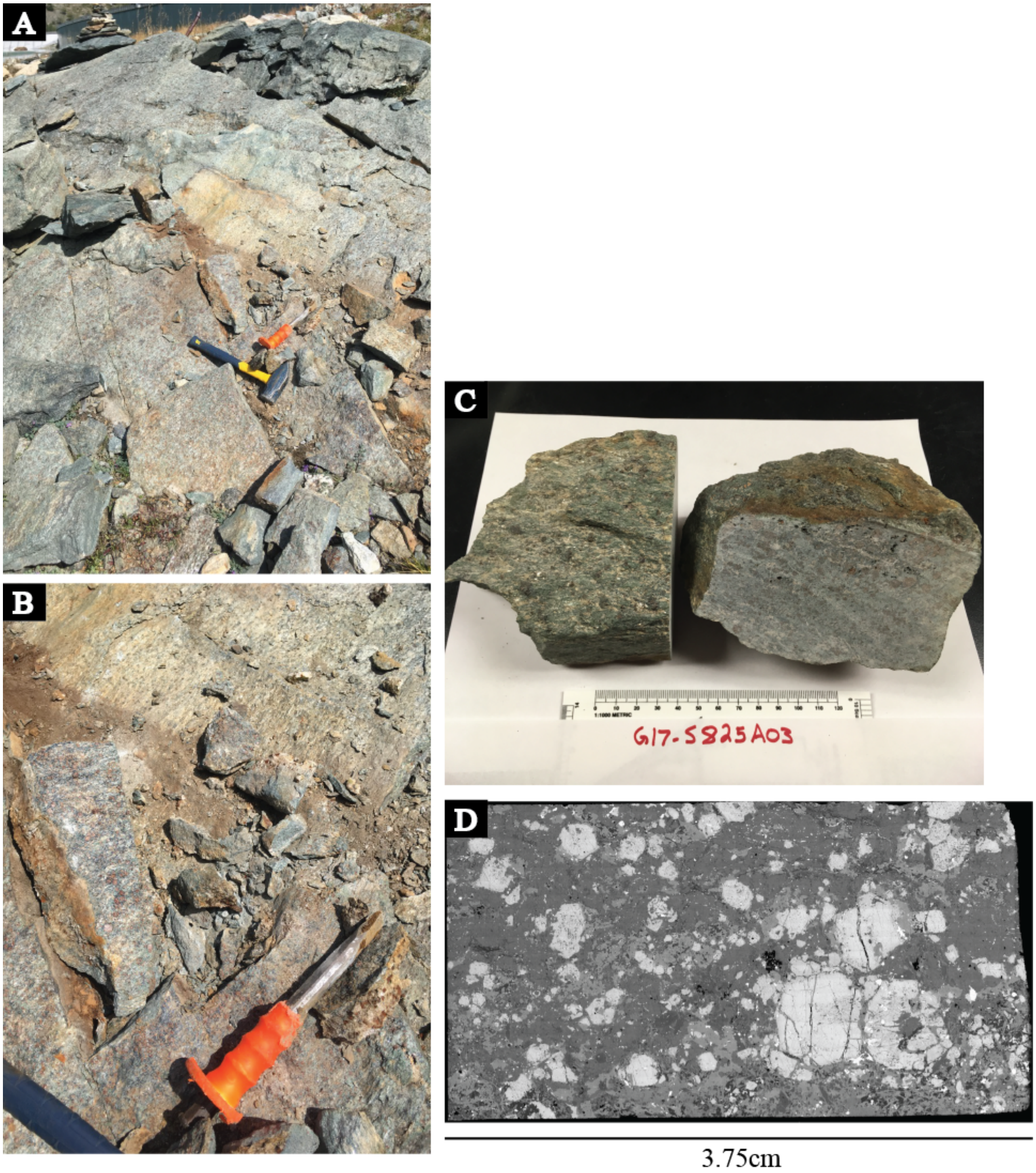

Figure 2.15 – Sample G17-S825A03 in A) field photo, B) field photo, C) hand sample, and D) backscatter electron image of thin section G17-S825A03 from this sample. A) and B) show sample G17-S825A03 at the site of collection Italy (N45° 52' 70.4", E07° 35' 57.8") Lago di Cignana, Western Alps, Italy in August 2017. G17-S825A03 is characterized by a typical HP/LT assemblage including large garnet porphyroblasts measuring up to 5mm in diameter in a glaucophane and omphacite rich matrix.

2.8 REFERENCES

Agard, P., Goffé, B., Touret, J.L. and Vidal, O., 2000. Retrograde mineral and fluid evolution in high-pressure metapelites (Schistes lustrés unit, Western Alps). *Contributions to Mineralogy and Petrology*, *140*(3), pp.296-315.

Altherr, R., Schliestedt, M., Okrusch, M., Seidel, E., Kreuzer, H., Harre, W., Lenz, H., Wendt, I. and Wagner, G.A., 1979. Geochronology of high-pressure rocks on Sifnos (Cyclades, Greece). *Contributions to Mineralogy and Petrology*, *70*(3), pp.245-255.

Auzanneau, E., Schmidt, M.W., Vielzeuf, D. and Connolly, J.D., 2010. Titanium in phengite: a geobarometer for high temperature eclogites. *Contributions to Mineralogy and Petrology*, *159*(1), p.1.

Avigad, D., 1993. Tectonic juxtaposition of blueschists and greenschists in Sifnos Island (Aegean Sea)—implications for the structure of the Cycladic blueschist belt. *Journal of Structural Geology*, *15*(12), pp.1459-1469.

Avigad, D. and Garfunkel, Z., 1991. Uplift and exhumation of high-pressure metamorphic terrains: the example of the Cycladic blueschist belt (Aegean Sea). *Tectonophysics*, *188*(3), pp.357-372.

Barr, H., 1990. Preliminary fluid inclusion studies in a high-grade blueschist terrain, Syros, Greece. *Mineralogical Magazine*, *54*(375), pp.159-168.

Baxter, E.F. and Caddick, M.J., 2013. Garnet growth as a proxy for progressive subduction zone dehydration. *Geology*, *41*(6), pp.643-646.

Boundy, T.M., Donohue, C.L., Essene, E.J., Mezger, K. and Austrheim, H., 2002. Discovery of eclogite facies carbonate rocks from the Lindås Nappe, Caledonides, Western Norway. *Journal of Metamorphic Geology*, *20*(7), pp.649-667.

Breeding, C.M., Ague, J.J. and Bröcker, M., 2004. Fluid–metasedimentary rock interactions in subduction-zone mélange: implications for the chemical composition of arc magmas. *Geology*, *32*(12), pp.1041-1044.

Cao, Y., Song, S.G., Niu, Y.L., Jung, H. and Jin, Z.M., 2011. Variation of mineral composition, fabric and oxygen fugacity from massive to foliated eclogites during exhumation of subducted ocean crust in the North Qilian suture zone, NW China. *Journal of Metamorphic Geology*, *29*(7), pp.699-720.

Cheney, J.T., Brady, J.B., Harms, T.A. and Schumacher, J.C., 2001. Evolution of Cycladic Subduction Zone Rocks: Syros Blueschist-Eclogite Terrane III. In *Keck Symposium* (Vol. 14, pp. 107-112).

Christie, D.M., Carmichael, I.S. and Langmuir, C.H., 1986. Oxidation states of mid-ocean ridge basalt glasses. *Earth and Planetary Science Letters*, *79*(3-4), pp.397-411.

Coggon, R. and Holland, T.J.B., 2002. Mixing properties of phengitic micas and revised garnet-phengite thermobarometers. *Journal of Metamorphic Geology*, *20*(7), pp.683-696.

Connolly, J.A.D., 2009. The geodynamic equation of state: what and how. *Geochemistry, Geophysics, Geosystems*, *10*(10).

Dal Piaz, G., Cortiana, G., Del Moro, A., Martin, S., Pennacchioni, G. and Tartarotti, P., 2001. Tertiary age and paleostructural inferences of the eclogitic imprint in the Austroalpine outliers and Zermatt–Saas ophiolite, western Alps. *International Journal of Earth Sciences*, *90*(3), pp.668-684.

Dauphas, N., John, S.G. and Rouxel, O., 2017. Iron isotope systematics. *Reviews in Mineralogy and Geochemistry*, *82*(1), pp.415-510.

Debret, B., Millet, M.A., Pons, M.L., Bouilhol, P., Inglis, E. and Williams, H., 2016. Isotopic evidence for iron mobility during subduction. *Geology*, *44*(3), pp.215-218.

Diener, J.F.A. and Powell, R., 2012. Revised activity–composition models for clinopyroxene and amphibole. *Journal of Metamorphic Geology*, *30*(2), pp.131-142.

Donohue, C.L. and Essene, E.J., 2000. An oxygen barometer with the assemblage garnet–epidote. *Earth and Planetary Science Letters*, *181*(3), pp.459-472.

Dragovic, B., 2013. *Constraining the rates and timescales of garnet growth and associated dehydration during metamorphism* (Doctoral dissertation, Boston University).

Dragovic, B., Baxter, E.F. and Caddick, M.J., 2015. Pulsed dehydration and garnet growth during subduction revealed by zoned garnet geochronology and thermodynamic modeling, Sifnos, Greece. *Earth and Planetary Science Letters*, *413*, pp.111-122.

Dragovic, B., Samanta, L.M., Baxter, E.F., Selverstone, J., 2012. Using garnet to constrain the duration and rate of water-releasing metamorphic reactions during subduction: an example from Sifnos, Greece. Chem. Geol. 314–317, 9–22.

Evans, K.A., 2012. The redox budget of subduction zones. *Earth-Science Reviews*, *113*(1-2), pp.11-32.

Evans, K.A., Elburg, M.A. and Kamenetsky, V.S., 2012. Oxidation state of subarc mantle. *Geology*, *40*(9), pp.783-786.

Forster, M., Lister, G., Compagnoni, R., Giles, D., Hills, Q., Betts, P., Beltrando, M. and Tamagno, E., 2004. Mapping of oceanic crust with" HP" to" UHP" metamorphism: The Lago di Cignana Unit,(Western Alps). In *Mapping geology in Italy*. Geological Society of London.

Froitzheim, N., Schmid, S.M. and Frey, M., 1996. Mesozoic paleogeography and the timing of eclogite-facies metamorphism in the Alps: a working hypothesis. *Eclogae Geologicae Helvetiae*, *89*(1), p.81.

Frost, B.R., 1991. Introduction to oxygen fugacity and its petrologic importance. *Reviews in Mineralogy and Geochemistry*, *25*(1), pp.1-9.

Furman, M.L., 1988. Ternary-feldspar modeling and thermometry. *Amer. Mineral.*, *73*, pp.201-215.

Gerrits, A.R., 2013, October. The redox state of the Franciscan trench. In *2013 GSA Annual Meeting in Denver*.

Groppo, C., Beltrando, M. and Compagnoni, R., 2009. The P–T path of the ultra-high pressure Lago di Cignana and adjoining high-pressure meta-ophiolitic units: insights into the evolution of the subducting Tethyan slab. *Journal of Metamorphic Geology*, *27*(3), pp.207-231.

Groppo, C., & Castelli, D., 2010. Prograde P–T evolution of a lawsonite eclogite from the Monviso meta-ophiolite (Western Alps): dehydration and redox reactions during subduction of oceanic FeTi-oxide gabbro. *Journal of Petrology*, *51*(12), 2489-2514.

Holland, T.J.B. and Powell, R., 1998. An internally consistent thermodynamic data set for phases of petrological interest. *Journal of metamorphic Geology*, *16*(3), pp.309-343.

Kelley, K.A. and Cottrell, E., 2009. Water and the oxidation state of subduction zone magmas. *Science*, *325*(5940), pp.605-607.

Kendall, J., 2016. *Sm/Nd garnet geochronology and pressure-temperature paths of eclogites from Syros, Greece: Implications for subduction zone processes and water loss from the subducting slab* (Doctoral dissertation, Boston College).

Keiter, M., Ballhaus, C. and Tomaschek, F., 2011. A new geological map of the Island of Syros (Aegean Sea, Greece): implications for lithostratigraphy and structural history of the Cycladic Blueschist Unit. *Geological Society of America Special Papers*, *481*, pp.1-43.

Lapen, T.J., Johnson, C.M., Baumgartner, L.P., Mahlen, N.J., Beard, B.L. and Amato, J.M., 2003. Burial rates during prograde metamorphism of an ultra-high-pressure terrane: an example from Lago di Cignana, western Alps, Italy. *Earth and Planetary Science Letters*, *215*(1-2), pp.57-72.

Lee, C.T.A., Luffi, P., Le Roux, V., Dasgupta, R., Albaréde, F. and Leeman, W.P., 2010. The redox state of arc mantle using Zn/Fe systematics. *Nature*, *468*(7324), p.681.

Lee, C.T., Leeman, W.P., Canil, D. and Li, Z.X.A., 2005. Similar V/Sc systematics in MORBs and arc basalts: Implications for the oxygen fugacities of their mantle source regions. *Geochimica et Cosmochimica Acta Supplement*, *69*, p.A639.

Lister, G.S. and Forster, M.A., 2016. White mica 40Ar/39Ar age spectra and the timing of multiple episodes of high-P metamorphic mineral growth in the Cycladic eclogite–blueschist belt, Syros, Aegean Sea, Greece. *Journal of Metamorphic Geology*, *34*(5), pp.401-421.

Magni, V., Bouilhol, P. and van Hunen, J., 2014. Deep water recycling through time. *Geochemistry, Geophysics, Geosystems*, *15*(11), pp.4203-4216.

Marschall, H.R. and Schumacher, J.C., 2012. Arc magmas sourced from mélange diapirs in subduction zones. *Nature Geoscience*, *5*(12), pp.862-867.

Mattinson, C.G., Zhang, R.Y., Tsujimori, T. and Liou, J.G., 2004. Epidote-rich talc-kyanite-phengite eclogites, Sulu terrane, eastern China: P-T-fO_2estimates and the significance of the epidote-talc assemblage in eclogite. *American Mineralogist*, *89*(11-12), pp.1772-1783.

Matthews, A. and Schliestedt, M., 1984. Evolution of the blueschist and greenschist facies rocks of Sifnos, Cyclades, Greece. *Contributions to Mineralogy and*

Petrology, *88*(1), pp.150-163.

Ming, T., Erdman, M., Eldridge, G., Lee, C.T.A., 2018. The redox "filter" beneath magmatic orogens and the formation of continental crust. *Science Advances, 4*, 5.

Okazaki, K. and Hirth, G., 2016. Dehydration of lawsonite could directly trigger earthquakes in subducting oceanic crust. *Nature*, *530*(7588), p.81.

Okrusch, M. and Bröcker, M., 1990. Eclogites associated with high-grade blueschists in the Cyclades archipelago, Greece: a review. *European Journal of Mineralogy*, pp.451-478.

Palin, R.M., Weller, O.M., Waters, D.J. and Dyck, B., 2016. Quantifying geological uncertainty in metamorphic phase equilibria modelling; a Monte Carlo assessment and implications for tectonic interpretations. *Geoscience Frontiers*, *7*(4), pp.591-607.

Parkinson, I.J. and Arculus, R.J., 1999. The redox state of subduction zones: insights from arc-peridotites. *Chemical Geology*, *160*(4), pp.409-423.

Poli, S. and Schmidt, M.W., 1995. H2O transport and release in subduction zones: experimental constraints on basaltic and andesitic systems. *Journal of Geophysical Research: Solid Earth*, *100*(B11), pp.22299-22314.

Pollington, A.D., Baxter, E.F., 2011. High precision microsampling and preparation of zoned garnet porphyroblasts for Sm–Nd geochronology. Chem. Geol. 281, 270–282.

Polyakov, V.B. and Mineev, S.D., 2000. The use of Mössbauer spectroscopy in stable isotope geochemistry. *Geochimica et Cosmochimica Acta*, *64*(5), pp.849-865.

Powell, R. and Holland, T.J.B., 1988. An internally consistent dataset with uncertainties and correlations: 3. Applications to geobarometry, worked examples and a computer program. *Journal of metamorphic Geology*, *6*(2), pp.173-204.

Powell, R. and Holland, T., 1994. Optimal geothermometry and geobarometry. *American Mineralogist*, *79*(1-2), pp.120-133.

Powell, R., Holland, T.J.B.H. and Worley, B., 1998. Calculating phase diagrams involving solid solutions via non-linear equations, with examples using THERMOCALC. *Journal of metamorphic Geology*, *16*(4), pp.577-588.

Reinecke, T., 1998. Prograde high-to ultrahigh-pressure metamorphism and exhumation of oceanic sediments at Lago di Cignana, Zermatt-Saas Zone, western

Alps. *Lithos*, *42*(3-4), pp.147-189.

Reinecke, T., 1991. Very-high-pressure metamorphism and uplift of coesite-bearing metasediments from the Zermatt-Saas zone, Western Alps. *European Journal of Mineralogy*, pp.7-18.

Sato, M. and Wright, T.L., 1966. Oxygen fugacities directly measured in magmatic gases. *Science*, *153*(3740), pp.1103-1105.

Schmidt, M.W. and Poli, S., 1998. Experimentally based water budgets for dehydrating slabs and consequences for arc magma generation. *Earth and Planetary Science Letters*, *163*(1), pp.361-379.

Schauble, E.A., Rossman, G.R. and Taylor, H.P., 2001. Theoretical estimates of equilibrium Fe-isotope fractionations from vibrational spectroscopy. *Geochimica et Cosmochimica Acta*, *65*(15), pp.2487-2497.

Schmädicke, E. and Will, T.M., 2003. Pressure–temperature evolution of blueschist facies rocks from Sifnos, Greece, and implications for the exhumation of high-pressure rocks in the Central Aegean. *Journal of Metamorphic Geology*, *21*(8), pp.799-811.

Skora, S., Lapen, T.J., Baumgartner, L.P., Johnson, C.M., Hellebrand, E. and Mahlen, N.J., 2009. The duration of prograde garnet crystallization in the UHP eclogites at Lago di Cignana, Italy. *Earth and Planetary Science Letters*, *287*(3), pp.402-411.

Tatsumi, Y., 1986. Formation of the volcanic front in subduction zones. *Geophysical Research Letters*, *13*(8), pp.717-720.

Trotet, F., Jolivet, L. and Vidal, O., 2001. Tectono-metamorphic evolution of Syros and Sifnos islands (Cyclades, Greece). *Tectonophysics*, *338*(2), pp.179-206.

Van der Klauw, S.N.G.C., Reinecke, T. and Stöckhert, B., 1997. Exhumation of ultrahigh-pressure metamorphic oceanic crust from Lago di Cignana, Piemontese zone, western Alps: the structural record in metabasites. *Lithos*, *41*(1-3), pp.79-102.

White, R.W., Powell, R. and Holland, T.J.B., 2007. Progress relating to calculation of partial melting equilibria for metapelites. *Journal of metamorphic Geology*, *25*(5), pp.511-527.

White, R.W., Powell, R. and Clarke, G.L., 2002. The interpretation of reaction textures in Fe-rich metapelitic granulites of the Musgrave Block, central Australia:

constraints from mineral equilibria calculations in the system K2O–FeO–MgO–Al2O3–SiO2–H2O–TiO2–Fe2O3. *Journal of metamorphic Geology*, *20*(1), pp.41-55.

White, R.W., Powell, R., Holland, T.J.B. and Worley, B.A., 2000. The effect of TiO~ 2 and Fe~ 2O~ 3 on metapelitic assemblages at greenschist and amphibolite facies conditions: mineral equilibria calculations in the system K~ 2O-FeO-MgO-Al~ 2O~ 3-SiO~ 2-H~ 2O-TiO~ 2-Fe~ 2O~ 3. *Journal of Metamorphic Geology*, *18*(5), pp.497-512.

Wijbrans, J.R., Schliestedt, M. and York, D., 1990. Single grain argon laser probe dating of phengites from the blueschist to greenschist transition on Sifnos (Cyclades, Greece). *Contributions to Mineralogy and Petrology*, *104*(5), pp.582-593.

Williams, H.M., McCammon, C.A., Peslier, A.H., Halliday, A.N., Teutsch, N., Levasseur, S. and Burg, J.P., 2004. Iron isotope fractionation and the oxygen fugacity of the mantle. *Science*, *304*(5677), pp.1656-1659.m

Williams, H.M., Nielsen, S.G., Renac, C., Griffin, W.L., O'Reilly, S.Y., McCammon, C.A., Pearson, N., Viljoen, F., Alt, J.C. and Halliday, A.N., 2009. Fractionation of oxygen and iron isotopes by partial melting processes: implications for the interpretation of stable isotope signatures in mafic rocks. *Earth and Planetary Science Letters*, *283*(1), pp.156-166.

Wood, B.J., Bryndzia, L.T. and Johnson, K.E., 1990. Mantle oxidation state and its relationship to tectonic environment and fluid speciation. *Science*, *248*(4953), pp.337-345.